UNIVERSITEIT ANTWERPEN
Faculteit Wetenschappen
Departement Fysica

First-principles study of defects in transparent conducting oxide materials

---

First-principles studie van defecten in transparante geleidende oxide materialen

Proefschrift voorgelegd tot het behalen van de graad van doctor in de wetenschappen aan de Universiteit Antwerpen te verdedigen door

Mozhgan Amini

Promotoren
Prof. Dr. Bart Partoens
Prof. Dr. Dirk Lamoen

Antwerpen
January, 2014

Members of the Jury:

Chairman
Prof. Dr. Pierre Van Mechelen, Universiteit Antwerpen, Belgium

Supervisors
Prof. Dr. Bart Partoens, Universiteit Antwerpen, Belgium
Prof. Dr. Dirk Lamoen, Universiteit Antwerpen, Belgium

Members
Prof. Dr. Marlies Van Bael, Universiteit Hasselt, Belgium
Prof. Dr. Michel Houssa, Katholieke Universiteit Leuven, Belgium
Prof. Dr. Sabine Van Doorslaer, Universiteit Antwerpen, Belgium
Prof. Dr. Dominique Schryvers, Universiteit Antwerpen, Belgium

Contact Information

Mozhgan Amini
Department of Physics
University of Antwerp (CGB)
Groenenborgerlaan 171, U313
B-2020 Antwerp, Belgium
+32 (0) 3 265 34 31
Mozhgan.Amini@uantwerpen.be

Acknowledgement

This PhD thesis is the result of a challenging journey. One of the pleasures of completion is to look over the past and remember all the people who have encouraged and supported me along this long but fulfilling road.

First and foremost, I would like to express my sincere gratitude to my promoters Prof. Bart Partoens and Prof. Dirk Lamoen for giving me this opportunity to learn from their expertise in the field and to have the fruitful discussions with them. They always had time to answer my questions and they patiently provided the vision, encouragement and advise necessary for me to proceed throughout my research period. Besides my promoters I would like to thank the members of my thesis committee: Prof. Dr. Pierre Van Mechelen, Prof. Dr. Dominique Schryvers, Prof. Dr. Sabine Van Doorslaer, Prof. Dr. Marlies Van Bael, and Prof. Dr. Michel Houssa who provided constructive feedback with their insightful comments and questions.

My sincere thanks goes to Dr. Rolando Saniz for his kind help, and invaluable advice for better understanding of the results presented in this work. My thanks also go out to my colleagues from the CMT and EMAT group in the University of Antwerp. In particular, I am grateful to Dr. Hemant Dixit, Dr. Ortwin Leenaerts, Dr. Masahiko Matsubara, Kirsten Govaerts, Samira Dabaghmanesh, Nasrin Sarmadian and Dr. Massoud Ramezani Masir for all useful discussions and a cheerful atmosphere we had during these years. I must also thank Stephan Vercauteren and Bob Schoeters for helping in translating the summary of my thesis in Dutch.

I would like to take this opportunity to thank Prof. Dr. François Peeters, head of CMT group, for his kind support and Hilde Evans, the secretariat of the Department of Physics, for her administrative assistance.

I would also like to acknowledge my debt to my former promoters Prof. Dr. Seyed Mohammad Hosseini and Prof. Dr. Ahmad Kompany for inspiring me throughout my earlier studies.

Last but not least, I would like to thank my parents and my two brothers, Majid and Masoud, for their unconditional love, support and encouragement during the hard and easy times of my life. I owe them everything and wish I could show them just how much I love and appreciate them. I would also like to thank my lovely niece, Hasti, and her dearest mother, Azadeh, for their loving support.

And most of all for my loving, supportive, encouraging, and patient friend and husband, Hamed, whose faithful support during this PhD is so appreciated. Thank you!

Mozhgan Amini
Antwerpen - January 2014

Contents

List of Abbreviations

AZO	Aluminium doped zinc oxide
CBM	Conduction band minimum
CRT	Cathode ray tube
CVD	Chemical vapor deposition
DFT	Density functional theory
DLTS	Deep level transient spectroscopy
EELS	electron energy loss spectroscopy
EMT	effective mass theory
EPR	electron paramagnetic resonance
ESR	electron spin resonance
FPD	Flat panel display
FTO	Fluorine doped tin oxide
GGA	Generalized gradient approximation
HAADF	High angle annular dark-field
HK	Hohenberg-Kohn
ITO	Indium tin oxide
KS	Kohn-Sham
LAPW	Linearized augmented plane wave
LCD	Liquid crystal display
LDA	Local density approximation
PAW	Projector augmented wave method
PET	Polyethylene terephthalate
PLD	Pulsed laser deposition
PP	Pseudopotential
STEM	Scanning transmission electron microscopy
TB	Tight-binding
TCO	Transparent conducting oxides
VBM	Valence band maximum
XC	Exchange-correlation

Chapter 1

Introduction

Semiconductor materials have changed and improved the way we live. Semiconductors are a group of materials with an electrical conductivity intermediate to that of conductors (electric charges flow easily) and insulators (electric charges do not flow freely), and are used in almost all technological devices. Semiconductors are one of the fundamental building blocks and basic materials in advanced electronics.

An important property of semiconductors is that their energy gap lies between zero and about 4 eV. Figure 1.1 shows a typical band structure for an insulator, a semiconductor and a metal. The conductivity of semiconductor materials can be tuned in several ways. Subjecting these materials to heat or light, applying an electric or magnetic field, and introducing defects or impurities to their microstructure by doping, are methods that are used to manipulate their conductivity.

The topic of this thesis is a specific group of semiconductors called transparent conducting oxides (TCOs). These materials are transparent and at the same time conducting. In this chapter, basic important properties and a few techniques for the fabrication of TCOs are briefly explained, and finally a number of their applications are listed. The main goal of this thesis is to contribute to the understanding of the conductivity of TCOs using first principles calculations to study native defects and impurities in TCOs. In the next chapter, a brief introduction to the methodology I used to study TCO materials in this thesis is presented. Next the effect of defects and impurities in a TCO material is discussed together with the methods used to calculate their electronic structure. These introductory chapters are followed by the results I obtained.

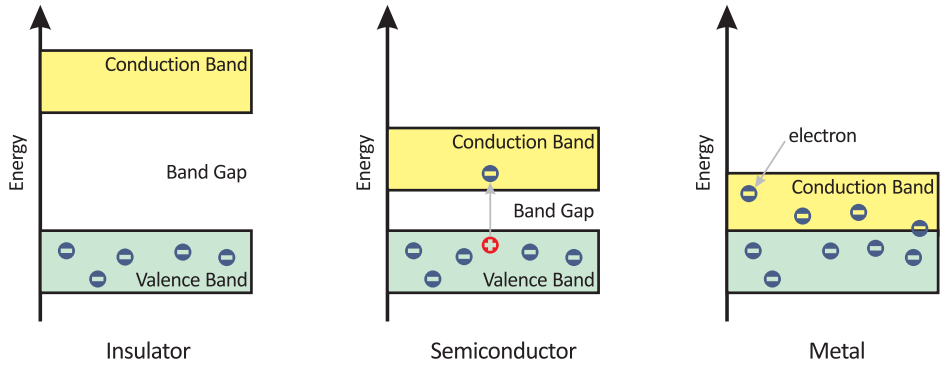

Figure 1.1: Typical band structures of an insulator, a semiconductor, and a metal.

1.1 Transparent conducting oxides

Visible light is made up of the wavelengths of the electromagnetic spectrum in the range of about 380-740 nm or energies in the range of 1.7-3.3 eV. An object can be considered optically transparent if no scattering or absorption takes place in the visible spectral range. For materials with a band gap larger than 3.3 eV, interband transitions do not occur in the visible light range, so, light can pass through them easily hereby making them transparent.

Therefore the optical transparency of a semiconductor material needs a minimum band gap energy of about 3.3 eV. Since this energy (3.3 eV) is too large to transfer electrons into the conduction band at room temperature, one can conclude that high optical transparency is incompatible with high electrical conductivity [1].

Transparent conducting oxides (TCO) are a special group of materials that are both optical transparent and show high electrical conductivity. TCOs are prepared from a wide variety of materials. They are usually normal semiconductors, doped with one or more types of impurities. These dopants together with native defects in these systems, play an important role in controlling the conductivity. So defects contribute to the conductivity in a semiconductor which is already optically transparent. A good TCO material should have an optical transmission above 80% in the visible light range, a carrier concentration of the order of 10^{20} cm^{-3}, and a resistivity of the order of $10^{-3}\Omega$cm [2].

The first TCO films, prepared by thermal oxidation of cadmium, were reported by Bädeker in 1907 [3]. The films were both electrically conducting and optically transparent, but since CdO has a toxic nature, it attracted

little research attention.

Another TCO material In_2O_3:Sn (ITO, tin doped indium oxide) was reported by Rupperecht [4] in 1954. Investigations were continued in order to identify other alternatives as TCOs. Two other important TCO materials which have been investigated intensively since are ZnO:Al (AZO, aluminium doped zinc oxide), and SnO_2:F (FTO, fluorine doped tin oxide).

In addition to these binary oxides, TCOs based on ternary oxides were also developed in the 1980s such as Cd_2SnO_4, $CdSnO_3$, $CdIn_2O_4$, and others. [5, 6] However, the chemical composition of binary compounds in film depositions is easier to control than that of ternaries.

1.2 Basic properties of transparent conductors

There are several important chemical and physical properties related to the performance of TCOs in different applications [7]. Some of them are briefly listed here.

1.2.1 Electrical conductivity

In 1900, a model was proposed by Paul Drude to explain the transport properties of electrons in metals, commonly known as Drude model [8]. He assumed that matter consists of light negatively charged electrons which are mobile, and heavy, static, positively charged ions which are immobile. The only interactions are electron-core collisions, which take place in a very short time span τ. (Long-range interaction between the electrons and the ions or between the electrons were neglected.) Figure 1.2 shows a path of the conduction electrons scattering off the ions in the material, according to the Drude model. Electrons are assumed to achieve thermal equilibrium through collisions, and the probability of an electron suffering a collision in a short time dt is dt/τ, where $1/\tau$ is the scattering rate.

The equation of motion for an electron moving in the crystal is explained by the second law of Newton, and if τ is the average time between collisions, the average drift speed is

$$v_d = \frac{eE\tau}{m_e} \equiv \mu E \tag{1.1}$$

where E is the electric field, m_e is the electron effective mass, and e is the electric charge carried by an electron. One can also rewrite the average drift

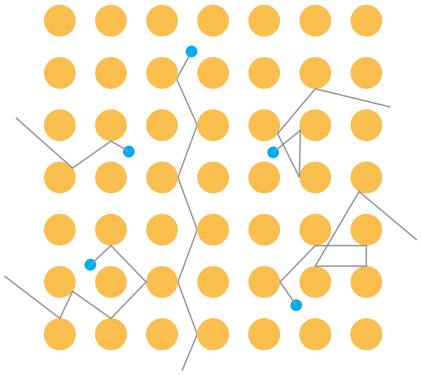

Figure 1.2: Path of the conduction electrons scattering off the ions in the material, according to the Drude model.

speed with respect to the mobility μ of the charge carriers. In conclusion, the Drude conductivity of the material as a function of the number of charge carriers n is given by

$$\sigma = \frac{ne^2\tau}{m_e} = n\mu e \tag{1.2}$$

The relation above clearly shows the dependence of the conductivity of the material on the number of charge carriers n, their effective mass m_e, and the relaxation time τ. Therefore in a semiconductor material, conductivity can be improved by increasing either the carrier concentration or their mobility. For example by doping a material with impurities and introducing defects in it, one can increase the number of charge carriers and thus the conductivity of the material.

On the other hand, the conductivity can also be improved by increasing the mobility of the carriers in the system. The mobility itself depends on the effective mass of the carriers, and the relaxation time. For a free electron with mass m_e^0, it is known that the energy relates to the wavevector through the relation $\epsilon = (\hbar^2/2m_e^0)k^2$. So the coefficient of k^2 determines the curvature of ϵ versus k. In a similar approach, the lower conduction band in a crystal can be approximated with a parabola around its minimum. For isotropic bands, the coefficient of k^2 is then proportional to a so called effective mass, m_e expressed as

$$\frac{1}{m_e} = \frac{1}{\hbar^2}\frac{d^2\epsilon_k}{dk^2} \tag{1.3}$$

where ϵ_k is the energy of the carrier in the periodic potential and k is the

wave vector. The value for the electron effective mass is thus related to the curvature of the lower conduction band. The lower the curvature, the higher the effective mass and vice versa (a similar procedure is also valid for holes).

1.2.2 Plasma frequency

According to the Drude model, due to the effect of the electric field, the electrons can oscillate in a cloud performing a collective motion and oscillating at a certain frequency which is called the plasma frequency. In the following sections, the important role of the plasma frequency on the optical properties of the semiconductor materials is explained. The plasma frequency is a threshold frequency as for all lower frequencies the material reflects an incident radiation and at higher frequencies the material acts as an optically transparent object. It should be noted that for higher frequencies in the UV part of the spectrum, the radiation energy is high enough to overcome the band gap and the material will absorb incident radiation.

Assuming an electron moving in a time-dependent electric field $\mathbf{E}(t)$ in the crystal, the equation of motion can be written as

$$m_e \frac{d^2\mathbf{x}(t)}{dt^2} = e\mathbf{E}(t) \tag{1.4}$$

An alternating electric field is given by $\mathbf{E}(t) = Ee^{-i\omega t}$. By putting the time-dependent electric field and also $\mathbf{x}(t) = xe^{-i\omega t}$ in the equation of motion, one finds

$$-m_e\omega^2 x = eE \quad \Longrightarrow \quad x = \frac{-eE}{m_e\omega^2} \tag{1.5}$$

For a carrier concentration n, the polarization P is given by

$$P = nex \quad \Longrightarrow \quad P = \frac{-ne^2E}{m_e\omega^2} \tag{1.6}$$

and the electric displacement field due to the polarization is

$$D = \epsilon_0\epsilon E = \epsilon_0 E + P \quad \Longrightarrow \quad \epsilon = 1 + \frac{P}{\epsilon_0 E} \tag{1.7}$$

using Eq.(1.7) the dielectric function can also be written as

$$\epsilon = 1 - \frac{\omega_p^2}{\omega^2} \quad ; \quad \omega_p = \sqrt{\frac{ne^2}{\epsilon_0 m_e}} \tag{1.8}$$

The plasma frequency is denoted as ω_p in the equation above. It is interesting to note that the plasma frequency is directly related to the square root of the carrier concentration n, and also inversely proportional to the square root of the effective mass of the carrier. Therefore the plasma frequency of a chosen compound can be manipulated by tuning the amount of charge carriers and choosing a host material with a desired effective mass, according to the specific application.

1.2.3 Optical transparency

There is an alternative way to explain the interaction of light with a medium. Once light passes through a medium, a fraction of it will be absorbed. This phenomenon can be taken into account by defining a complex index of refraction

$$\tilde{n}(\omega) = \eta + i\kappa \tag{1.9}$$

The real part η determines the phase velocity while the imaginary part κ indicates the amount of absorption when the electromagnetic wave propagates through the material. The imaginary part is known as the extinction coefficient and both η and κ are functions of the frequency.

Let us consider an electric field of a plane electromagnetic wave traveling in the z direction

$$E(z,t) = E_0 e^{i(\tilde{k}z - \omega t)} \tag{1.10}$$

$\tilde{k}$ is the wave number which is related to the refractive index through $2\pi\tilde{n}/\lambda_0$, where λ_0 represents the vacuum wavelength. By a simple substitution of the complex value of $\tilde{k}$, the plane wave expression becomes

$$Re(E_0 e^{i(\tilde{k}z - \omega t)}) = e^{\frac{-2\pi\kappa z}{\lambda_0}} Re(E_0 e^{i(kz - \omega t)}) \tag{1.11}$$

where $k = 2\pi\eta/\lambda_0$. It is clear from this equation that for $\kappa > 0$ the penetrating wave drops off exponentially in the medium (light is absorbed). In case of $\kappa = 0$ the wave travels forever undisturbed. There are even special situations (e.g. in the gain medium of lasers) when $\kappa < 0$ which means the wave is amplified by the medium.

The dielectric function $\epsilon(\omega)$ of a non-magnetic material is alternatively related to the refractive index $n(\omega)$ by

$$\epsilon(\omega) = \tilde{n}^2(\omega) \tag{1.12}$$

In Fig. 1.3, the spectral dependence of TCO materials is schematically shown. ω_{gap} and ω_p are the frequencies at which the band gap absorption and free electron plasma absorption takes place. For $\omega < \omega_p$, ϵ has a negative value and the imaginary part of the refractive index is large. Like in the case of $\kappa > 0$, the penetrating wave drops off exponentially in the material without any propagation, and as a result the material is opaque and has a near unity reflectance. If $\omega_p < \omega < \omega_{gap}$, ϵ is positive and the imaginary part of the refractive index is almost zero. So, the light wave will propagate in the material which then acts as transparent in this region, and finally for $\omega > \omega_{gap}$, the photon energy is high enough to overcome the band gap energy and will be absorbed by the material. The plasma frequency for most TCOs falls in the near infrared part of the spectrum. Therefore the visible light is in the higher frequency range, making these materials transparent to the visible light.

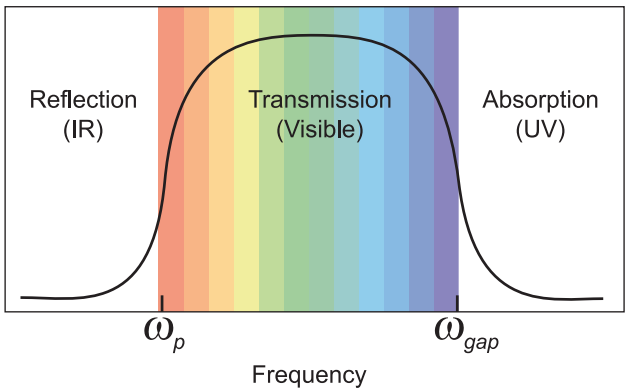

Figure 1.3: Transmission of the material with respect to the external applied energy. The middle part is considered as the `*optical window*´.

1.2.4 TCO material selection examples

There is no specific TCO material suitable for all applications. Depending on which material property is of most importance, different selections are made. For example, the ability of a TCO material to reflect thermal infrared heat is used to make energy-conserving windows for which this selection is made on ω_p. As another example, the electrical conductivity of a TCO is used in front-surface electrodes for solar cells and flat-panel displays in which the dopability is more important. Table 1.1 summarizes some of the most significant criteria that may influence the choice of a transparent conducting

material[1].

Table 1.1: TCO materials and their specific properties [7].

Property	Materials
Highest conductivity	$In_2O_3 : Sn$
Lowest plasma frequency	$SnO_2 : F$, $ZnO : F$
Highest plasma frequency	$In_2O_3 : Sn$
Highest transparency	$ZnO : F$, Cd_2SnO_4
Highest work function (best contact to p-Si)	$SnO_2 : F$, $ZnSnO_3$
Lowest work function (best contact to n-Si)	$ZnO : F$
Best thermal stability	$SnO_2 : F$, Cd_2SnO_4
Best mechanical durability	$SnO_2 : F$
Best chemical durability	$SnO_2 : F$
Easiest to etch	$ZnO : F$
Lowest deposition temperature	$In_2O_3 : Sn$, $ZnO : B$
Least toxic	$ZnO : F$, $SnO_2 : F$
Lowest cost	$SnO_2 : F$

1.3 Defects and impurities in TCO materials

Doping as well as the presence of native point defects alters the number of charge carriers (electrons for '*n-type*' and holes for '*p-type*') in semiconductors and can highly affect their conductivity. Figure 1.4 shows the representation of the electronic band structure of a TCO material in both undoped, and doped cases. In the doped case, the Fermi level (E_F) is pushed up into the conduction band and makes the system conductive.

So the study of defects and impurities is an important research area in semiconductor physics. They are used to control the electronic and opto-electronic properties of materials. However, to achieve such control, the knowledge of the fundamental processes that dominate the doping is necessary. First-principles calculations have already made important contributions to the understanding of these fundamental processes of doping in different semiconductors [9].

[1]Some of the most utilized materials do not appear in the list of Table 1.1. For example $ZnO : Al$ is often second best for several TCO material properties and therefore does not appear in the list.

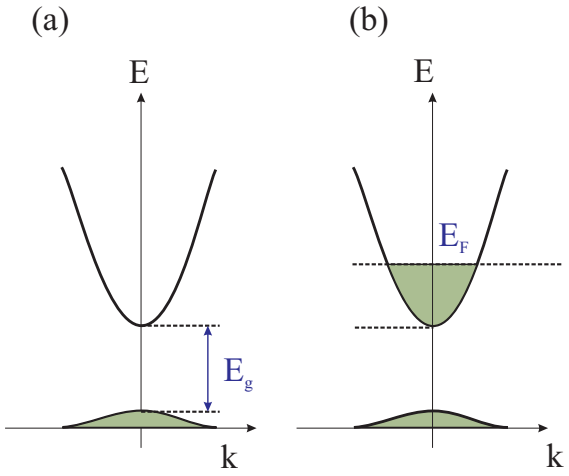

Figure 1.4: Representation of the electronic band structure of a TCO material in (a) undoped, and (b) doped cases where the Fermi level (E_F) is pushed up into the conduction band and makes the system conductive.

1.4 Fabrication of TCOs

TCO films are prepared by different deposition techniques [10]. In the following some of these techniques are briefly explained.

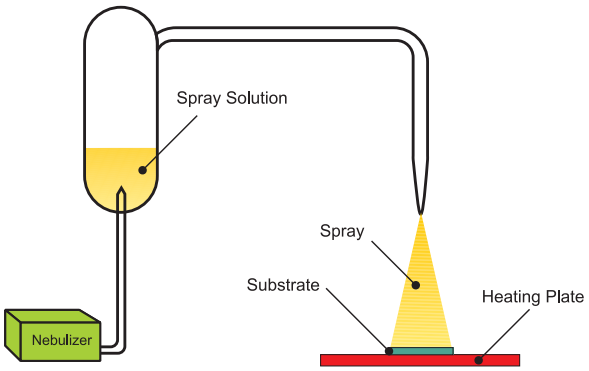

Figure 1.5: General schematic of a spray pyrolysis deposition process.

- Spray pyrolysis : This process is one of the most inexpensive and commonly used techniques for the preparation of TCO films. In this process, an ionic solution containing the constituent elements of a compound in the form of soluble salts (e.g. aqueous solution of $SnCl_4.5H_2O$ for deposition of SnO_2 thin films) is sprayed onto a heated surface (un-

der normal atmospheric conditions) where the constituents react to form a desired solid film. A schematic drawing of the process is shown in Fig. 1.5.

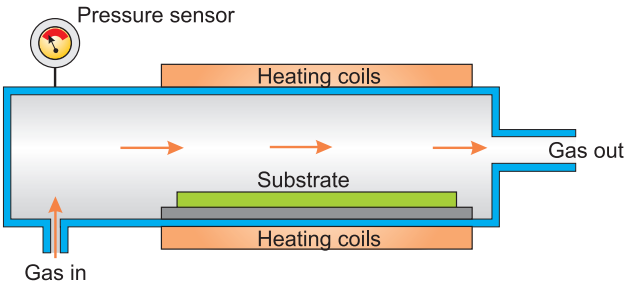

Figure 1.6: General schematic of a CVD chamber (reproduced from [11]).

- Chemical vapor deposition (CVD) : CVD is a commonly used technique to fabricate TCO thin films [12]. The method results in a layer with high purity, since it involves an atomic deposition of material on the substrate. In the CVD process, gaseous precursors decompose at the heated substrate in a chamber with controlled atmosphere and produce the desired thin film. Figure 1.6 illustrates a typical CVD chamber.

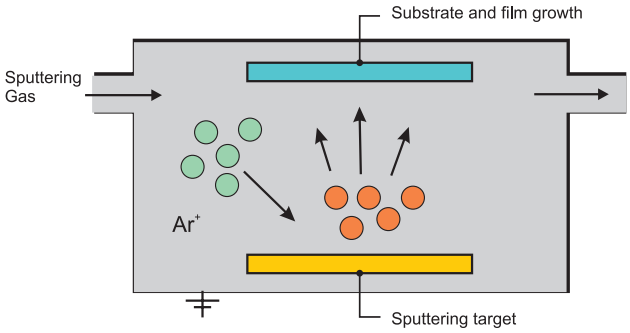

Figure 1.7: General schematic of sputtering process (reproduced from [13]).

- Sputtering : An alternative technique used to prepare thin film coatings is sputtering. This method is even applicable to materials with very high melting points. In this method, it is not needed to heat the substrate since atoms are sputtered of a target and are deposited onto a substrate as a thin film. Usually an inert gas with an atomic weight

close to the target is used as the sputtering gas. The process is depicted in Fig. 1.7.

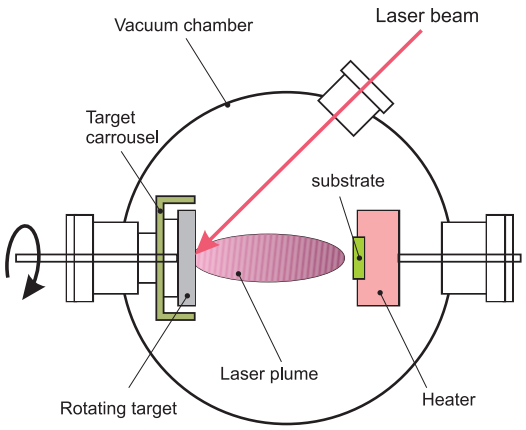

Figure 1.8: General schematic of PLD process (reproduced from [14]).

- Pulsed laser deposition (PLD) : This is another powerful technique for the preparation of TCO films. It is not yet applicable for large scale commercial applications. In this physical vapor deposition method, a substrate is placed in a vacuum chamber and a laser beam is used to evaporate the material. Then, by condensing the vaporized material, it is deposited on the substrate and forms a thin film. The procedure is schematically shown in Fig. 1.8.

Nevertheless, different growth methods will lead to films with different amounts and types of defects. For example, it is clear that in sputtering methods more defects with high formation energies will be formed than in CVD growth that leads to more crystalline films. Even the substrate in the deposition method plays an important role in the final structure of the thin film. Research revealed that films prepared by sputtering deposited on single crystalline substrates exhibit a significantly higher density of defects than the films deposited on an amorphous substrate. This is most probably due to a higher density of misfit dislocations, which compensate for the lattice mismatch between the film and the substrate [15]. Apart from the manufacturing process most of the techniques are combined with a subsequent annealing process to reduce the inappropriate crystal defects [16].

1.5 Applications

TCOs are a technologically important class of materials that combines electrical conductivity and optical transparency together. TCOs are essential for many photovoltaic and optoelectronic applications. Some of these applications are briefly described in the following.

Generally TCO materials can be categorized according to their electronic properties. N-type TCO material contains excess free electrons in the structure, while there is a deficiency of electrons in a p-type TCO material. It should be noted that there are already many known n-type TCOs, but the lack of good p-type TCOs limits the presence of active electronic devices which can be fabricated with both n- and p-type TCOs. Delafossite $CuXO_2$ (X=Al, Ga and In) oxides were a first group of p-type materials which are studied since 1997 and triggered the development of a series of p-type TCOs [17].

1.5.1 Photovoltaic cell

A photovoltaic cell is used to convert the energy of light into electrical current. If this emission energy comes from the sun, then the cell is called a solar cell. Harnessing solar energy which is a long lasting source provides a very economical way of producing power.

Photovoltaic cells require at least one electrode that can provide both optical transparency and electrical conductivity. The transparent conducting electrode acts as a transparent medium over much of the solar spectrum. The electrode allows light to pass through to the active layer beneath (where carrier generation occurs), and it also acts as a conductor for charge transport out of the photovoltaic cell. However there are some other crucial requirements for such transparent electrodes (e.g. interfacial properties, materials compatibility, chemical stability, etc.) as well. [18]

In a typical photovoltaic cell, the top layer consists of a transparent material that is either glass or flexible plastic. Then there is an electrode, consisting of a TCO layer coated with very thin n-type (or p-type) interfacial materials. On the other side there is another electrode coated with very thin p-type (or n-type) interfacial materials and as a result of this p-n junction there will be an active absorber layer (a mixture of donors and acceptors) in the middle. (Such an arrangement is schematically shown in Fig. 1.9.)

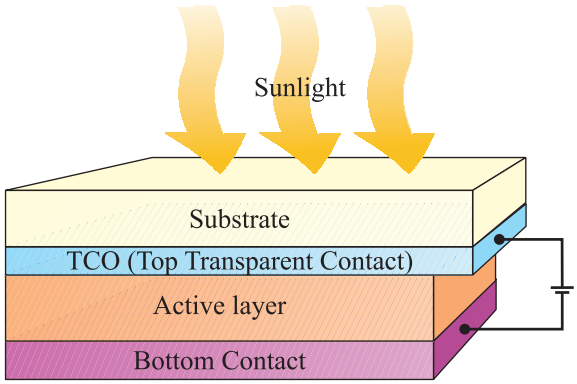

Figure 1.9: A schematically drawing depicting multiple layers in a typical solar cell.

When light shines on the photovoltaic cell, its energy (photons) ionizes the atoms and creates electron hole pairs in the cell, allowing them to flow freely and form a current. Contacts on the top and bottom of the cell draw off the current to use externally as power. Apart from the active layer, the amount of power is also determined by the type and area of the electrodes, the intensity and the wavelength of the sunlight.

In the production of solar cells, thermal stability and low cost are the primary factors for the selection of TCOs. The most extensively used material in photovoltaic cells is $SnO_2 : F$ which is used as a heat reflecting coating and a transparent electrode for amorphous silicon and cadmium telluride based solar cells [7].

1.5.2 Smart windows

Smart windows are made of glasses containing a glazing material to control the amount of light transmission through the glass. The glazing on the glass is essentially a TCO material such as ITO or AZO.

As discussed before, the optical transparency of a TCO material highly depends on its plasma frequency which itself can be tuned by changing the carrier concentrations and effective masses. Therefore TCOs are good candidates to be used as glazing material in smart windows. Since for frequencies smaller than the plasma frequency, a TCO material reflects the infrared part of light, it is used to control the temperature indoors in cold and hot climates as shown in Fig. 1.10 and 1.11. For example, titanium nitride is a suitable choice for its durability combined with a short plasma wavelength which can reflect the sunlight out of the building [7].

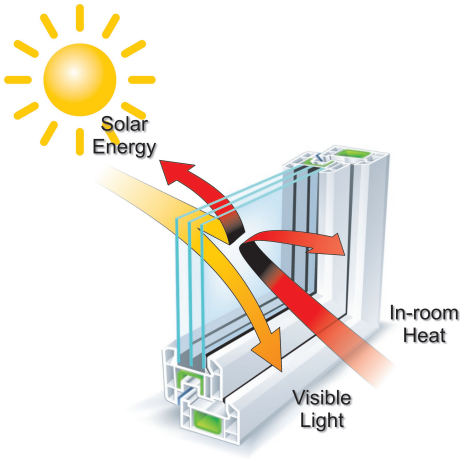

Figure 1.10: Schematics of a smart window. The TCO coating can either block or allow the IR part of light thereby allowing control over room temperature.

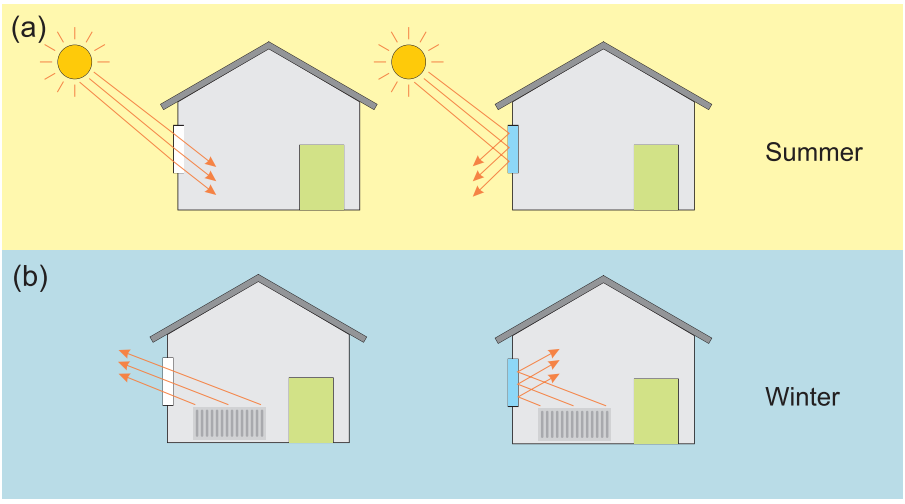

Figure 1.11: (a) In summer, the smart window reflects the heat coming from the outside before being absorbed in the room, thus keeping the house cooler. (b) In winter, the smart window reflects the heat coming from the house before it goes outside and keeps the home warmer.

TCOs can also be used to increase the safety of an oven window by maintaining the outside temperature of the glass. They can also be used to make

defrosting windows in freezers. These windows prevent the condensation of water vapor and remain an ice-free surface.

1.5.3 Touch panels

Touch panels are electronic visual displays by which the user can control the device through touching the screen. They are used in several devices such as smartphones and tablets, navigation systems, and ATM machines. The durability and low cost of tin oxide make it a good choice for this application [7]. Generally there are two types of touch panels:

- Resistive touch panels : These touch panels are based on the pressure applied to the screen with a finger, or any other object. They consist of two layers (film or glass) each covered by a transparent conducting material (usually ITO because of its good durability) which are separated by a gap between them. There are some spacing dots (insulators) between two layers which prevent unintended contacts of the layers. When the panel is touched, the top layer is pressed down and the two layers contact and causes cascade of signals and as a result a command will be registered.

  These panels, which rely on mechanical pressure have a slightly long response time and are unable to provide multi-touch functioning, however they are insensitive to the medium which triggers the mechanical pressure.

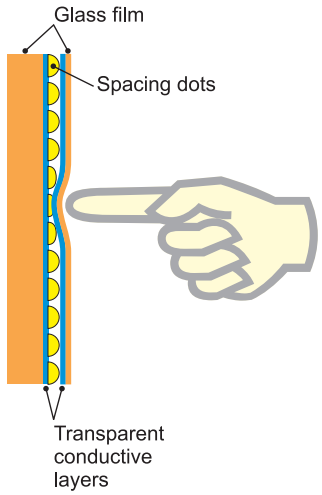

Figure 1.12: Schematic of a touch panel.

- Capacitive touch panels : These panels are based on the electrical properties of the touching object (e.g. conductivity of the human body). They usually consist of one insulating layer (film or glass) which is covered by a transparent conductive material on one side. When the panel is touched with the finger, a change in the screen's electrical field occurs. This change is registered, and the coordinates of the touch are determined.

  These panels are highly responsive to the slightest touch and also allow multi-touch functioning. They are more expensive to manufacture compared to the resistive ones, but they provide a more pleasant user experience.

1.5.4 Flat panel displays

Flat panel displays are a class of display devices with longer durability, lighter weight and inexpensive display components. Figure 1.13 shows the evolution of the electronic visual displays from the bulky cathode ray tube (CRT) display to the thin liquid crystal display (LCD) and finally to the more advanced paper-like flat panel displays (FPD).

Figure 1.13: Evolution of display technology from the CRT display to the LCD and finally to the FPDs.

Most of the FPDs use LCD technologies in which a thin layer of liquid crystal is located in between two transparent conducting plates and each of these plates is connected to a polarizer filter. When an incident un-polarized light shines to the top layer, it becomes polarized in one direction and moves through the liquid crystal causing the molecules to be aligned with respect to the applied electric field. Different applied electric fields, activate different

segments of the liquid crystal and cause changes in the diffusion and the polarization properties of the light. So segments can block or transmit light and make an image by passing it through specific segments. At the bottom, light passes through a final polarized filter which is rotated 90° from the first filter. This one is also covered with a transparent conductor material. So if the light is rotated during its path from the first filter, then it will pass through the second one with its maximum intensity (see Fig. 1.14). FPDs are used in almost all modern flat-panel displays, such as laptops, tablets, TVs, video games, consumer electronics, etc. The most extensively used material is tin-doped indium oxide (ITO). The properties of ITO which are particularly interesting for this application include etchability, low deposition temperature and low resistance [7].

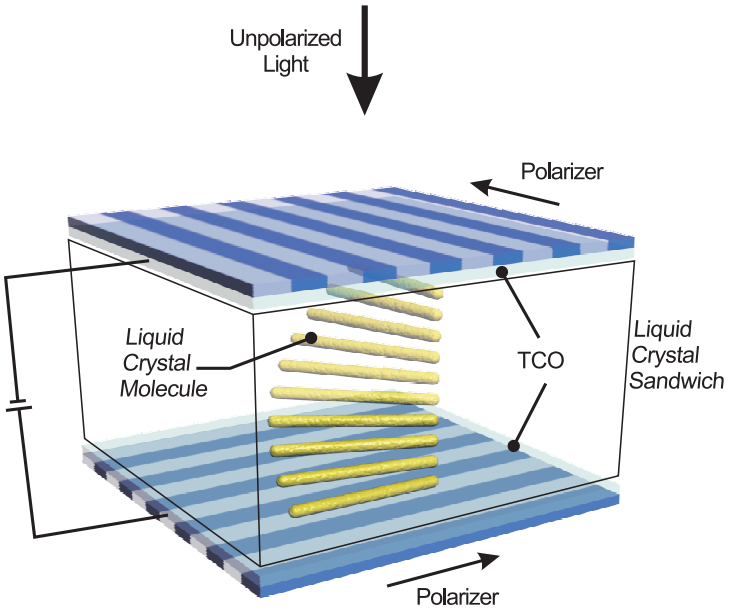

Figure 1.14: Demonstration of a FPD.

1.5.5 TCO application growth

The touch panel transparent conductive film market was $956 million in 2012 and is expected to reach $4.8 billion by 2019 [19]. ITO is the basis of more than 90% of the transparent conductive films in touchscreens. However due to the increasing demand in the market the price of Indium has increased dramatically. On the other hand sputtered ITO layer on plastic films are

known to be brittle and crack upon a few percent strain. Therefore many researches have been devoted to the development of new transparent conducting materials with improved functionality and lower production costs.

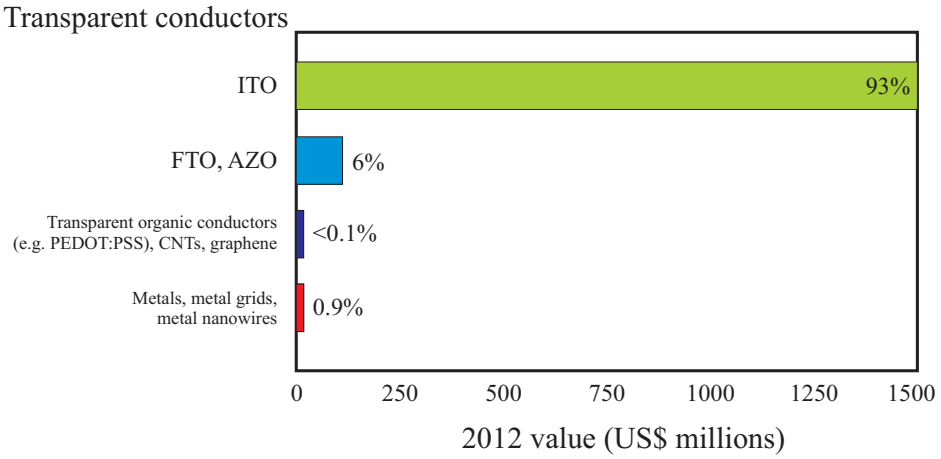

Figure 1.15: The commonly used TCOs (in displays, photovoltaics, or touchscreens) with their market share in 2012[19].

Note that other than oxide materials are also proposes as transparent conductor materials. An alternative for ITO films which meets the flexibility requirement and price of production for those application are hybrid transparent conductive films based on nano silver and PEDOT:PSS (poly(3,4-ethylenedioxythiophene) poly(styrenesulfonate)) polymer mixture[19]. Figure 1.15 shows commonly used TCO materials with their market share in 2012.

1.6 Outline of the thesis

The aim of this thesis is to achieve an accurate description of the electronic structure of TCO materials, using density functional theory (DFT), and to create an understanding of the fundamental processes that control doping in a few particular TCOs in order to develop the knowledge about these materials.

In **chapter 2** a brief overview is given on the DFT calculations (the theoretical method used throughout this thesis) and several ways to solve the Kohn-Sham equations.

Chapter 3 contains an introduction on different kinds of defects and impurities. Since point defects and impurities have profound effects on the

electronic properties of materials, some important parameters such as their formation energies and transition levels are briefly explained.

In **chapter 4** of the thesis, we have used first principles calculations to study point defects in CdO based on density functional theory within the local density approximation and beyond (LDA+U). We have investigated the donor and/or acceptor character of the hydrogen impurity in CdO, and the most likely occurring native defects in CdO, namely the oxygen vacancy, the cadmium vacancy, the oxygen interstitial and the Cd interstitial by ab initio calculations.

In **chapter 5**, we have studied the electronic structure and formation energies of substitutional group III elements (Al, Ga, In) doped in ZnO. We have applied two correction schemes for the band gap values and we have made a comparison between these two approaches.

Further, in **chapter 6**, we have considered the two shallow donors interstitial hydrogen H_i and substitutional X_{Zn} with X = Al, Ga or In in ZnO. Furthermore we have studied by first-principles calculations the codoping of ZnO with hydrogen and a group III element (Al, Ga, or In).

Chapter 7 deals with ZnM_2O_4 (M=Co, Rh, Ir) spinel structures as a class of potential p-type transparent conducting oxides (TCO). We have studied the formation energy of acceptor-like defects using first principles calculations with an advanced hybrid exchange-correlation functional (HSE06) within density functional theory (DFT).

Finally in the last chapter, **Chapter 8**, we propose a method to determine the transition levels between different charge states without explicitly calculating the formation energy of a defect in a charged state. This method allows now the study of defects in nanostructures, for which the standard approach is not valid. We have shown the validity of our approach by considering the oxygen vacancy V_O in bulk ZnO. Next we have applied this approach to the same defect in a ZnO slab.

Chapter 2

Density Functional Theory

2.1 Introduction

The computational modeling of different structures of materials and their properties can be very useful and valuable in developing materials and their applications. They can also be used for interpretation of experimental results. Since the computer simulations offer acceptable accuracy in prediction of materials properties, they are widely used in the development of new materials.

In this chapter, one of the theoretical frameworks that are used nowadays for electronic structure calculations in the field of condensed matter is introduced. The basics of the density functional theory (DFT), a quantum mechanical approach for ground state calculations, are explained. DFT is used in this thesis to calculate the electronic structure of defects in TCO materials. The content of this chapter is based on Richard M. Martin's book on electronic structure calculations [20], which the reader may refer to for more details.

2.2 The time-independent Schrödinger equation

The time-independent Schrödinger equation for a crystal is a partial differential equation that describes a system of atomic nuclei and their surrounding electrons.

$$H\Psi(\mathbf{r}_1, \mathbf{r}_2, ..., \mathbf{R}_1, \mathbf{R}_2, ...) = E\Psi(\mathbf{r}_1, \mathbf{r}_2, ..., \mathbf{R}_1, \mathbf{R}_2, ...) \tag{2.1}$$

where H, E, and Ψ are the Hamiltonian, the electronic energy, and the many-body wave function of the system, and $\mathbf{r}_i$ and $\mathbf{R}_i$ are the positions of the electrons and ions respectively (capital indices refer to the nuclei and small indices to the electrons). The Hamiltonian of the system is given by

$$H = -\sum_i \frac{\hbar^2 \nabla_i^2}{2m_e} - \sum_I \frac{\hbar^2 \nabla_I^2}{2M_I} + \frac{1}{2}\sum_{i \neq j} \frac{e^2}{|\mathbf{r}_i - \mathbf{r}_j|} + \frac{1}{2}\sum_{I \neq J} \frac{Z_I Z_J e^2}{|\mathbf{R}_I - \mathbf{R}_J|} - \sum_{i,I} \frac{Z_I e^2}{|\mathbf{r}_i - \mathbf{R}_I|} \tag{2.2}$$

where M_I and Z_I are the atomic mass and charge of the nucleus, and e is the electron charge. In the Hamiltonian above, the first two terms correspond to the kinetic energy of the electrons (T_e) and nuclei (T_N) respectively. The third and forth terms indicate the Coulomb interaction between electrons (internal potential V_{int}) and nuclei (V_{II}), respectively, and the last term corresponds to the electrons-nuclei Coulomb interactions (external potential V_{ext}). For simplicity, atomic units will be used in the following ($\hbar = m_e = e = 1$). So, the fundamental Hamiltonian can be written as

$$H = T_e + T_N + V_{int} + V_{II} + V_{ext} \tag{2.3}$$

There are several approximations in order to solve this quantum many-body problem. Some of them are briefly explained in the following.

2.3 Born-Oppenheimer approximation

The Born-Oppenheimer approximation [21] is an approach to simplify the Schrödinger equation of the coupled nucleus-electron system. It is based on the fact that the mass of a nucleus is almost infinity comparing to the mass of an electron and the velocity of a nucleus is much less than that of an electron, so the kinetic energy of the nuclei can be ignored in the Hamiltonian. Therefore, electrons are moving in the array of fixed nuclei with a constant potential energy (V_{II}), and the total electronic Hamiltonian becomes

$$H_{tot} = T_e + V_{int} + V_{II} + V_{ext} \tag{2.4}$$

In this approximation, the nuclear positions enter as parameters (this means that for different coordinates of the nuclei, the electronic wave function changes, which is the only dependence of this function on the nuclear coordinates) in the electronic wave function, so the electronic Hamiltonian and the corresponding Schrödinger equation are

$$H_{elec} = T_e + V_{int} + V_{ext} \tag{2.5}$$

$$H_{elec}\Psi_{elec}(\mathbf{r}_1, \mathbf{r}_2, ...) = E_{elec}\Psi_{elec}(\mathbf{r}_1, \mathbf{r}_2, ...) \tag{2.6}$$

We omit explicitly the parametric dependence of Ψ_{elec} on $\mathbf{R}_I$. The total energy E_{tot} is then the sum of E_{elec} and the constant nuclear repulsion term E_{nuc} which comes from the constant potential energy V_{II}

$$E_{tot} = E_{elec} + E_{nuc} \tag{2.7}$$

2.4 The Hartree approximation

The simplest solution for the many-body equation is the Hartree approximation [22, 23, 24]. In this approximation, the Schrödinger equation is written as a one-particle equation and the total wave function is a product of all one-particle wave functions

$$\Psi_{elec}(\mathbf{r}_1, \mathbf{r}_2, ..., \mathbf{r}_n) = \Phi_1(\mathbf{r}_1)\Phi_2(\mathbf{r}_2)...\Phi_n(\mathbf{r}_n) \tag{2.8}$$

so each electron moves independently and sees the average potential generated by all the other electrons. From now on Ψ_{elec} will be denoted as Ψ.

The variational principle in quantum mechanics states that if E_0 is the ground state energy solution of the Schrödinger equation, for any wave function ϕ

$$E_0 \leq \frac{\langle\phi|H|\phi\rangle}{\langle\phi|\phi\rangle} \tag{2.9}$$

Now the Hartree wave function can be used with equation (2.6) and the variational principle to obtain the Hartree equation

$$\left[-\frac{\nabla^2}{2} - \sum_I \frac{Z_I}{|\mathbf{r}_i - \mathbf{R}_I|} + \sum_j \int d\mathbf{r}_j \Phi_j^*(\mathbf{r}_j)\frac{1}{|\mathbf{r}_i - \mathbf{r}_j|}\Phi_j(\mathbf{r}_j)\right]\Phi_i(\mathbf{r}_i) = \epsilon_i\Phi_i^*(\mathbf{r}_i) \tag{2.10}$$

where each independent electron i feels an effective potential of all electrons by an integration over their densities. Therefore the main many-body equation is divided into n simpler one-electron equations, and since for each wave function the potential depends on all wave functions, it has to be solved self consistently.

2.5 The Hartree-Fock approximation

The Hartree wave function in equation (2.8) neglects an important property of electrons. It neglects the fact that electrons are Fermi particles, and their wave functions must be antisymmetric with respect to interchanging any pair of particles

$$\Psi(\mathbf{r}_1, ...\mathbf{r}_k, ...\mathbf{r}_m, ...\mathbf{r}_n) = -\Psi(\mathbf{r}_1, ...\mathbf{r}_m, ...\mathbf{r}_k, ...\mathbf{r}_n) \tag{2.11}$$

The Hartree wave function can be corrected by considering a linear combination of products, and the expression for Fermions can be written as a determinant. For an n-electron system, the Slater determinant is defined as [25]

$$\Psi(\mathbf{r}_1, \mathbf{r}_2, ..., \mathbf{r}_n) = \frac{1}{\sqrt{n!}} \begin{vmatrix} \Phi_1(\mathbf{r}_1) & \Phi_1(\mathbf{r}_2) & \dots & \Phi_1(\mathbf{r}_n) \\ \Phi_2(\mathbf{r}_1) & \Phi_2(\mathbf{r}_2) & \dots & \Phi_2(\mathbf{r}_n) \\ \vdots & \vdots & & \vdots \\ \Phi_n(\mathbf{r}_1) & \Phi_n(\mathbf{r}_2) & \dots & \Phi_n(\mathbf{r}_n) \end{vmatrix} \tag{2.12}$$

each line of the determinant corresponds to a certain one-electron state, and each column to a certain position in space. The wave function changes sign when two particles (here two rows or columns of the determinant) interchange. Furthermore, if two rows or columns are identical then the determinant equals zero, which means that such a situation (two identical particles occupying the same spatial coordinates) is not physically possible.

Using the Slater determinant with equation (2.6) and the variational principle, the Hartree-Fock equation can be derived as

$$\begin{aligned} \left[-\frac{\nabla^2}{2} - \sum_I \frac{Z_I}{|\mathbf{r}_i - \mathbf{R}_I|} + \sum_j \int d\mathbf{r}_j \Phi_j^*(\mathbf{r}_j) \frac{1}{|\mathbf{r}_i - \mathbf{r}_j|} \Phi_j(\mathbf{r}_j) \right] \Phi_i(\mathbf{r}_i) \\ - \sum_j \left[\int d\mathbf{r}_j \Phi_j^*(\mathbf{r}_j) \frac{1}{|\mathbf{r}_i - \mathbf{r}_j|} \Phi_i(\mathbf{r}_j) \right] \Phi_j(\mathbf{r}_i) = \epsilon_i \Phi_i^*(\mathbf{r}_i) \end{aligned} \tag{2.13}$$

This equation has an extra term compared to the Hartree equation. This term is called the exchange potential, since it comes from considering a constraint related to the exchange of particles. The exchange term also cancels an unphysical self-interaction of electrons in the Hartree equation.

2.6 Basics of density functional theory

From the Born-Oppenheimer approximation, it follows that it is enough to solve the many-electron Schrödinger equation. The Hartree-Fock approach changes the many-body interacting problem to an independent one electron problem that can be solved. It also accounts for the anti-symmetric nature of the wave function through the exchange term.

However since the exact wave function cannot generally be expressed as a single determinant, there is still a difference between the exact energy and the Hartree-Fock energy which is called the correlation energy. Several methodologies such as the Møller-Plesset (MP) perturbation theory [26], the configuration interaction (CI) [27] approach, or the coupled cluster (CC) [28] method, were developed to include this effect. Density functional theory is known as one of the most successful quantum mechanical solutions of the many-electron Schrödinger equation to calculate the ground state energy of a system.

In the following sections, the basics of the density functional theory are explained. First a theoretical proof that the density can be considered as the basic variable is given (the Hohenberg-Kohn theorems). This is followed by a methodology to solve the problem by mapping it onto a system of non-interacting particles (the Kohn-Sham equations). Finally the exchange-correlation (XC) energy, the periodic boundary conditions in the crystal, and pseudopotentials are briefly discussed.

2.7 The Hohenberg-Kohn theorems

Density functional theory is based on the two Hohenberg-Kohn (HK) theorems [29], which are mentioned below:

- **Theorem I** : *For any system of interacting particles in an external potential $V_{ext}(\boldsymbol{r})$ the potential $V_{ext}(\boldsymbol{r})$ is determined uniquely, except for a constant, by the ground state density $n_0(\boldsymbol{r})$.*

- **Theorem II** : *A universal functional for the energy $E[n]$ in terms of the density $n(\boldsymbol{r})$ can be defined, valid for any external potential $V_{ext}(\boldsymbol{r})$. The exact ground state energy of the system is the global minimum of this functional and the density that minimizes the functional is the exact ground state density $n_0(\boldsymbol{r})$.*

The first theorem states that the ground state electron density uniquely determines an external potential, the Hamiltonian, and thus all the properties

of the system. To prove this theorem, assume that there are two different external potentials $V_{ext}(\mathbf{r})$ and $V_{ext}^{'}(\mathbf{r})$, each giving the same ground state density $n_0(\mathbf{r})$. So, there will be two Hamiltonians H and $H^{'}$, two normalized wave functions Ψ and $\Psi^{'}$, and two ground-state energies E_0 and $E_0^{'}$. Applying the variational principle of Eq.(2.9) for E_0 with $\Psi^{'}$ as a trial wave function (assuming that $\Psi^{'}$ is normalized to 1) yields:

$$E_0 < \langle \Psi^{'} | H | \Psi^{'} \rangle = \langle \Psi^{'} | H^{'} | \Psi^{'} \rangle + \langle \Psi^{'} | H - H^{'} | \Psi^{'} \rangle \tag{2.14}$$

$$E_0 < E_0^{'} + \int n_0(\mathbf{r})[V_{ext}(\mathbf{r}) - V_{ext}^{'}(\mathbf{r})]d\mathbf{r} \tag{2.15}$$

Similarly, considering Ψ as a trial wave function gives

$$E_0^{'} < \langle \Psi | H^{'} | \Psi \rangle = \langle \Psi | H | \Psi \rangle + \langle \Psi | H^{'} - H | \Psi \rangle \tag{2.16}$$

$$E_0^{'} < E_0 + \int n_0(\mathbf{r})[V_{ext}^{'}(\mathbf{r}) - V_{ext}(\mathbf{r})]d\mathbf{r} \tag{2.17}$$

Summing (2.15) and (2.17) leads to

$$E_0 + E_0^{'} < E_0^{'} + E_0 \tag{2.18}$$

which is a contradiction, and so there cannot be two different potentials that give the same density for their ground state.

The total energy can be written as

$$E_{HK}[n] = T_e[n] + E_{int}[n] + E_{ext}[n] = F_{HK}[n] + \int n(\mathbf{r})V_{ext}(\mathbf{r})d\mathbf{r} \tag{2.19}$$

$$F_{HK}[n] = T_e[n] + E_{int}[n] \tag{2.20}$$

where F_{HK} is the Hohenberg-Kohn universal functional which contains the functional for the kinetic energy and that for the electron-electron interaction. This functional is completely independent of the system. The explicit form of both these functionals is unknown. Finding good approximations is one of the major challenges of DFT calculations.

The second HK theorem states that the exact ground state energy of the system is the global minimum of the universal functional F_{HK}. This theorem is nothing but the variational principle

$$E_0 \leq E_{HK}[n] = F_{HK}[n] + \int n(\mathbf{r})V_{ext}(\mathbf{r})d\mathbf{r} \tag{2.21}$$

which indicates that, the density that minimizes the HK functional is also the exact ground state density. Note that densities correspond to the ground

state densities of Hamiltonians with certain external potentials V_{ext}. These densities are called "V-representable" densities.

2.8 The Kohn-Sham equations

In 1965, W. Kohn and L. J. Sham used the formalism of the HK theorems to carry this approach further [30]. They considered a system of non-interacting electrons with an effective potential V_{KS}, instead of the original system of interacting electrons with a particular external potential V_{ext}, such that the ground state density of both systems are the same. In other words, the interacting many-body system is mapped on a system that is non-interacting, but with the same density and energy. Therefore, the Kohn-Sham (KS) method is exact since it yields the same ground state density as the real system, and provides an explicit algorithm to calculate the ground state energy and density.

It is mentioned before that the ground state energy of a system can be written as

$$E_0 = \min_{\Psi \longrightarrow n} \left(F_{KS}[n] + \int n(\mathbf{r}) V_{ext}(\mathbf{r}) d\mathbf{r} \right) \tag{2.22}$$

where the universal functional $F_{KS}[n]$ contains the contributions of the kinetic energy and the Coulomb interaction, and the minimization over all wave functions is performed leading to a certain density. This functional is defined for all densities that can be derived from wave functions with N electrons. Therefore these densities are called "N-representable" formulated by Levy and Lieb [31, 32]. The summation over the density throughout the solid is constant and equal to the number of electrons

$$N = \int_V n(\mathbf{r}) d\mathbf{r} \tag{2.23}$$

Now the KS method suggests to calculate the exact kinetic energy of a non-interacting reference system with the same density as the real, interacting one

$$T_{KS} = -\frac{1}{2} \sum_i^N \langle \Phi_i | \nabla^2 | \Phi_i \rangle \tag{2.24}$$

$$n_{KS}(\mathbf{r}) = \sum_i^N |\Phi_i(r)|^2 = n(\mathbf{r}) \tag{2.25}$$

where Φ_i are the orbitals of the non-interacting system. Therefore, Kohn and Sham introduced the following separation of the functional $F_{KS}[n]$

$$F_{KS}[n] = T_{KS}[n] + E_H[n] + E_{XC}[n] \tag{2.26}$$

where $F_{KS}[n]$ contains the contributions of the KS kinetic energy, the classical Coulomb interaction (Hartree energy) and the so-called exchange-correlation energy. By comparing this functional with the HK functional in equation (2.20), the exchange-correlation energy is derived as follows

$$E_{XC}[n] = (T_e[n] - T_{KS}[n]) + (E_{int}[n] - E_H[n]) \tag{2.27}$$

So E_{XC} is the functional that contains all the many-body effects that are not present in the classical kinetic energy, and Hartree interaction terms, in other words, E_{XC} contains everything that is unknown about the system.

Finally, the resulting Schrödinger-like equations called the Kohn-Sham equations are given by

$$[-\frac{1}{2}\nabla^2 + V_{KS}(\mathbf{r})]\Phi_i(\mathbf{r}) = \epsilon_i\Phi_i(\mathbf{r}) \tag{2.28}$$

where V_{KS} is the effective KS potential in which the electrons move, and is given by

$$V_{KS}(\mathbf{r}) = V_{ext} + V_H + V_{XC} = -\sum_I \frac{Z_I}{|\mathbf{r} - \mathbf{R}_I|} + \int \frac{n(\mathbf{r}')d\mathbf{r}'}{|\mathbf{r} - \mathbf{r}'|} + \frac{\delta E_{XC}[n(\mathbf{r})]}{\delta[n(\mathbf{r})]} \tag{2.29}$$

and

$$\left(-\frac{\nabla^2}{2} + V_{ext} + V_H + \frac{\delta E_{XC}[n(\mathbf{r})]}{\delta[n(\mathbf{r})]}\right)\Phi_i(\mathbf{r}) = \epsilon_i\Phi_i(\mathbf{r}) \tag{2.30}$$

The Kohn-Sham equations are solved self-consistently, since for the explicit i^{th} single particle orbital, the KS potential depends on all the other orbitals. First the initial electron density is guessed, for example, as a perturbation of atomic densities. Then the KS equations are solved, and the wave functions $\Phi_i(\mathbf{r})$ give the electron density through

$$n(\mathbf{r}) = \sum_{i=1}^{occupied} |\Phi_i(\mathbf{r})|^2 \tag{2.31}$$

The resulting density is compared to the initial guess. If the difference is larger than a predefined criterion, the new density enters the KS equations,

and the cycle is repeated until the iterations no longer modify the solutions and self-consistency is reached.

2.9 The exchange-correlation energy

While the KS method provides an exact expression for the total energy, unfortunately it is still not possible to solve the KS equations, since the XC functional is not known. In this section, some approximative expressions for this functional are briefly presented.

2.9.1 The local density approximation

The simplest approximation for the exchange-correlation energy is the Local Density Approximation (LDA). The basic idea of this approximation stems from a uniform electron gas. In this approximation it is assumed that the local XC energy per particle depends on the local density, and is equal to the XC energy per particle of a homogeneous electron gas (with the same density), in a neutralizing positive background. Thus the exchange-correlation energy E_{XC} is written in the following form

$$E_{XC}^{LDA}(n) = \int n(\mathbf{r})\epsilon_{XC}(n(\mathbf{r}))d\mathbf{r} \tag{2.32}$$

where $\epsilon_{XC}(n(\mathbf{r}))$ is the exchange-correlation energy per particle of a uniform electron gas of density $n(\mathbf{r})$. Therefore E_{XC} only depends upon the value of the electronic density at each point in space (local density). The quantity $\epsilon_{XC}(n(\mathbf{r}))$ can be further linearly decomposed into exchange and correlation contributions

$$\epsilon_{XC}(n(\mathbf{r})) = \epsilon_X(n(\mathbf{r})) + \epsilon_C(n(\mathbf{r})) \tag{2.33}$$

where the exchange part ϵ_X, represents the exchange energy of an electron in a uniform electron gas of a particular density and is given by [33, 34]

$$\epsilon_X = -\frac{3}{4}\left(\frac{3n(\mathbf{r})}{\pi}\right)^{1/3} \tag{2.34}$$

Since there is no explicit expression for the correlation part ϵ_C, several approaches have been proposed. For example, Ceperly and Alder in 1980 used accurate numerical quantum Monte-Carlo simulations of the homogeneous electron gas to find a numerical solution for ϵ_C [35] or Perdew and Wang who presented another accurate approximation for ϵ_C in 1992 [36].

The LDA is based on the local nature of the exchange-correlation potential and on the assumption that the density distribution does not vary too rapidly [30]. The accuracy of this simple approximation is surprisingly good and mostly leads to a correct picture of binding trends, structural parameters, bond lengths, vibrational energies, phonon spectra and other properties across the periodic table. However this method usually underestimates the band gap, and also overestimates the binding energy and underestimates the bond lengths [37]. This moderate accuracy that LDA delivers is insufficient for many applications.

2.9.2 The generalized gradient approximation

The generalized gradient approximation (GGAs) for the exchange-correlation energy improves in general upon the local density description (LDA) of atoms, molecules, and solids. It goes beyond LDA by using not only the information about the density at a particular point ($n(\mathbf{r})$), but also by using the density in the local neighborhood by including the dependence on the gradient ($\nabla n(\mathbf{r})$). Within this approximation, the non-homogeneity of the true electron density is taken into account. So the XC energy is written as follows

$$E_{XC}^{GGA}(n) = \int n(\mathbf{r})\epsilon_{XC}\left(n(\mathbf{r}), \nabla n(\mathbf{r})\right) d\mathbf{r} \tag{2.35}$$

In principle GGA method provides a better result for bond lengths, binding energies, ... than LDA, but in practice it has also some shortcomings.

Several studies have been made on comparing the advantages or disadvantages of the LDA versus GGA method (see Refs. [38], [39], [40]). For example, the lattice constants calculated using LDA are in general 2% smaller than the experimental ones, while GGA matches in most cases quite well or slightly overestimates the experimental values. This overestimation can lead to an underestimation of the bond strengths, in contrast to experiments and LDA.

There are many forms of GGA functionals that are used in different calculations. It is possible to construct a GGA, free of empirical parameters and starting from physical principles, e.g. the Perdew-Burke-Ernzerhof (PBE)-GGA form [38], while Becke exchange [41] and Lee-Yang-Parr (LYP) correlation [42] (BLYP) use parameters that are fitted to experimental data.

2.9.3 LDA and GGA for spin polarized systems

In order to deal with magnetic systems, the total electron density needs to be separated into the spin-up and spin-down components as

$$n(\mathbf{r}) = n_{\uparrow}(\mathbf{r}) + n_{\downarrow}(\mathbf{r}) \tag{2.36}$$

The magnetization density for a spin-polarized system is given by

$$m(\mathbf{r}) = n_{\uparrow}(\mathbf{r}) - n_{\downarrow}(\mathbf{r}) \tag{2.37}$$

Therefore the Kohn-Sham equations have to be extended so that any ground state property becomes a functional of both $n(\mathbf{r})$ and $m(\mathbf{r})$ as

$$E_{XC}^{LSDA}(n_{\uparrow}, n_{\downarrow}) = \int n(\mathbf{r})\epsilon_{XC}\left(n_{\uparrow}(\mathbf{r}), n_{\downarrow}(\mathbf{r})\right) d\mathbf{r} \tag{2.38}$$

and, the exchange-correlation energy for GGA can be written as

$$E_{XC}^{GGA}(n_{\uparrow}, n_{\downarrow}) = \int n(\mathbf{r})\epsilon_{XC}\left(n_{\uparrow}(\mathbf{r}), n_{\downarrow}(\mathbf{r}), \nabla n_{\uparrow}(\mathbf{r}), \nabla n_{\downarrow}(\mathbf{r})\right) d\mathbf{r} \tag{2.39}$$

2.9.4 The LDA+U method : beyond LDA/GGA

The LDA and GGA approaches work sufficiently well for a large number of systems. However it is often claimed that these methods are useless for strongly correlated materials, such as transition metals or rare-earth atoms, which have partially filled localized d or f bands [43, 44]. The LDA method tends to delocalize electrons over the crystal, and each electron feels an average of the Coulombic potential. In strongly correlated materials, there is a large Coulombic repulsion between localized electrons, which might not be well represented by a functional as the LDA approximation for E_{XC}. One of the simplest methods to avoid this problem is to add a Hubbard-like term for localized d or f orbitals, to the LDA density functional within the so-called "LDA+U" total energy functional [45, 46].

In this method, localized d (or f) orbitals are separated from delocalized orbitals (s and p electrons). A semi-empirical term is added to the conventional energy functional only for the localized orbitals which are expected to have strong correlation. The delocalized orbitals are correctly described by the usual LDA calculation.

Note that the double counting of interactions is avoided, by subtracting the double-counting correction term from the Hamiltonian. So the LDA+U total energy functional takes the form

$$E^{LDA+U} = E^{LDA} + (E^{U} - E^{dc}) \tag{2.40}$$

where the E^{U} is the electron-electron interaction energy of the localized electrons and E^{dc} is the double counting term which cancels the electron-electron

interaction energy, included in the E^{LDA} part. This technique is no longer parameter free and the Hamiltonian becomes orbital dependent. One important issue within this approach is the choice of the U parameter, which in principle can be calculated through first principles calculations (see Ref. [47, 48, 49]). In Table 2.1 the calculated values of U parameters for some systems are listed.

Table 2.1: Calculated U parameters for some systems (from Ref. [49]).

Material	U(eV)
ZnO	4.7
CdO	2.1
GaN	3.9
InN	1.9

2.10 The band gap problem

Most of the approximations for the exchange-correlation functional predict structural properties with sufficiently good accuracy. However for electronic properties such as the band gap, these approximations strongly underestimate the experimental value. For example this underestimation for LDA calculations is about 40% [30, 50].

The fundamental band gap can be defined as the difference between the ionization energy I and the electron affinity A [51]

$$E_{gap} = I - A \tag{2.41}$$

The ionization energy is defined as the energy required to remove an electron from the system, while the electron affinity is the energy released when an electron is added to the system. So the ionization energy and electron affinity for an N-electron system are defined as follows

$$I(N) = E(N-1) - E(N) \quad ; \quad A(N) = E(N) - E(N+1) \tag{2.42}$$

Since the XC functional is unknown, approximation methods should be used to solve the KS equations. It is good to know that the KS orbital energies ϵ_i have a meaning. J. F. Janak showed [52] that the variation of the total energy, with respect to an orbital occupation is equal to the eigenvalue of that orbital, independent of the detailed form of the exchange-correlation

functional. This leads to a connection between the ground-state energies of N and $N+1$-electron systems, which is useful in the calculation of certain excitation energies [52]. It is proven that

$$\partial E/\partial n_i = \epsilon_i \tag{2.43}$$

where n_i is the occupation number for each of the states and can be tuned between 0 and 1. Janak also connects the ground states of the N- and (N+1)-electron systems

$$E_{N+1} - E_N = \int_0^1 \epsilon_i(n) dn \tag{2.44}$$

So for the M-electron system, the first ionization potential and electron affinity can be written as

$$I(M) = -\int_0^1 dn \epsilon_M(M - 1 + n) \tag{2.45}$$

$$A(M) = -\int_0^1 dn \epsilon_{M+1}(M + n) \tag{2.46}$$

The addition or removal of one electron in an infinite crystal ($M \longrightarrow \infty$), can make an infinitesimal change in the ground-state density. This change comes from a corresponding infinitesimal change in the KS potential. Such a small change does not alter the one-electron energies. Therefore the fundamental band gap can be predicted by the KS band-structure of the neutral (M-electron) system [53, 54]

$$E_{gap}^{KS} = \epsilon_{M+1}(M) - \epsilon_M(M) \tag{2.47}$$

The missing parameter in this argument is the possibility that the KS potential (and specifically $\delta E_{XC}/\delta n(\mathbf{r})$) might be a discontinuous function [55]. So the XC potential might jump by a constant C when the number of electrons increases

$$\lim_{\eta \to 0} \left[\frac{\delta E_{XC}}{\delta n(\mathbf{r})}|_{M+\eta} - \frac{\delta E_{XC}}{\delta n(\mathbf{r})}|_{M-\eta} \right] = C \tag{2.48}$$

So the band gap energy becomes

$$E_{gap} = \epsilon_{M+1}(M) - \epsilon_M(M) + C \tag{2.49}$$

which implies that the KS band gap is underestimated by an amount equal to the derivative discontinuity C from the experimental one. Therefore the calculated band gap based on LDA or GGA is an underestimated approximation.

2.11 The hybrid functional: an accurate band gap

One possibility which has been very successful in calculating the band gap of different materials, is to use a hybrid exchange-correlation energy functional. It is defined as

$$E_{XC}^{hyb} = \alpha E_X^{HF} + (1-\alpha)E_X^{GGA} + E_C^{GGA} \tag{2.50}$$

where E_X^{HF} is the exchange energy calculated with the exact nonlocal HF wave function; E_X^{GGA} and E_C^{GGA} are the conventional semilocal GGA exchange and correlation energies, and α is a mixing parameter.

There are several hybrid functionals that can be used in different calculations. B3PW91 was the first one introduced in 1993 [56], later in 1994 and 1999 the popular B3LYP and PBE0 functionals appeared respectively [57, 58, 59]. In 2003 the screened hybrid HSE06 (Heyd-Scuseria-Ernzerhof) was proposed, which usually yields better results for the band gaps compared to other methods [60]. The mixing parameter of HSE06 is 25% and the functional is as follows

$$E_{XC}^{HSE06} = \frac{1}{4}E_X^{HF,SR}(\omega) + \frac{3}{4}E_X^{PBE,SR}(\omega) + E_X^{PBE,LR}(\omega) + E_C^{PBE} \tag{2.51}$$

PBE (Perdew-Burke-Ernzerhof) is a version of a GGA methods [38]. The exchange part is divided into short-range (SR) and long-range (LR) components. To avoid heavy calculations for long-range HF exchange, only the short-range part is mixed with the PBE exchange term. ω is the screening parameter, which indicates the range separation and is related to a distance for which the short-range interactions become negligible. So when ($\omega \longrightarrow \infty$), all of the interactions in the exchange energy are treated as long-range, and when ($\omega \longrightarrow 0$), all of them are treated as short-range. It has been shown that the optimum ω is approximately 0.2-0.3 Å [60]. The proposed 25% as the mixing parameter is not a generic feature for all systems and needs to be adjusted to obtain the correct band gap.

The HSE method leads to substantially improved band gaps compared to the other mentioned methods. Table 2.2 and Fig. 2.1 show the results obtained with the LDA and HSE potentials for the fundamental band gap of 23 solids [61].

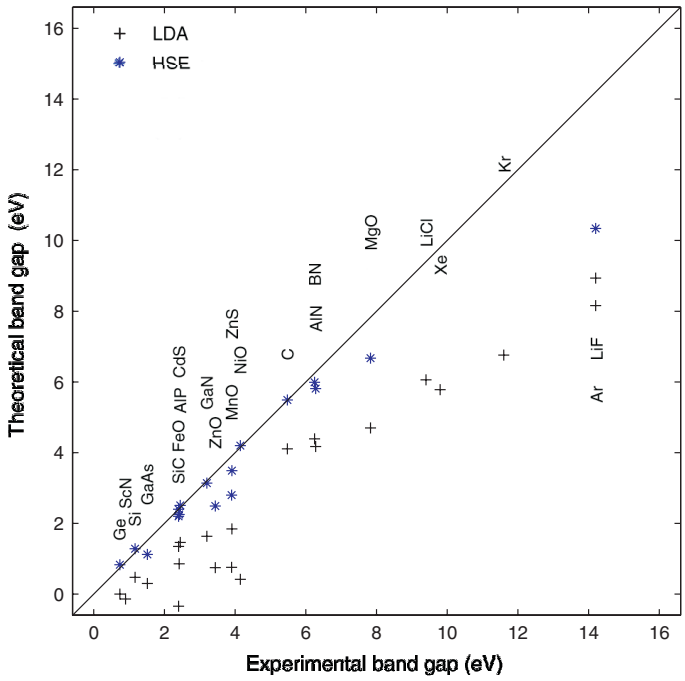

Figure 2.1: Theoretical versus experimental band gaps. The values are given in Table 2.2[61].

2.12 Periodicity of the crystal

In order to apply DFT to a real crystal, the KS equations should be solved for all the particles present in the system. Since there are too many particles in a real solid (roughly 10^{24} electrons and ions per cm^3), this will be computationally impossible. Therefore one should look for other possible approximations to solve the problem.

Crystal structures are built up from a unit cell which is periodically repeated. To reduce the number of particles in a calculation, it is enough to consider only the unit cell of the crystal. It consists of atoms, whose arrangement defines the crystal's symmetry, and its repetition in three dimensions in space generates a crystal structure. The unit cell is characterized by lattice parameters. To predict the property of a crystal it is enough to solve the KS equation for a small unit cell of a real solid.

2.12.1 The Bloch theorem

Consider the Hamiltonian for a single particle in a potential $U(\mathbf{r})$

Table 2.2: Theoretical and experimental fundamental band gaps (in eV). The structures are indicated in parentheses. Band gaps are measured either at room temperature (RT, 300 K) or at low temperature (LT), with LT implying less than 77 K. [61, 62].

Solid	LDA	HSE	Exp.
Ne (A1)	11.42	-	21.70 (LT)
Ar (A1)	8.16	10.34	14.20 (LT)
Kr (A1)	6.76	-	11.6 (LT)
Xe (A1)	5.78	-	9.8 (LT)
C (A4)	4.11	5.49	5.48 (RT)
Si (A4)	0.47	1.28	1.17 (LT)
Ge (A4)	0.00	0.83	0.74 (LT)
LiF (B1)	8.94	-	14.20 (RT)
LiCl (B1)	6.06	-	9.4 (LT)
MgO (B1)	4.70	6.67	7.83 (LT)
ScN (B1)	-0.14	-	0.9 (RT)
MnO (B1)	0.76	2.8	3.9 (RT)
FeO (B1)	-0.35	2.2	2.4 (LT)
NiO (B1)	0.42	4.2	4.3 (RT)
SiC (B3)	1.35	2.40	2.40 (LT)
BN (B3)	4.39	5.99	6.36 (LT)
GaN (B3)	1.63	3.14	3.20 (RT)
GaAs (B3)	0.30	1.12	1.52 (LT)
AlP (B3)	1.46	2.51	2.45 (RT)
ZnS (B3)	1.84	3.49	3.80 (LT)
CdS (B3)	0.86	2.25	2.42 (RT)
AlN (B4)	4.17	5.81	6.19 (LT)
ZnO (B4)	0.75	2.49	3.44 (LT)

$$H = \frac{-\nabla^2}{2} + U(\mathbf{r}) \tag{2.52}$$

According to the Bloch theory, the electrons move in a periodic potential $U(\mathbf{r})$ instead of moving in free space. This potential is generated by the periodic structure of the solid and is translational invariant.

$$U(\mathbf{r} + \mathbf{R}) = U(\mathbf{r}) \tag{2.53}$$

for all lattice vectors $\mathbf{R}$ of the crystal. Bloch's theorem states that the eigenstates Φ of this Hamiltonian can be written as

$$\Phi_{n\mathbf{k}}(\mathbf{r}) = e^{i\mathbf{k}.\mathbf{r}} u_{n\mathbf{k}}(\mathbf{r}) \tag{2.54}$$

where it has the form of a plane wave times a function u_{nk} with periodicity of the lattice. $\mathbf{k}$ is the wave vector that is chosen in the first Brillouin zone due to the translational symmetry, n is the band index which labels different solutions for a given $\mathbf{k}$, and $u_{n\mathbf{k}}(\mathbf{r}+\mathbf{R}) = u_{n\mathbf{k}}(\mathbf{r})$ for all $\mathbf{R}$ in the crystal.

Bloch's theorem is also written in another equivalent form

$$\Phi_{n\mathbf{k}}(\mathbf{r}+\mathbf{R}) = e^{i\mathbf{k}.\mathbf{R}} \Phi_{n\mathbf{k}}(\mathbf{r}) \tag{2.55}$$

If $E_n(\mathbf{K})$ is an energy eigenvalue, then $E_n(\mathbf{k}+\mathbf{G})$ is also an eigenvalue for all vectors G of the reciprocal lattice.

According to Bloch's theorem the problem of infinitely many-electrons has been turned into a problem of infinitely many k-points inside the first Brillouin zone. Since the wavefunctions of closely located k-points are almost identical, a small region can be sampled by one single k-point. In general it is enough to solve the KS equation, using only a finite number of k-points, in a unit cell of the crystal and calculate the electronic part of the total energy, to a good approximation. So choosing a sufficiently dense mesh of integration points is crucial for the convergence of the results. There are several methods for sampling the Brillouin zone with an appropriate set of k-points, such as the scheme proposed by Monkhorst and Pack in 1976. [63]

2.12.2 Energy cut-off

The periodic functions $u_{n\mathbf{k}}$ can be expanded in plane waves

$$u_{n\mathbf{k}}(\mathbf{r}) = \sum_{\mathbf{G}} c_{n\mathbf{k},\mathbf{G}} e^{i\mathbf{G}.\mathbf{r}} \tag{2.56}$$

where the summation is over all reciprocal lattice vectors $\mathbf{G}$. So the KS wave functions at each k-point are now expressed in terms of an infinite discrete plane wave basis set

$$\Phi_{n\mathbf{k}}(\mathbf{r}) = \sum_{\mathbf{G}} c_{n\mathbf{k},\mathbf{G}} e^{i(\mathbf{k}+\mathbf{G}).\mathbf{r}} \tag{2.57}$$

Since it is not possible to consider an infinite basis set, the number of plane waves can be restricted by placing an upper boundary to the kinetic energy $(\mathbf{k}+\mathbf{G})^2/2$ of the plane waves. This boundary is called the energy cut-off E_{cut} and the restriction is thus given by

$$\frac{|\mathbf{k}+\mathbf{G}|^2}{2} < E_{cut} \tag{2.58}$$

2.13 Pseudopotentials

Although the initial many-body problem has been considerably simplified, it is still computationally expensive for a system with a large number of electrons. Pseudopotentials (PPs) or effective potentials are used as an approximation for the simplified description of complex systems. There are several methods to generate different pseudopotentials. On the other hand, there are also some other approaches called all-electron methods in which all the electrons are explicitly used in the computation. The fact that PPs are not unique allows the freedom to choose forms that simplify the calculations and the interpretation of the resulting electronic structure. Some of these methods are introduced briefly in the following section.

2.13.1 Plane wave pseudopotential method

The plane wave pseudopotential (PP) approach is used to replace the atomic all-electron potential such that the core states are eliminated. It is based on the fact that most physical properties of solids only depend on the valence electrons and one can distinguish between the core and valence electrons.

In this approximation, the core (i.e. non-valence) electrons are removed and the strong ionic potential is replaced by the weaker pseudopotential V_{pseudo} in the Schrödinger equation, that acts on a set of pseudo wave functions Ψ_{pseudo}. This approach was first introduced by Hans Hellmann in 1934 [64]. These pseudo functions are constructed in such a way that the pseudo wave function and the true wave function become identical beyond a certain radius (cut-off radius r_c). As it is shown schematically in Fig. 2.2, the pseudo wave function is generated so that it has no radial nodes in the core region.

2.13.2 Projected augmented wave method

The projector augmented wave method (PAW) is an alternative which has been introduced by Blöchl in 1994 [65]. This approach is in between the all-electron and pseudopotential method.

The PAW approach transforms the rapid oscillating wave functions of the valence electrons near ion cores into smooth wave functions which are computationally more convenient. The true wave functions Ψ_n are related to the pseudo wave functions $\tilde{\Psi}_n$ by a linear transformation [65]

$$|\Psi_n\rangle = |\tilde{\Psi}_n\rangle + \sum_i (|\Phi_i\rangle - |\tilde{\Phi}_i\rangle) c_i \tag{2.59}$$

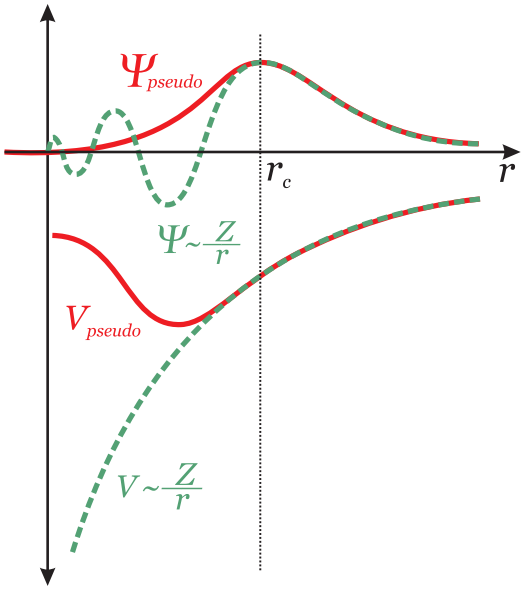

Figure 2.2: Schematic representation of the pseudo potential and the pseudo wave function. The dotted vertical line corresponds to the cut-off radius r_c.

where n is the band index, i is an atom index, and c_i are coefficients. Since we require the transformation to be linear, these coefficients must be linear functionals of the pseudo wave functions.

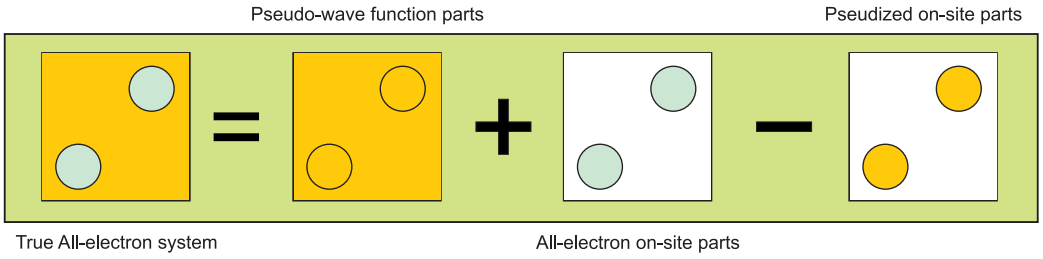

Figure 2.3: Schematic representation of the basic concept of the PAW method.

So the true all-electron wave function is expressed in three terms. The first term is the pseudo wave function $\tilde{\Psi}_n$ which is identical to the true state outside the augmentation region. The second term is the all-electron core partial wave Φ_i which is identical to the all-electron core state Ψ_n, and finally the pseudo core partial wave $\tilde{\Phi}_i$ which is identical to the pseudo core states $\tilde{\Psi}_n$. Figure 2.3 schematically shows the basic concept of the PAW method.

In this thesis we make use of density functional theory to calculate the electronic properties of some TCO materials within the LDA, LDA+U, and HSE06 approach as implemented in the Vienna ab initio simulation package [66]. Electron-ion interactions are treated using the projector augmented wave potentials [67, 68, 65].

Chapter 3

Electronic Properties of Defects and Impurities in Solids

3.1 Introduction

The study of point defects and impurities is an important area in semiconductor, insulator, and metal physics [9, 69, 70, 71]. Defects have profound effects on materials properties, and can be used to control their electronic and optoelectronic properties. Although they can improve some properties and turn materials into useful device components, they can also have some undesirable effects. These changes in the properties occur already for small amounts of defects, and the term dopant is usually used for an impurity atom at low concentration, which is in the order of one per million host atoms. So the desired properties can be achieved without changes in composition of the material, but just by manipulating the crystal defects.

To achieve such control on the mechanism of defects in different solids, knowledge of the fundamental processes that control doping is necessary. First-principles calculations have already made important contributions to the understanding of these fundamental processes of doping in different semiconductors [9].

In the following chapter, different kinds of defects are classified and some related terms such as donor, acceptor, shallow, and deep are introduced. Then some important parameters which can be calculated theoretically such as their formation energies, and transition levels are briefly explained. Finally different approaches are presented in order to improve the DFT results and make them more consistent and comparable to experimental data. This knowledge is later used in the next chapters to study the electronic properties of defects and impurities in some TCO materials.

3.2 Defects with different spatial extents

Any deviation from the perfect atomic arrangement in a crystal is called a defect. Defects can be categorized by their spatial extent. They are classified into four categories according to their dimension:

- **Point defects** (zero dimensional)
  localized imperfections in crystals which occur only at or around a single lattice site.

- **Line defects** (one dimensional)
  involve rows of atoms which are misaligned, such as dislocations.

- **Planar defects** (two dimensional)
  occur over a surface in the crystal. This involves interfaces between two crystal regions of different crystallographic orientations or different phases. Also it can happen in face-centered cubic or hexagonal close-packed crystals when there is a change in the regular sequence of positions of atomic planes (stacking faults).

- **Extended defects** (three dimensional)
  composed of some defects, which are clustered together in a small region of a crystal.

This chapter discusses different types and properties of point defects. Point defects can be further divided into the following:

◇ **Vacancies**
Vacancies are lattice sites which are vacant by missing atoms. In other words, a vacancy is the absence of an atom from its normal location in a perfect crystal structure. (A missing atom A in a crystal is denoted by V_A).

◇ **Schottky defects**
A Schottky defect occurs when an equal number of cations and anions are missing from their lattice sites, and the electrical neutrality of the crystal is maintained. This type of defect appears generally in ionic crystals, where the positive and negative ions do not differ too much in size. The Schottky defect is a type of vacancy named after Walter H. Schottky. [72] (This defect in an ionic crystal A^+B^- is denoted by $V_A + V_B$).

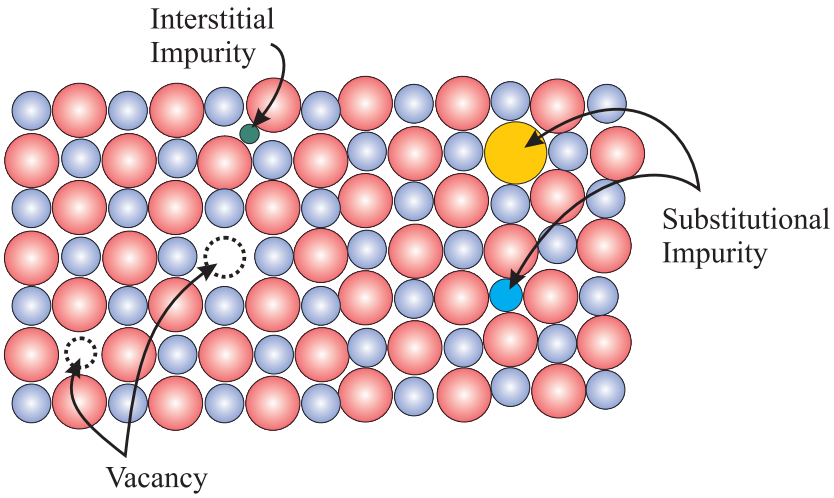

Figure 3.1: Schematic illustration of some types of point defects in a crystal.

◇ **Interstitials**

Interstitial defects are formed when an extra atom is occupying a site in the crystal structure at which there is usually not an atom. (Inserting atom A in an interstitial site in the crystal is denoted by A_I.)

◇ **Frenkel defects**

An atom displaced from its position to a nearby interstitial site is called a Frenkel defect, named after Yakov Frenkel. [73] (Since it is having V_A and A_I defects together, it is labeled as $V_A + A_I$.)

◇ **Substitutionals**

Substitutional defects are formed when an extra atom replaces a host atom. (Atom A replacing a host atom B in the crystal is denoted by A_B.)

◇ **Antisites**

Antisite defects are a kind of substitutional defects in which a host atom occupies the site which was originally occupied by another type of host atom. (A host atom A replacing another host atom B in the crystal is labeled as A_B.)

Figure 3.1, schematically shows different types of defects in a crystal. Vacancies, Schottky, Frenkel, and antisite defects which do not involve foreign atoms are also called native or 'intrinsic' defects, and other defects such as interstitials and substitutionals involving foreign impurity atoms are called 'extrinsic' defects.

3.3 Electronic properties of defects

Defects have a strong influence on the electronic properties of the host material. One can classify defects in different systems, by their level depth which is created in the band gap of the host material, into shallow and deep levels. In the following the important concepts of donors and acceptors, and deep and shallow levels are discussed. Some experimental methods to study these states are also briefly introduced (for more details see Ref. [69, 74]).

3.3.1 Shallow dopants

An intrinsic semiconductor has no free electrons in its conduction band (at $T = 0K$). One can make semiconductors conducting by adding very small amounts of selected impurities or native defects to the semiconductor. ($\sim$ one per million host atoms). The process of adding specific amounts of impurities to a material is called doping. The doping process in a semiconductor can be characterized as one of the followings

- **N-type doping**: Adding an impurity or defect in a semiconductor increases the number of free electrons, the doped semiconductor is n-type (or negative type) and the defect that causes this effect is referred to as a donor since it donates its electron for conduction. This addition of free electrons, enormously increases the conductivity of the semiconductor. A 1 cm^3 sample of pure germanium at room temperature contains about 10^{13} intrinsic free carriers (electrons or holes). If the Ge sample doped with 10^{17} phosphorous atoms per cm^3, the dopant donates an extra 10^{17} free electrons in the same volume and the electrical conductivity is increased by a factor of 10000. For example according to the periodic table of elements, a group-V atom such as phosphorus P has one extra valence electron compared to a group-IV atom such as Si. Then, by substituting one Si atom in the semiconductor material silicon with one P atom the system becomes an n-type semiconductor. This is because the P atom has 5 valence electrons in its outer shell and uses 4 of them to form covalent bonds with the Si atoms, leaving 1 electron almost free in the crystal. This extra electron of dopant atom P is loosely bound and can be easily excited into the conduction band. So atom P acts as a donor in Si.

  In this situation, the dopant atom creates an energy level just below the bulk material's conduction band. Since the dopant level is very close to the bulk conduction band, it only requires a small amount of energy to free the electrons in order to move freely in the conduction band.

Figure 3.2 schematically shows the silicon crystal structure doped n-type.

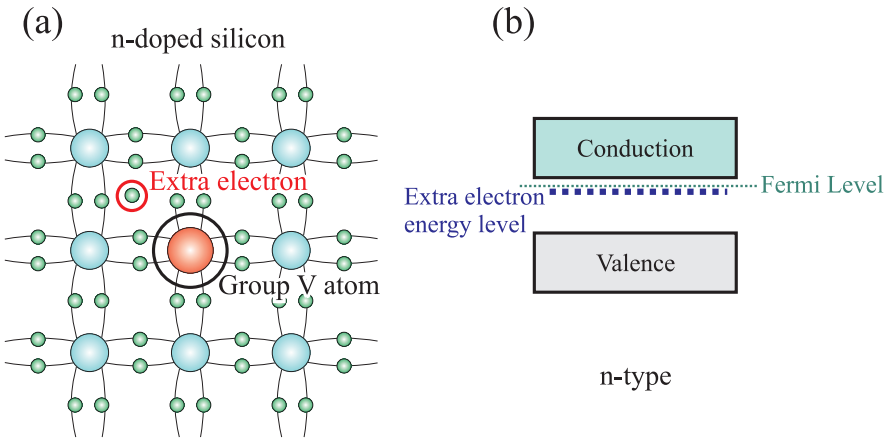

Figure 3.2: Schematics of silicon crystal structure (a) doped with an impurity to produce n-type semiconductor material, (b) valence and conduction bands with respect to a defect level.

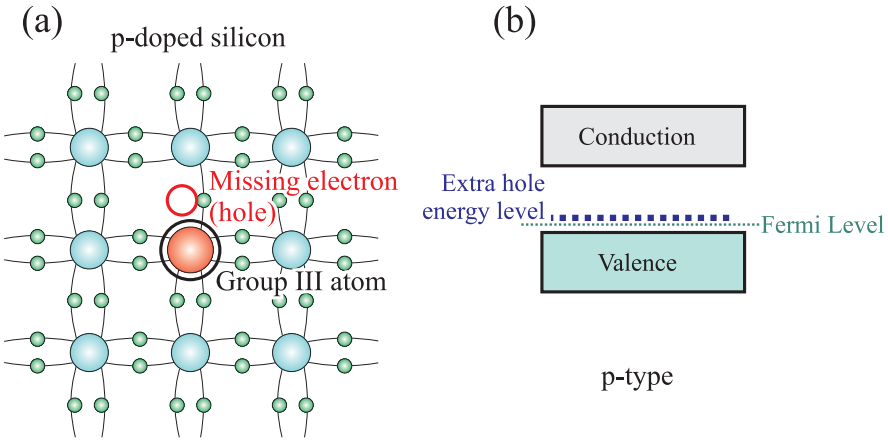

Figure 3.3: Schematics of silicon crystal structure (a) doped with an impurity to produce p-type semiconductor material, (b) valence and conduction bands with respect to a defect level.

- **P-type doping**: An impurity or defect that reduces the number of free electrons in a semiconductor (causing more holes), is p-type (or positive type) and the defect that causes this effect is referred to as an

acceptor. For example substituting a Si atom in bulk Si with a group-III atom such as aluminium Al (with one less valence electron), causes the system to be p-type. In this case, the impurity has one electron less than the required amount to establish a covalent bond, therefore in a single covalent bond there will be only 1 electron instead of 2, and the Al atom acts as an acceptor in this system.

In this situation, the dopant atom creates an empty energy level just above the valence band of the bulk material. So electrons in the valence band find it easy to hop into these new levels and creating holes in the valence band. Figure 3.3 schematically shows the silicon crystal structure doped p-type.

As it is mentioned above, n-type and p-type doping create energy levels just below the conduction band and above the valence band of the bulk material, respectively. Since these defect levels are very close to the bulk valence or conduction band edges, they can be ionized easily. These types of levels are called shallow states, and a dopant causes a shallow state is referred to as a shallow dopant. On the contrary, any other impurities that are not shallow are referred to as deep dopants and are discussed in the next section.

Most[1] shallow dopants can be described by a hydrogen-like model in the effective mass approximation. Let's consider a perfect semiconductor with completely full valence bands and empty conduction bands. Now substitute one of this semiconductor's atoms by an impurity atom from the next column of the periodic table. The impurity atom has one more valence electron, while its nucleus has one extra positive charge. This positively charged ion causes an extra Coulomb field

$$V(\mathbf{r}) = \frac{e}{\epsilon \mathbf{r}} \tag{3.1}$$

where ϵ is the dielectric constant of the material (since the positive ion is in a dielectric medium). Therefore an extra valence electron can be considered as a free electron with mass m^* moving in the impurity potential $V(\mathbf{r})$ in addition to the crystal potential. The Schrödinger equation of the donor electron has the form

$$(-\frac{\hbar^2}{2m^*}\nabla^2 + V(\mathbf{r}))\Psi(\mathbf{r}) = E\Psi(\mathbf{r}) \tag{3.2}$$

[1]Also localized levels in the band gap can be considered shallow, if they are located close to the CBM or VBM. However, in this section we only consider shallow defects with an extended wavefunction.

This situation is similar to the hydrogen atom with one electron and one proton. The difference is that now the proton has a charge e/ϵ instead of e and the electron has a mass m_e^* instead of m_e. This approach is known as the effective mass approximation. It is known that the hydrogen atom has bound states with energies of

$$E_n^{(H)} = -\frac{e^4 m_e}{2\hbar^2 n^2} \tag{3.3}$$

where $n = 1, 2, 3, ...$ The ground state has energy $E_1 = -13.6eV$, and the second energy level has energy $E_2 = -13.6/4 = -3.4eV$ (the first excited state). The ionization energy for an extra electron (from an impurity atom) in the host system can be written as

$$E_n^{donor} = E_{CBM} - \frac{e^4 m_e^*}{2\hbar^2 n^2 \epsilon^2} = E_{CBM} - E_n^{(H)} \frac{m_e^*}{\epsilon^2} \tag{3.4}$$

where E_{CBM} is the energy at the conduction band minimum (CBM) and m_e^* is in units of m_e. Considering ϵ has a typical value in the order of 10, and the effective mass usually varies between $0.1m_e$ to about m_e, the above equation then indicates that the ionization energy of the donor energy level ($n = 1$) ranges from ~ 13 to ~ 130 meV. This small energy compared to the band gap, of the order of 1 eV, clearly confirms that such hydrogenic levels are shallow. Table 3.1 shows the experimental ionization energies of some donor states in silicon.

Table 3.1: Experimental ionization energies of some donor states when added to Si.

Donor	Ionization energy (eV) [75]
P	0.044
As	0.049
Sb	0.039
Li	0.033

It is important to realize that these shallow levels are not atomic impurity levels. A representation of some of the bound states of a donor atom near a parabolic conduction band is shown in Fig. 3.4. This figure also indicates the atomic impurity level in resonance with the conduction band. After relaxation of the electron to the minimum of the conduction band, this atomic level is unoccupied. The electron becomes now weakly bound to the impurity ion which is the effective mass state discussed above. The extension of the wave function becomes of the order of the effective Bohr radius and is spread out over many lattice constants.

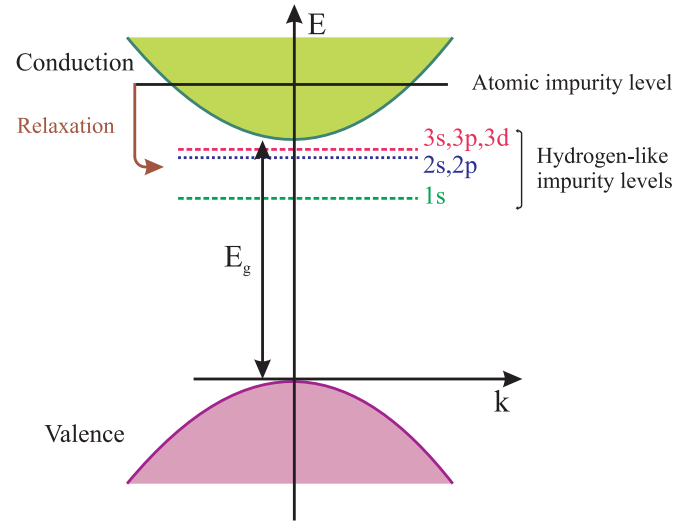

Figure 3.4: Schematic representation of the n=1,2, and 3 bound states of a shallow donor electron.

The above statements also apply to acceptors. In acceptors, the impurity atom has one or more electrons less than the host atom. If E_{VBM} is the energy at the valence band maximum (VBM), and m_h^* is the effective mass of the hole, then shallow hydrogenic energy levels are created above the E_{VBM} with ionization energies

$$E_n^{acceptor} = E_{VBM} + \frac{e^4 m_h^*}{2\hbar^2 n^2 \epsilon^2} = E_{VBM} + E_n^{(H)} \frac{m_h^*}{\epsilon^2} \tag{3.5}$$

where m_h^* is in units of m_e.

Finally it should be noted that the most important role of shallow dopants is to control conductivity. Almost all of these impurities are ionized and contribute to the conductivity at room temperature (because their ionization energies are comparable to $k_B T \sim 25meV$).

3.3.2 Deep dopants

Defects do not always create shallow levels, but also deep levels can form when the atomic impurity levels are not in resonance with the valence or conduction band and fall into the band gap[2]. Unlike shallow states, deep states have strongly localized wave functions. Deep states are often undesired, since they can cause carrier trapping and recombination. Their main

[2]Deep levels can be called shallow if they are located close to the CBM (for donors) or VBM (for acceptors).

function is to act as a catalyst for recombination of electrons and holes. The presence of such dopants provides intermediate levels within the band gap. These intermediate levels act as smaller energy steps for electrons (in the conduction band) and holes (in the valence band) making electron-hole recombination more likely. Therefore the most important role of deep dopants is to control the lifetime of carriers. A schematic illustration of the particle energy states for a shallow and deep acceptor levels is shown in Fig. 3.5.

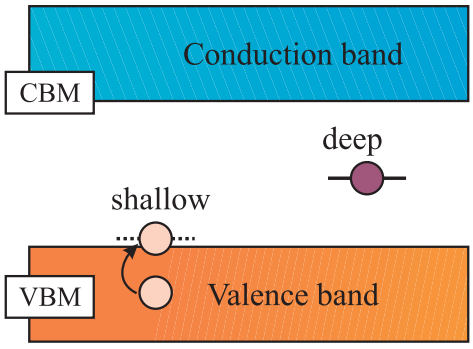

Figure 3.5: Schematic illustration of the particle energy states for a shallow and deep acceptor levels.

3.3.3 Limitations of the ab initio approach

Although shallow levels are either very close to the conduction band minimum or to the valence band maximum, in practical computations, these extended states cannot be successfully described within the usual volume of supercells in DFT calculations.

A tight-binding (TB) calculation for silicon bulk doped with shallow donor phosphorus showed that a very large supercell (64000 Si atoms) is required before the binding energy of the system is converged and before the extension of the impurity wave function fits in the supercell. This corresponds to a distance of more than 100Å between the dopants [76]. Ionization energies of shallow impurities can therefore not be determined from DFT calculations. So in the calculations, shallow donors usually fall in the conduction band, while shallow acceptors fall in the valence band. Note that although ionization energies of shallow levels cannot be determined, the character of a shallow state can. On the other hand, the position of deep levels can be determined by DFT calculations.

3.3.4 Experimental techniques

The nature of an impurity of being either shallow or deep, and the position of the energy levels can also be determined experimentally. The position of an impurity level can be achieved by identifying transitions of electrons from one level to another in experiment. Transitions can be related to excitations (electron goes to higher energy level by absorbing energy), or to de-excitations (electron goes to lower energy level by releasing energy).

According to the form of the absorbed or released energy, experimental methods to determine these transitions can be classified into two groups:

- **Thermal experiments:** At $T = 0K$, all electrons occupy their ground state energy levels and since there is no external perturbation, transitions between different levels are not possible. At finite temperature the situation is different. There will be thermal vibrations of the crystal lattice and these vibrations may interact with electrons in a crystal. In the case of donors, the electrons which are activated may make transitions from their levels in the band gap to the conduction bands (electron emission), while some other may drop back into the empty levels in the gap (electron capture). For acceptors, the electrons may make transitions from the valence bands into the level in the band gap (hole emission) and vice versa (hole capture). Finally at a certain temperature, a steady state occurs and the density of excess carriers $n(T)$ is measured. The density of carriers can be obtained indirectly by measuring either the conductivity or the Hall coefficient in a crystal [77]. These methods are mostly used for detecting shallow states.

  On the other hand, in order to detect a deep state the concentration of shallow dopants should be lower than the concentrations of deep dopants. Therefore some techniques are developed to achieve the desired concentration, such as junction techniques. These techniques study deep level impurities located in the transition region of a p-n junction where the Fermi level lies in the middle of the gap, and the shallow dopants are all ionized. Figure 3.6, shows a schematic representation of a p-n junction.

  For such a system applying a reverse bias, sweeps away the charge carriers and so increases the resistivity of the p-n junction. This results in the p-n junction to behave as an insulator. Electrons of the deep levels can be thermally excited to the conduction bands, and the change in the capacitance of the p-n junction can be measured [78, 79, 80, 81]. Such techniques have been referred to as deep level transient spectroscopy (DLTS).

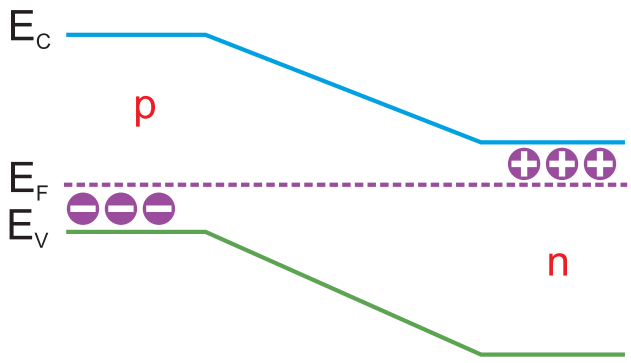

Figure 3.6: Schematic representation of a p-n junction. E_F is the Fermi level.

- **Optical experiments:** The difference between these experiments and thermal experiments comes from the difference between the form of the energy supplied or released in the process. Here transitions are caused by an external photon field, instead of the phonon field in thermal experiments. The fact that photons can be supplied with desired frequencies and intensities which are easily controllable, makes optical experiments more flexible than the thermal ones. In these types of experiments, carriers are excited from their ground states into the excited bands by absorbing light. For frequencies smaller than the separation between the level and the band edge, there should be no absorption. By scanning through other frequencies, peaks corresponding to impurity levels appear in the absorption spectrum of a crystal and they are measurable [82, 83, 84], for example using electron paramagnetic resonance (EPR) and electron spin resonance (ESR) spectroscopy [85, 86].

  The optical experiments work well for shallow levels, and sometimes they yield good results for deep levels as well, but in general for deep levels, junction techniques are usually more applicable.

In addition to the above mentioned techniques, three-dimensional (3D), atomic scale information on dopant atoms can also be obtained from aberration-corrected (scanning) transmission electron microscopes. In high angle annular dark-field scanning transmission electron microscopy (HAADF-STEM) a focused electron beam is scanned across the specimen and, at each point transmitted electrons scattered to high angles, are measured by an annular detector. The measured intensity depends on the atomic number Z. HAADF-STEM combined with advanced 3D reconstruction techniques allows for a 3D reconstruction of the material at the atomic scale [87, 88, 89]. Combining STEM with electron energy loss spectroscopy (EELS) provides

local chemical, structural, and electronic information such as nearest neighbors bonding, dielectric response, band gap and valence state [90].

3.4 Doping limitations

Doping of semiconductors has a number of limitations and difficulties, which need to be considered [9]. In this section, we itemize some of these limitations and requirements for successful doping.

- **Solubility:** The solubility corresponds to the highest concentration that the impurity can achieve in the semiconductor (in thermodynamic equilibrium). This concentration depends on temperature, the abundance of the impurity, and the host constituents in the growth condition.

  In order to have a high carrier concentration, a high concentration of the dopants is needed. Note that increasing the number of the dopants, does not necessarily increase their concentration in the solid, since forming a different phase may turn out to be more favorable.

- **Ionization energy:** The ionization energy of a dopant is directly related to its doping efficiency, since this energy determines the fraction of dopants that contributes to the formation of free carriers (at a given temperature). Ionization energy is mostly related to the inherent properties of the semiconductor, and the higher the ionization energy, the more limited the doping.

- **Compensation of the dopants:** To control the doping process, it is necessary to be aware of the compensation effect of the other impurities or native defects. For example, when a semiconductor is doped with an acceptor to obtain p-type conductivity, other impurities or native defects that act as donors should be carefully controlled and prohibited.

- **Incorporation of the dopants in other configurations:** A dopant may behave differently at different sites of the semiconductor. For example, Li on the Ga site in GaN acts as an acceptor, while Li on an interstitial site acts as a donor. Since the interstitial position is energetically more favorable, the Li dopant prefers to act as a donor rather than an acceptor in GaN, and this can clearly lead to self-compensation [91].

3.5 Methodology

First-principles calculations made large contributions to the understanding of the behavior of different defects and impurities in semiconductors. Within density functional theory, it is possible to calculate total energies and particularly the formation energies for several types of dopants in different materials. The structural behavior of a dopant, its stable position in the host material, and the relaxation of the surrounding atoms are some other important properties that can be investigated.

In the following section, it is briefly described how to use the total energy of a defect to calculate its concentration and the formation energy in a material, how to find the transition levels between different charge states of a defect which determines its shallow or deep character, and some other important issues related to the study of defects.

3.5.1 Concentrations of defects

Creation of defects and impurities in a crystal normally costs energy. One of the main quantities in the study of point defects is the Gibbs free energy. In thermodynamic equilibrium the concentration c of an impurity in a crystal is given by the expression[92, 9]

$$c = N \exp(-\Delta G/k_B T) \tag{3.6}$$

where N is the number of equivalent possibilities, with the same energies, in which the defect can be incorporated (per unit volume). ΔG is the change in the Gibbs free energy of the system, k_B is Boltzmann's constant, and T is the temperature.

The change in Gibbs free energy of the system is given by

$$\Delta G = \Delta E + P\Delta V - T\Delta S \tag{3.7}$$

where ΔE is the change in the total energy (contains chemical potential terms), P is the pressure, ΔV is the change in the volume when an impurity is introduced into the system, and ΔS is the change in vibrational entropy of the system. The change in the volume is negligible for most crystalline solids at moderate temperatures and atmospheric pressure. Moreover for different defects, the change in vibrational entropy is usually very small. Therefore the Gibbs free energy of the system is equal to the formation energy ($\Delta E \equiv E_f$) of the system. Hence Eq. (3.6) can be written as

$$c = N \exp(-E_f/k_B T) \tag{3.8}$$

According to this expression, defects with high formation energies will occur in low concentrations. Since the growth of a semiconductor is close enough to the equilibrium condition, it warrants the use of the expression (3.8). This brings up the prominence of the formation energy of defects in crystals. Though thermodynamics provides the driving force for the formation of the defects, it should be noted that the number of defects also depends on the thermal history of the host material i.e. on the kinetics of the growth process. In the following, the derivation of the formation energy is discussed.

3.5.2 Formation energy

Density functional theory calculations in the supercell geometry are used as a standard method to study defects and impurities in semiconductor materials. As discussed in chapter 2, using an appropriate exchange correlation energy functional provides a description of the many-body electronic ground state energy of a system.

Since the purpose of this thesis is to investigate the electronic properties of an isolated defect in an infinite crystal, performing calculations needs a large supercell containing a defect which provides a low concentration of defects in a crystal. The larger the supercell size, the smaller the interactions between defects and impurities in neighboring supercells, and the better the results will be compared to a single, isolated impurity. Moreover, relaxation of several layers of atoms around the impurity is also included inside the supercell.

Equation (3.8) shows that the concentration of point defects and impurities depends on their formation energies. The formation energy of a defect or impurity D in the charge state q is defined as

$$E_f[D^q] = E_{tot}[D^q] - E_{tot}[bulk] + \sum_i n_i \mu_i + q[E_F + E_v + \Delta V] \qquad (3.9)$$

$E_{tot}[D^q]$ is the total energy from a supercell calculation with one impurity D in the cell, and $E_{tot}[bulk]$ is the total energy for the equivalent perfect supercell. n_i indicates the number of atoms of type i that have been added ($n_i < 0$) or removed ($n_i > 0$) from the supercell when the defect or impurity is created, and μ_i are the corresponding chemical potentials which represent the energy of the reservoirs with which atoms are being exchanged. Chemical potentials for different species are discussed in more details in the following section. E_F is the chemical potential of the electron, which in semiconductor physics is often called the Fermi energy, with respect to E_v, which we choose to be the top of the valence band of the primitive defect-free unit cell. In the

defect containing supercell, the position of band edges (valence band maximum, conduction band minimum) is affected by the defect, which brings different reference energies for the defect containing and the perfect crystal. In order to assume that we use the same reference energy level for the calculations with and without the defect, another term (denoted as ΔV) should be added to the formation energy for charged defects. This is schematically shown in Fig. 3.7. A widely applied practice to determine ΔV is to consider the total electrostatic potential at some point, or region, far from the defect and to align it with the potential in the same region in the undoped supercell [9].

As an example, consider an oxygen vacancy as a native defect in an oxide material. The formation energy or the energy needed for an oxygen vacancy to form in a supercell is schematically shown in Fig. 3.8. According to the definition, the formation energy is the difference between the total energy of the oxide with an oxygen vacancy and the initial pure oxide. Since an oxygen atom is removed from the system and is moved into a "reservoir" of oxygen atoms (e.g. a gas of O_2 molecules), the total energy of an oxygen atom in the reservoir ($\mu_O = \frac{E[O_2]}{2}$) should be also added to the formation energy expression. If the system is electrically charged, then an extra term should be considered. Here the oxygen vacancy gives away one electron and has a positive charge state, so the energy of an electron in its reservoir (chemical potential of the electron) is added to the formation energy expression.

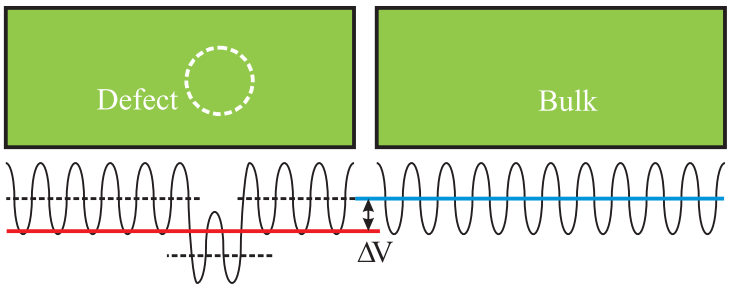

Figure 3.7: Schematic representation of the ΔV value.

As mentioned before, defects can occur in multiple charge states, and the formation energy is different for each of them. The stable charge state for an impurity at a given Fermi level is the one which has the lowest formation energy.

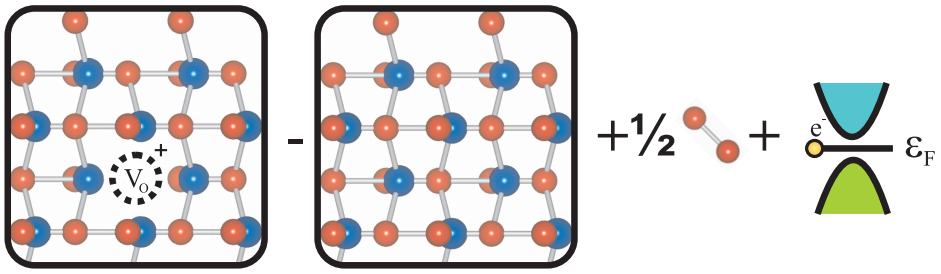

Figure 3.8: Schematic illustration of the formation energy of an oxygen vacancy in a crystal.

3.5.3 Thermodynamic transition levels

It is previously mentioned that defects and impurities introduce levels in the band gap of the semiconductor or near the band edges. These levels have an important influence on the electrical properties of a material, and these are the ones that are measured in the experiments. Therefore it is essential to identify the nature of the transition level (shallow or deep) and calculate their positions in the band structure [9, 93].

The (thermodynamic) transition levels between different charge states can be calculated by using their formation energies. The transition level $\epsilon(q, q\prime)$, is the Fermi energy for which the formation energies of charge states q and $q\prime$ are equal

$$E_f[D^q] = E_f[D^{q\prime}] \tag{3.10}$$

Considering Eq.(3.9), the thermodynamic transition level between two charge states q and $q\prime$ can be written as

$$\epsilon(q, q\prime) = \frac{E_f(D^q; E_F = 0) - E_f(D^{q\prime}; E_F = 0)}{q\prime - q} \tag{3.11}$$

In the above equation $E_f(D^q; E_F = 0)$ is the formation energy of the defect D in the charge state q when the Fermi level is at the valence band maximum ($E_F = 0$). Thus for Fermi levels below this transition point, charge state q is stable while for Fermi levels above, charge state $q\prime$ is stable.

As an example, Fig. 3.9 shows the calculated formation energies versus the Fermi energy for the oxygen vacancy (V_O) and zinc interstitial (Zn_i)

defects in the ZnO host material[3]. For the oxygen vacancy, different charge states $(0, 1+, 2+)$ are shown. It is clear that the + charge state (V_O^+) is never the stable configuration for the relevant range of Fermi energies. For the Fermi energies close to the VBM, this defect is stable in the 2+ charge state and for Fermi energies close to the CBM, the oxygen vacancy is stable in the 0 charge state. Because the transition $\epsilon(0, 2+)$ occurs in the band gap, it follows that the oxygen vacancy acts as a deep donor in ZnO. On the other hand, Fig. 3.9(b) shows that the zinc interstitial defect is only stable in the 2+ charge state. Since the transition $\epsilon(0, 2+)$ occurs in the conduction band, one can conclude that the zinc interstitial acts as a shallow donor in ZnO.

Note that in order to compare the calculated transition points with the thermal ionization energies from the experiments, for each charge state the atomic structure is also relaxed to its equilibrium configuration. This is the reason why the calculated transition levels are not necessarily equal to the transition levels obtained from the optical experiments. The excitation energy measured in optical experiments is different from the thermodynamic transition level, because the atoms don't have the time to relax to their ground state positions corresponding to the new situation. So in optical experiments, the optical transition level is observed where the final charge state (after the transition) is not relaxed to its equilibrium configuration. Thus in the systems where lattice relaxations of a defect strongly change from one charge state to another, the transition level will considerably differ from the optical transition level.

Figure 3.10 shows the configuration coordinates diagram illustrating the difference between optical and thermal transition energies. Consider an electron in the equilibrium configuration related to the charge state q_0 of the defect, denoted as q_0^0. This electron can absorb a photon and the defect makes a transition to another charge state q_+, while the surrounding ions do not move. The minimum energy required for such a vertical transition is called the optical energy, $E_{optical}$, and can be measured in an optical experiment. The excited electron ends up in the minimum of the conduction band far away from the defect, thus from the defect-free system. After the transition, the atomic configuration tends to relax to a new equilibrium configuration, whose energy difference with the previous configuration is labeled as E_{relax}. On the other hand, the thermal energy $E_{thermal}$ is related to the

[3]The calculations are performed using DFT with the HSE06 functional as implemented in the VASP package. We have used 37.5% mixing of Hartree-Fock exchange in the functional, and electron-ion interactions are treated using projector augmented wave potentials. An oxygen vacancy is simulated by removing an O atom from a 72-atom supercell. A 2×2×2 mesh of special k-points based on the Monkhorst-Pack scheme is chosen for the integrations over the Brillouin zone.

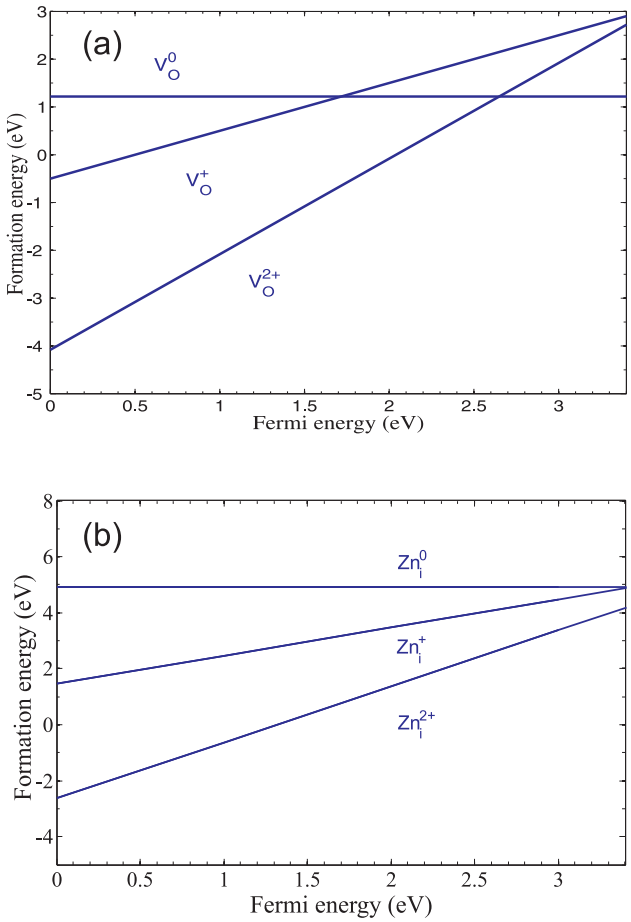

Figure 3.9: Calculated formation energies versus Fermi energies for (a) V_O and (b) Zn_i in the ZnO host material.

energy difference between the equilibrium configuration of charge state q_+^0 and the equilibrium configuration of charge state q_0^0. So the optical energy can be written as a function of the thermal energy

$$E_{optical} = E_{thermal} + E_{relax} \tag{3.12}$$

Therefore, the ionization energy coming from an optical experiment is always larger than or equal to the thermal ionization energy.

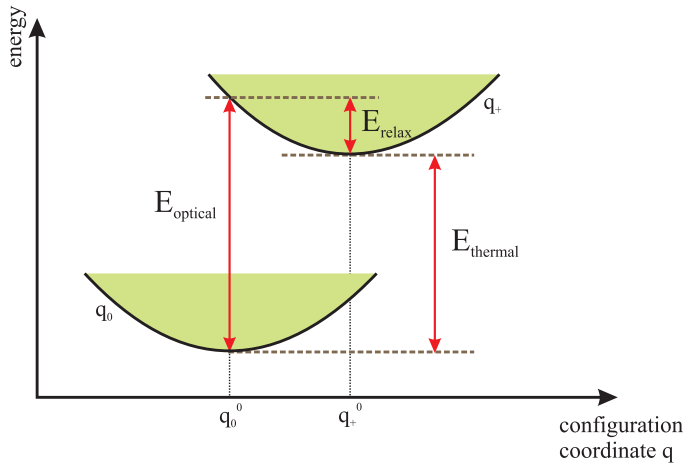

Figure 3.10: Configuration coordinates diagram illustrating the difference between optical and thermal transition energies.

Similar to the configuration coordinates diagram, the formation energy as a function of the Fermi energy plot can also be used to illustrate the difference between the thermal and optical transition energies. Figure 3.11 shows the formation energies for two charge states 1+ and 0 of an arbitrary defect as a function of the Fermi energy. In this figure, also the formation energy of the defect in charge state 1+ at the relaxed coordinates of charge state 0 is shown by the dashed line. Let us denote the total energy of a charge state q in the relaxed coordinates of charge state $q\prime$ as $E(q, X(q\prime))$. The thermal energy in our example is given by

$$E_{thermal} = E(+, X(+)) + E_v + E_g - E(0, X(0)) \tag{3.13}$$

Now, using Eq.(3.11)

$$\epsilon(0, +) = E(0, X(0)) - E(+, X(+)) - E_v \tag{3.14}$$

which shows that $E_{thermal}$ is given by

$$E_{thermal} = E_g - \epsilon(0, +) \tag{3.15}$$

and is also shown in Fig. 3.11. The optical energy is given by

$$\begin{aligned} E_{optical} &= E(+, X(0)) + E_v + E_g - E(0, X(0)) \\ &= E_g - \epsilon(0, +inX(0)) \end{aligned} \tag{3.16}$$

in which ϵ is now the transition level between charge state 0 and charge state 1+, but in both cases the relaxed coordinates for charge state 0 are considered. Also this $E_{optical}$ is shown in Fig. 3.11.

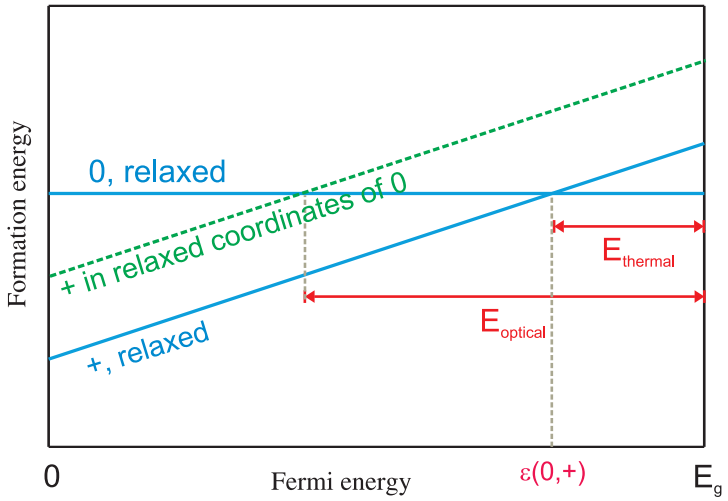

Figure 3.11: Formation energy as a function of the Fermi energy for two charge states 1+ and 0 of an arbitrary defect in a system.

To show the importance of looking at relaxed charged systems, consider Fig. 3.12 presenting the formation energies as a function of the Fermi energy for Zn_i defect in ZnO. It is shown that the transition $\epsilon(0, 2+)$ of the relaxed system, occurs in the conduction band and as a result the Zn_i defect acts as a shallow donor in ZnO. However considering the transition $\epsilon(0, 2+inX(0))$, one can conclude that the Zn_i acts as a deep donor in ZnO which is a completely different result.

3.5.4 Chemical potentials

As it is mentioned previously, the chemical potentials represent the energy of the reservoirs with which atoms are being exchanged. The chemical potentials highly depend on the experimental growth conditions, and should be considered as variables in the expression of the formation energy.

For example, the experimental growth conditions for a binary system such as ZnO can be Zn-rich, O-rich, or anything in between. The formation energy of ZnO can be written as [94, 95]

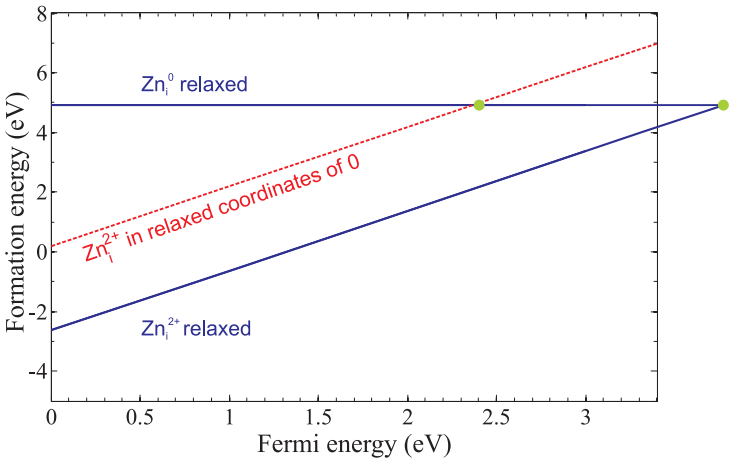

Figure 3.12: Formation energy as a function of the Fermi energy for Zn_i in ZnO.

$$\begin{aligned}\Delta H_f[ZnO] &= E[ZnO] - \mu_{Zn}^{Znbulk} - \mu_O^{O_2 molecule} \\ &= (\mu_{Zn}^{ZnO} + \mu_O^{ZnO}) - \mu_{Zn}^{Znbulk} - \mu_O^{O_2 molecule}) \\ &= (\mu_{Zn}^{ZnO} - \mu_{Zn}^{Znbulk}) + (\mu_O^{ZnO} - \mu_O^{O_2 molecule}) \\ &= \Delta\mu_{Zn} + \Delta\mu_O \end{aligned} \tag{3.17}$$

where we assumed that ZnO is prepared from Zn bulk and O_2 gas. In Eq.(3.17) $\mu_{Zn/O}^{ZnO}$ indicates the energy of a Zn/O atom in ZnO. μ_{Zn}^{Znbulk} indicates the energy of a Zn atom in bulk Zn, and $\mu_O^{O_2 molecule}$ denotes the energy of a O atom in the oxygen molecule. To avoid the precipitation into bulk zinc and oxygen gas the upper limits are set as

$$\Delta\mu_{Zn} \leq 0 \quad ; \quad \Delta\mu_O \leq 0 \tag{3.18}$$

So extreme O-rich conditions place an upper limit on μ_O by

$$\mu_O^{max} = \mu_O^{O_2 molecule} = \frac{1}{2} E[O_2 molecule] \tag{3.19}$$

This upper limit for oxygen leads to a lower limit (Zn-poor) on μ_{Zn} given by

$$\mu_{Zn}^{min} = \mu_{Zn}^{Znbulk} + \Delta H_f^{ZnO} = E[Znbulk] + \Delta H_f^{ZnO} \tag{3.20}$$

Similarly the Zn-rich conditions imply

$$\mu_{Zn}^{max} = E[Znbulk] \tag{3.21}$$

and the oxygen chemical potential corresponding to the Zn- rich conditions is then called O-poor condition and is given by

$$\mu_{O}^{min} = \frac{1}{2}E[O_2molecule] + \Delta H_f^{ZnO} \tag{3.22}$$

The above equations show the possible variation of Zn and O chemical potential when ZnO is formed.

For ternary systems, the variation of the chemical potentials is more complicated, because there are more degrees of freedom in the experimental growth conditions. For example, consider a ternary compound such as $ZnCo_2O_4$; the total formation energy of the system in order to maintain the stability is written as

$$\Delta H_f[ZnCo_2O_4] = \Delta\mu_{Zn} + 2\Delta\mu_{Co} + 4\Delta\mu_{O} = -12.85 \quad eV \tag{3.23}$$

where for this ternary system $\Delta\mu_{Zn} = \mu_{Zn}^{ZnCo_2O_4} - \mu_{Zn}^{Znbulk}$, $\Delta\mu_{Co} = \mu_{Rh}^{ZnCo_2O_4} - \mu_{Co}^{Cobulk}$, and $\Delta\mu_{O} = \mu_{O}^{Co_2O_4} - \mu_{O}^{O_2molecule}$. To avoid the elemental precipitation into the bulk zinc, bulk cobalt, and oxygen gas the upper limits are set as

$$\Delta\mu_{Zn} \leq 0 \quad ; \quad \Delta\mu_{Co} \leq 0 \quad ; \quad \Delta\mu_{O} \leq 0 \tag{3.24}$$

One can plot a triangle with the above conditions. Figure 3.13 shows schematically the possible chemical potential range in the ternary system $ZnCo_2O_4$. The three vertices are as follows

- **vertex A** : Zn/Co-rich (O-poor) condition
  $\Delta\mu_{Zn} = 0 \quad ; \quad \Delta\mu_{Co} = 0 \quad \rightarrow \quad \Delta\mu_{O} = \Delta H_f[ZnCo_2O_4]/4$
- **vertex B** : Zn-rich (Co-poor) condition
  $\Delta\mu_{Zn} = 0 \quad ; \quad \Delta\mu_{O} = 0 \quad \rightarrow \quad \Delta\mu_{Co} = \Delta H_f[ZnCo_2O_4]/2$
- **vertex C** : Co-rich (Zn-poor) condition
  $\Delta\mu_{Co} = 0 \quad ; \quad \Delta\mu_{O} = 0 \quad \rightarrow \quad \Delta\mu_{Zn} = \Delta H_f[ZnCo_2O_4]$

The line joining the vertices B and C refers to O-rich condition($\Delta\mu_O = 0$).

Considering the constraints of Eq.(3.24), inside the triangle the ternary structure is thermodynamically stable. But for a ternary system, there are more constraints because of the formation of competing binaries e.g. ZnO

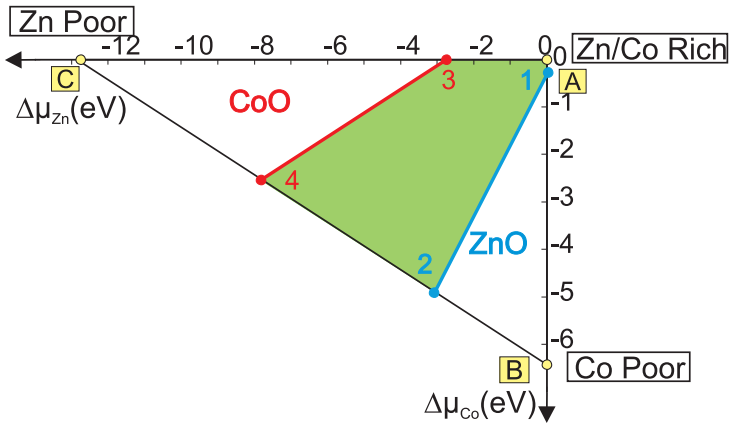

Figure 3.13: Schematic illustration for accessible chemical potential range in a ternary system $ZnCo_2O_4$.

and CoO in case of $ZnCo_2O_4$. These constraints which limit the possible accessible range of chemical potentials are as follows

$$\Delta\mu_{Zn} + \Delta\mu_O \leq \Delta H_f[ZnO] = -3.06 \quad eV \tag{3.25}$$

$$\Delta\mu_{Co} + \Delta\mu_O \leq \Delta H_f[CoO] = -2.53 \quad eV \tag{3.26}$$

In the Fig. 3.13, the stable region for $ZnCo_2O_4$ is shown in green. The vertices of this stable region are labeled as 1,2,3,4. The first vertex, 1, refers to the Zn rich condition ($\Delta\mu_{Zn} = 0$) and using Eq.(3.25), $\Delta\mu_O$ is calculated. Then using the ternary stability conditions of Eq.(3.23), $\Delta\mu_{Co}$ is obtained. The coordinates of vertex 1 thus correspond to: ($\Delta\mu_{Zn} = 0$;$\Delta\mu_{Co}$;$\Delta\mu_O$).

The second vertex, 2, corresponds to the O rich condition ($\Delta\mu_O = 0$). Using Eqs.(3.25)and (3.23), $\Delta\mu_{Zn}$ and $\Delta\mu_{Co}$ are obtained respectively. Below the line joining vertex 1 with 2, Eq.(3.25) is not satisfied and ZnO will form instead of $ZnCo_2O_4$.

Similarly, vertex 3 and 4 refer to the Co rich and O rich condition respectively and are determined from Eq.(3.26) and from the stability of the host in Eq.(3.23). Above the line joining vertex 3 with 4, CoO will be formed.

For the formation energy calculations, according to the experimental growth condition one can consider any of these vertices for the accessible range of the chemical potentials.

3.5.5 Accuracy and error

A number of factors should be considered in order to do an accurate defect calculation. Apart from the parameters such as the plane wave energy cut-off and k-point sampling in the density functional theory calculations, the choice of the supercell size is also an important issue in defect calculations. The larger the supercell size, the closer the results are to an isolated defect. Increasing the supercell size reduces the electrostatic interactions between charged defects in neighboring cells, but is more computationally intensive.

Another important source of errors in the DFT calculations, is the standard underestimation of the band gap in the LDA approximation and thus in the defect calculations. The size of this error in the defect calculations depends on how many electrons are located in the defect states, on the character of the defect state (valence band versus conduction band character), and on the size of the underestimation of the band gap. In the next section, some theoretical methods which are used in this thesis to eliminate the band gap error are discussed.

3.6 Correction methods

In chapter 2 the underestimation of the band-gap by the commonly used LDA or GGA functionals has been discussed. Doping a material with defects usually induces occupied states in the band gap, which have a certain fraction of conduction- against valence-band character. So their positions with respect to the VBM can be underestimated considerably, which affects the calculation of transition levels and formation energies to a considerable amount. Therefore the underestimation of the band gap may lead to large errors in the calculations (specially in case of wide band gap semiconductors).

To deal with the standard underestimation of the band gap in DFT approximations and thus in the defect calculations, different approaches have been employed, including a rigid upward shift of the conduction bands and defect levels [92], parameterized formation energies [96], or a semiempirical correction scheme [97]. A more recent correction scheme applies an extrapolation method based on the LDA+U approximation [98]. Many-body perturbation theory in the GW approximation is also a choice for the calculation of defect levels [99]. In principle an alternative computational scheme that suffers less from the band gap problem is the hybrid functional approach [60, 100] which has led to considerable improvement in the study of defects in materials. Approximations based on GW and hybrid functionals are typically computationally demanding for the required supercell sizes.

To study the electronic properties of defects and impurities in some TCO materials, the extrapolation technique is used in chapters 4 and 5, and the hybrid functional approach is used in chapters 6, 7 and 8 of this thesis. In the following the extrapolation technique is briefly explained.

3.6.1 The extrapolation technique

The LDA+U method was introduced in chapter 2, where a semi-empirical term was added to the LDA energy functional only for the localized orbitals which have a strong correlation. These strong Coulomb interactions are not sufficiently described in LDA. So the LDA+U method is mostly used for strongly correlated materials, such as transition metals having partially filled d or f bands. The LDA+U method usually affects both valence and conduction bands [49]. For example in the case of ZnO, the valence and conduction bands are composed mainly of Zn 3d and Zn 4s states respectively. Introducing an appropriate U value leads to more localized Zn 3d bands and therefore to a reduction of a repulsion with the O p states at the VBM (it pushes the VBM downward). This causes the Zn 4s conduction bands to become more delocalized and thus their energy increases (it pushes the CBM upward). Therefore the LDA+U method partially corrects the band gap.

An extrapolation technique based on the LDA and LDA+U calculations was employed to reach the experimental band gap and corresponding corrected transition levels and formation energies [98, 101, 102]. In the following this technique is briefly explained.

It is discussed in section (3.5) that the formation energies and transition levels for a certain defect in a material can be calculated from Eq.(3.9) and Eq.(3.11) respectively. These parameters should be calculated within the LDA and LDA+U method separately. The LDA+U method provides a partial but physically important correction of the band gap. The remaining correction is done with the extrapolation technique in order to remove the intrinsic LDA error. The extrapolated transition level is given by

$$\epsilon(q,q\prime) = \frac{\epsilon(q,q\prime)^{LDA+U} - \epsilon(q,q\prime)^{LDA}}{E_g^{LDA+U} - E_g^{LDA}}(E_g^{exp} - E_g^{LDA+U}) + \epsilon(q,q\prime)^{LDA+U} \quad (3.27)$$

where E_g^{LDA} and E_g^{LDA+U} are the band gaps given by the LDA and LDA+U approximations. $\epsilon(q,q\prime)^{LDA}$ and $\epsilon(q,q\prime)^{LDA+U}$ are the calculated transition points between charge states q and $q\prime$ within LDA and LDA+U approximation, and E_g^{exp} is the experimental gap. It should be noted that this extrapolation is applicable when the valence- and conduction-band character

of the defect state does not change when the gap is corrected, and only the position of the state is shifted in the gap.

Furthermore there should also be some corrections for formation energies. According to Eq.(3.9) the formation energy of a charged defect depends on the position of the VBM. It is assumed that this position is given by the value in the LDA+U approach and does not experience any extra shifts when the band gap is corrected [49]. It is assumed that all of the remaining corrections occur in the conduction band.

When the defect state is not occupied, the shift in its position will not affect the formation energy, and the formation energy of the defect should be well approximated by the LDA+U value. For example, the oxygen vacancy in the 2+ charge state in ZnO has a defect state which is free of electrons. The corrected formation energy for this defect state is thus equal to its LDA+U value. After we have a value for the 2+ charge state, we can find extrapolated values for the formation energies of the other charge states + and 0 as well.

Essential to the method is the existence of a stable charged state which is not occupied and therefore does not suffer from the band gap problem. However such a state does not always exist. For a partially occupied defect state, the shift in formation energy from LDA to LDA+U includes contributions from both the shift in the VBM and the shift in the defect state. Since the extra correction to the VBM is neglected, there is only a correction due to the shift in the Kohn-Sham defect state. This shift is proportional to the number of electrons that occupy the defect state. Therefore similar to Eq.(3.27) the formation energy, for a defect state with occupancy n, can be extrapolated according to

$$E_f = \frac{\epsilon(q,q\prime)^{LDA+U} - \epsilon(q,q\prime)^{LDA}}{E_g^{LDA+U} - E_g^{LDA}}(E_g^{exp} - E_g^{LDA+U})n + E_f^{LDA+U} \qquad (3.28)$$

The extrapolation technique is confirmed to give reliable results for the transition energies between different charge states of the impurity, both for ZnO with interstitial H [103] as for ZnO doped with a group III element [97]. However the use of this method is limited to materials with semicore d orbitals, and for states that are more delocalized, it may lead to wrong results [103].

Chapter 4

Hydrogen Impurities and Native Defects in CdO

4.1 Introduction

In this chapter of the thesis, we have used first principles calculations to study point defects in CdO based on density functional theory within the local density approximation and beyond (LDA+U).

As it is mentioned in chapter 1, an important class of materials with an already widespread application area are the TCOs. These materials combine electrical conductivity and optical transparency and are essential for photovoltaic and optoelectronic applications. The standard TCO in commercial use is tin-doped indium oxide (ITO). However, further development of practical thin-film transparent conducting oxide semiconductors is necessary since a stable supply of ITO cannot be assured because indium is a very expensive and scarce material [2]. In this regard, other post-transition metal oxides with wide band gaps and the ability to sustain high concentrations of electrons with high mobility are being explored.

As made, the three prototype TCOs, ZnO, SnO_2, and In_2O_3, show typically n-type conductivity. The understanding of the source of this unintentional conductivity has been a topic of intense research in the last decade. While oxygen vacancies were originally held responsible for the n-type conductivity [104, 4] in these TCOs, ab initio studies have revealed that the oxygen vacancy is a deep level donor and therefore cannot account for the unintentional conductivity. On the contrary, these studies also re-

The results of this chapter were published as: M. N. Amini, R. Saniz, D. Lamoen, and B. Partoens, Journal of Applied Physics **110**, 063521 (2011)

vealed instead that interstitial hydrogen forms a shallow donor in these oxides [105, 106, 107]. Furthermore, while an observed dependence of conductivity on oxygen partial pressure is usually taken as evidence for the importance of native defects, Janotti and Van de Walle [102] showed that substitutional hydrogen in a multicenter bond configuration can also account for the partial pressure dependence of the electrical conductivity. Recently, however, calculations based on hybrid functionals again claim the oxygen vacancy in SnO_2 and In_2O_3 to be shallow, while it is a deep level in ZnO [108]. This last result for ZnO is also confirmed by more accurate GW calculations [109].

Cadmium oxide (CdO) is one of the TCO materials which perhaps has received the least attention. This is mostly because of the toxicity of Cd and the relatively narrow band gap of CdO. However, it has demonstrated 5-10 times higher electron mobilities than in commercially available TCOs [110]. It can be a strong n-type semiconductor with a carrier concentration which is very sensitive to temperature: as temperature increases, the electron mobility increases from $\sim$ 1 to 220 $cm^2V^{-1}s^{-1}$ [110]. It is also shown that a solid solution of CdO in ZnO results in ternary (Zn,Cd)O, which is a suitable candidate for devices operating in the visible spectral range [111].

Recently, two experimental studies on the formation of defects in CdO have appeared [112, 113]. In Ref. [112] it was found that not only hydrogen impurities are donors in n-type CdO, but, in contrast to ZnO, also native defects -most likely oxygen vacancies. Furthermore, it was claimed that the electrical behavior of these defects is unified by a single energy level, the charge neutrality level, an idea which was already introduced in the late eighties [114]. At this energy level, the formation energy for creating donor and acceptor native defects is equal. After bombarding the CdO sample with He^+ ions, creating in such a way these native defects, it was found that the Fermi level stabilized at 0.4 eV above the conduction band minimum. Furthermore, the transition level $H(+/-)$ between the positive interstitial hydrogen defect and the negative one was determined by diffusion of hydrogen in a nominally undoped CdO sample. The $H(+/-)$ was also found to lie 0.4 eV above the conduction band minimum. This led to the conclusion of the existence of a unified energy level describing the electrical behavior of defects. However, in the experimental work of Ref. [113] also native defects in CdO were created, but now by bombarding with heavier ions than in Ref. [112]. The stabilization of the Fermi level was found to be at 1 eV above the conduction band minimum. They convincingly showed that only by using the heavier ions to bombard the sample a large enough damage production rate can be achieved to correctly measure the stabilized Fermi level energy. The value of 1 eV should therefore be considered as the correct value of the Fermi level stabilization in CdO. However, in the experiment

of Ref. [113], the effect of hydrogen impurities in CdO was not studied. As such, the existence of a unification of both transition levels is still an open question.

In this chapter, these experimental studies motivated us to study the donor and/or acceptor character of the hydrogen impurity in CdO (interstitial and substitutional at an oxygen site), and the most likely occurring native defects in the above described experiments in CdO, namely the oxygen vacancy, the cadmium vacancy, the oxygen interstitial and the Cd interstitial by ab initio calculations. We investigate if all these impurities are good candidates to explain the observed shallow donor character in the experiments, and if the calculations support the concept of a unified charge neutrality level. The same month our research were published, a similar theoretical study on the sources of conductivity in CdO appeared [115]. Therefore we conclude this chapter with a comparison with our results and those of Ref. [115].

4.2 Computational details

We perform first-principles calculations using density functional theory (DFT) within the local density approximation (LDA) and the LDA+U approach, as implemented in the Vienna ab initio simulation package [66, 116]. Electron-ion interactions are treated using projector augmented wave potentials [67, 68, 65]. The cadmium ($5s^2 4d^{10}$), oxygen ($2s^2 2p^6$) and hydrogen ($1s^1$) electrons are treated as valence electrons. The defects are simulated by adding (removing) host atoms to (from) a 216-atom $3 \times 3 \times 3$ cubic supercell with periodic boundary conditions. A $2 \times 2 \times 2$ mesh of special k-points based on the Monkhorst-Pack scheme [63] is chosen for the integrations over the Brillouin zone. Tests as a function of plane-wave cutoff and k-point sampling show that our results are numerically converged to within ~ 2 meV in total energy. Therefore the electron wavefunctions are described using a plane-wave basis set with an energy cutoff of 750 eV. Note that the convergence with respect to self-consistent iterations was assumed when the total energy difference between cycles was less than 10^{-4} eV, and the geometry relaxation tolerance was better than 0.01 eV/Å.

To deal with the standard underestimation of the band gap in the LDA approximation, and thus in this defect calculation, we make use of the combination of the LDA and LDA+U method to correct this band gap problem as was recently applied successfully for ZnO and described in Ref. [86]. We have used U=2.2 eV for Cd, as calculated in Ref. [49].

4.3 Geometrical and electronic structures

We study CdO in its ground state crystal structure, i.e. rocksalt. The calculated lattice parameter is 4.654 Å, in good agreement with the experimental value of 4.696 Å [117]. Figure 4.1, shows the bulk crystal structure of CdO.

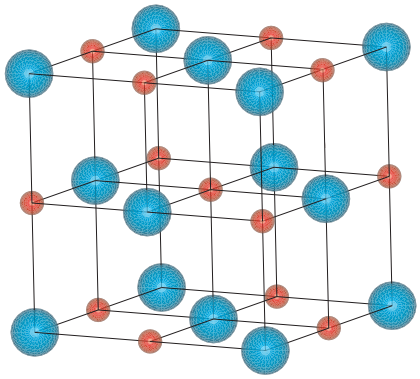

Figure 4.1: Crystal structure of CdO - rocksalt ($Fm\bar{3}m, \#225$). Blue color is for the cadmium atoms while red shows the oxygen atoms.

CdO is a semiconductor with an indirect band gap of 0.8 eV between the top of the valence band at the L point and the minimum of the conduction band in the Γ point, [118] while our DFT-LDA calculations result in a semi-metallic behaviour with a band overlap of -0.45 eV, in agreement with earlier ab initio results [119]. The experimental direct gap at the Γ point is 2.28 eV. [118] Also this direct gap is strongly underestimated in our DFT-LDA calculations, which give 1.04 eV. The calculated band structure of CdO within LDA is shown in Fig. 7.2.

It is known that the LDA+U approach improves the description of the bands related to the semicore d states, leading to a partial correction of band gaps in materials such as ZnO, SnO_2, and InN [49]. Therefore we have also applied the LDA+U approach to calculate the electronic structure of CdO. The LDA+U approach only marginally increases the separation between valence and conduction bands. Within this approach, CdO is still semi-metallic with a negative band overlap of -0.22 eV, and the direct gap at the Γ point is found to be 1.15 eV.

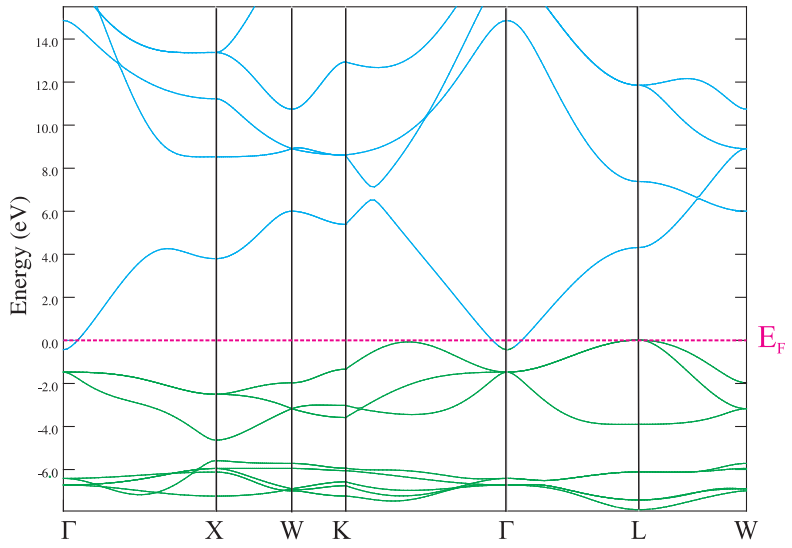

Figure 4.2: Electronic band structure of CdO calculated using LDA.

4.4 Formation energy treatment

The concentration of point defects and impurities depends on their formation energies. Defects with high formation energies will occur in low concentrations. As it is discussed in chapter 3, the formation energy of a defect or impurity in different charge states is defined in Eq.(3.9). The chemical potentials in the formation energy equation depend on the experimental growth conditions, which can be either Cd-rich, O-rich or anything in between. Extreme O-rich conditions place an upper limit on μ_O by

$$\mu_O^{max} = \frac{1}{2}E[O_2] \tag{4.1}$$

This upper limit for oxygen leads to a lower limit on μ_{Cd}^{min} given by the thermodynamic stability condition for CdO

$$\mu_{Cd} + \mu_O = E_{tot}[CdO] \tag{4.2}$$

where $E_{tot}[CdO]$ is the total energy of a two-atom unit cell of bulk CdO. The upper limit on the cadmium chemical potential then results in a lower limit on the oxygen chemical potential

$$\mu_O^{min} = \frac{1}{2}E[O_2] + \Delta H_f[CdO] \tag{4.3}$$

with $\Delta H_f[CdO]$ the enthalpy of formation of bulk CdO (negative for a stable compound). Further we fix the value for μ_H to half the energy of a H_2 molecule[1].

As it is mentioned in chapter 3, a method to determine ΔV is to consider the total electrostatic potential at some point, or region, far from the defect and to align it with the potential in the same region in the undoped supercell [9]. In our work we apply an alternative method, which is computationally very simple and economical, and does not depend on the choice of the point or region in the supercell used for the calculation. Briefly, consider $\delta(\vec{r}) = V_u(\vec{r}) - V_d(\vec{r})$, where V_d (V_u) is the total electrostatic potential in the doped (undoped) supercell (we take the undoped system as reference). Assume that the impurity distorts the potential only in a limited region within the supercell. Within this region δ is a position dependent function, varying more or less rapidly depending on how strong the distortion is. Outside this region, since the potential is not distorted by the impurity, V_d and V_u are just shifted respect to each other and δ takes precisely the constant value ΔV. Obviously, then, given a set of points uniformly distributed in the supercell, the most likely value of δ over this set is ΔV. Thus, to determine ΔV one could use, e.g., a histogram of the values taken by δ over a grid of points in the supercell. The histogram will be strongly peaked at the energy interval containing ΔV, without the need to know where in the supercell the potential is not distorted by the impurity. Instead of building a histogram, however, it is more efficient and accurate to use the linear tetrahedron method [120] to calculate the volume of points in the supercell corresponding to each energy interval. A few calculations with a decreasing length of the energy intervals will rapidly converge to a precise value of ΔV. This is the method we use here.

By using the formation energies of different charge states, one can also calculate the transition levels between them. These are the ones that are most relevant to experiment. The transition level $\varepsilon(q/q')$, is the Fermi energy for which the formation energies of charge states q and q' are equal.

As it is mentioned above, even by applying the LDA+U approach, CdO has a negative band gap. The fact that the LDA and LDA+U approaches are unable to describe CdO as a semiconductor has consequences on the choice

[1]Note that, in case of an equilibrium with water, the formation energy of hydrogen defects is also coupled with the oxygen chemical potential in oxygen rich conditions and with the cadmium chemical potential in oxygen poor conditions. This lowers the hydrogen chemical potential in oxygen rich conditions by 1.44 eV and in oxygen poor conditions by 0.3 eV. Consequently, it raises the formation energies of the hydrogen interstitial and substitutional defects by the same amounts. However, this has no further consequences on our conclusions further down.

of the k-point mesh when calculating the formation energy of the defects in supercells, i.e., we have checked that our k-point mesh only includes k-points for which all valence states are occupied and conduction bands are empty.

4.5 Native defects

Fig. 4.3(a) shows the formation energy of the oxygen vacancy V_O as a function of Fermi level E_F for three possible charge states V_O^0, V_O^+, and V_O^{2+} under oxygen poor conditions. No correction for the underestimation of the band gap has been applied yet. The vertical lines mark the calculated and experimental value of the direct band gap at Γ. As the reference of the Fermi level E_F is chosen to be the top of the valence band at the Γ point of the primitive unit cell, we can immediately deduce from Figs. 4.3 if the defect levels are close to or in the conduction band. We find that the oxygen vacancy in the V_O^{2+} charge state is stable up to a Fermi energy of $E_F = 1.78$ eV with a negative formation energy. We have applied two correction steps in our calculations. The first step in the band gap correction scheme results in a transition level in the conduction band, as shown in Fig. 4.3(b), which shows the formation energies of the different charge states of the same oxygen vacancy obtained within the LDA+U approach. Further we use the LDA and LDA+U results to extrapolate to the experimental direct gap value, using the extrapolation technique as proposed first in Ref. [98] and extensively discussed in Ref. [86]. (The extrapolation technique is also more explained in chapter 3)

Note that we use the value of the direct gap at the Γ point of the primitive cell for the extrapolation, which is consistent with our choice of reference E_v for the Fermi level E_F. After extrapolation we obtain that the crossing between V_O^{2+} and V_O^+ occurs at 1.99 eV, and between V_O^+ and V_O^0 at 3.06 eV, which is in the conduction band, as shown in Fig. 4.3(c). (The correction scheme for formation energies is discussed in the next paragraph). Therefore we can conclude that the oxygen vacancy is a shallow donor and can be a cause of unintentional n-type conductivity in CdO. As such it is a good candidate to explain the observed n-type behavior in CdO due to the creation of native defects after particle irradiation in Refs. [112, 113]. The fact that the oxygen vacancy is a shallow donor is in contrast to what was found for ZnO [105, 109] and in some references for SnO_2 and In_2O_3 [106, 107].

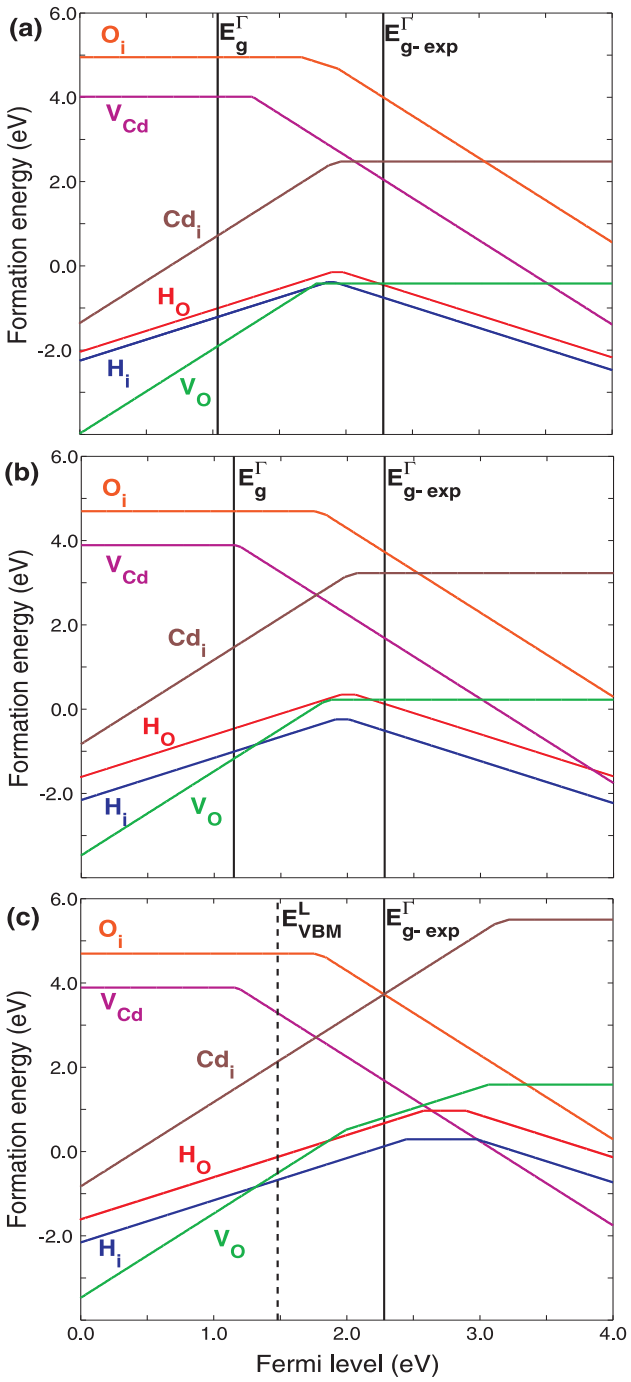

Figure 4.3: Formation energies as a function of Fermi level in CdO for a hydrogen interstitial, hydrogen substitutional, oxygen vacancy, cadmium vacancy, oxygen interstitial and cadmium interstitial for (a) LDA, (b) LDA+U and (c) extrapolated values. Results for Cd-rich conditions are shown.

In order to obtain the corrected formation energies, we proceed as follows. The formation energies depend on the position of the valence band maximum and also the defect state in the band gap. It is assumed that by applying LDA+U, one can get the correct valence band maximum and that the remaining correction occurs in the conduction band. So when the defect state is not occupied, we should only correct the position of the VBM which is assumed to be well approximated within LDA+U [86]. In the case of the oxygen vacancy, removing one oxygen atom breaks its neighbor bonds and creates 6 cadmium dangling bonds with a total of 2 electrons. In the 2+ charge state of the oxygen vacancy the defect level is not occupied and one can take the LDA+U formation energy as the final result. Once we have the formation energy value for one charge state, we can then obtain extrapolated values for formation energies for the other charge states from the already obtained extrapolated crossings ε [86]. The results are shown in Fig. 4.3(c).

In ZnO (Ref. [98]) and SnO_2 [106] large differences in local lattice relaxations were found for different charge states of the oxygen vacancy. For the neutral V_O^0, the nearest neighbor Zn and Sn atoms were found to relax inward, while for V_O^+ and V_O^{2+} the relaxations are outward. However, for the oxygen vacancy in CdO, we find that all Cd nearest neighbors relax outward for all charge states: 3.04 % for V_O^0, 3.41 % for V_O^+, and 3.61 % for V_O^{2+} of the equilibrium Cd-O bond length.

Note that these relaxations are up to an order of magnitude smaller than what was found for ZnO (Ref. [98]) and SnO_2 [106]. This is due to the highly ionic nature of CdO among the IIB-VIA compounds[121], which causes it to form only in the rocksalt structure, a typical structure of ionic insulators. The large difference in local lattice relaxations around the oxygen vacancy for different charge states in ZnO and SnO_2 were held responsible for the so-called negative-U behavior, implying that $\varepsilon(2+/+)$ lies above $\varepsilon(+/0)$ and the 1+ charge state of the oxygen vacancy is not stable for any position of the Fermi level. In CdO we find on the contrary that the V_O^+ state is indeed stable.

Let us now consider the cadmium vacancy native defect. Figures 4.3(a) and (b) show also the calculated formation energies for the cadmium vacancy V_{Cd} in the different charge states V_{Cd}^0, V_{Cd}^- and V_{Cd}^{2-} in the Cd rich limit within the LDA and LDA+U approaches, respectively. In CdO, removing one cadmium atom from a cell breaks six bonds. These six oxygen dangling bonds lie close to the valence band maximum and since they are only partially filled they can accept extra electrons. As the cadmium vacancy defect level has valence band character, no extra band gap correction scheme must be applied in our approximation, and the formation energies obtained within the LDA+U approach are approximated to be the final results (also shown again

in Fig. 4.3(c)). The transition between the formation energy of the V_{Cd}^0 and the V_{Cd}^- state occurs at 1.16 eV above the valence band maximum at the Γ point of the primitive unit cell, which is our reference energy E_v. The absolute valence band maximum is however at the L point in the primitive cell and lies 1.48 eV higher then the maximum at the Γ point. This level is indicated by the dashed line in Fig. 4.3(c). We can conclude that the cadmium vacancy is a shallow acceptor in CdO, however with a much higher formation energy then the oxygen vacancy, which explains the n-type behavior of CdO. The oxygen atoms around the vacancy relax outward by 7.80 % for the V_{Cd}^0, by 7.68 % for the V_{Cd}^- and by 7.47 % for the V_{Cd}^{2-} of the equilibrium Cd-O bond length.

In Ref. [112] and [122], schematic formation energy diagrams were used to support the charge neutrality concept. The same authors also studied the charge neutrality in InN by bombarding the sample with ions to create native defects [123], in a similar way as was done for CdO [112]. The experimentally determined position of the charge neutrality level was also compared in Ref. [122] with the calculated formation energies of nitrogen and indium vacancies in InN as obtained in Ref [124]. The positively charged donor-like nitrogen vacancy V_N^+ and negatively charged acceptor-like indium vacancy V_{In}^{3-} were found to have the lowest formation energies and their crossing was found to lie close to the observed experimental charged neutrality level. In this way, the calculations supported the experimental findings. Let us now make the same analysis for CdO. Fig. 4.3(c) shows that the crossing between the oxygen vacancy V_O^+ and the cadmium vacancy V_{Cd}^{2-} occurs at 2.57 eV, i.e. 0.29 eV above the conduction band minimum, and thus far from the experimentally observed value of 1 eV above the conduction band minimum [113]. Furthermore, it is important to realize that this crossing point is also determined by the experimental growth conditions. The results in Fig. 4.3 are for the oxygen poor limit. But note that in the oxygen rich limit the V_O formation energies move up by 2.29 eV, while the V_{Cd} formation energies move down by the same value. Therefore, in the oxygen rich limit the crossing between both formation energies occurs in the band gap. As the crossing point depends on the chemical potentials of the species (which are assumed to be in thermodynamic equilibrium), a comparison with the experiment can only be made if the chemical potentials of the species in the experiment are known. So, generally the analysis of Ref. [122] is not applicable and the concept of a charge neutrality level for native defects is not well-defined. In the particular cases of the experiments of Refs. [112] and [113], the vacancies were created by bombarding the sample with heavy ions, but at the same time oxygen and cadmium at interstitial positions are produced. Therefore we also investigated these oxygen and cadmium interstitial defects. First we

calculate their formation energies and charge states, after which we compare the formation energy of the co-formation of a cadmium vacancy and a cadmium interstitial with the formation energy of the co-formation of an oxygen vacancy together with an oxygen interstitial.

Let us first consider the oxygen interstitial. We found that the preferential position of the oxygen atom is in the [100] plane between two cadmium and two oxygen atoms. After relaxation, the oxygen interstitial remains at the center of the plane while its four nearest neighbors relax outward by about 0.26 Å for oxygen and 0.41 Å for cadmium in all charge states. The calculated formation energies of the interstitial oxygen in the charge states O_i^0, O_i^- and O_i^{2-} without applying any band gap correction scheme are shown in Fig. 4.3(a) as function of the Fermi energy level and also within LDA+U approach in Fig. 4.3(b). By applying the LDA+U correction, the crossing point between O_i^0 and O_i^- shifts upward from 1.67 eV to 1.75 eV. Just as the cadmium vacancy defect level, the oxygen interstitial defect level has valence band character, and therefore no extra band gap correction scheme is applied, and the formation energies obtained within the LDA+U approach are the final results. The oxygen interstitial can thus be considered as a deep acceptor.

On the contrary the cadmium interstitial occupies the center of the cube which is surrounded by four cadmium and also four oxygen atoms in the CdO crystal. After relaxation, for all different charge states, all eight nearest neighbors shift outward by about 0.55 Å for the cadmium atoms and 0.12 Å for the oxygen atoms. For interstitial cadmium, the calculated formation energies in the charge states Cd_i^0, Cd_i^+ and Cd_i^{2+} without any band gap correction scheme and also within LDA+U approach are shown in Fig. 4.3(a) and (b) as a function of the Fermi energy level. The crossing point between Cd_i^{2+} and Cd_i^+ moves up from 1.87 eV to 1.98 eV within the first correction step. As there are no defect levels occupied in the cadmium interstitial in the charge state Cd_i^{2+}, its formation energy is given by the LDA+U result, from which the formation energies of the other charge states are deduced. They are also shown in Fig. 4.3(c). The cadmium interstitial is clearly a shallow donor and the final corrected crossing point between Cd_i^{2+} and Cd_i^+ is at 3.11 eV, thus 0.83 eV above the conduction band minimum.

Previously, we have calculated the formation energies of the vacancies for equilibrium growth conditions (for example under oxygen poor conditions). However, the vacancies in the experiment are not realized during the growth of the sample, but by bombarding the sample with ions [112, 113]. The knocked-out oxygen and cadmium atoms form interstitial defects. Therefore a description of the defect formation that comes closer to the experiments is considering the formation energy of the co-formation of a cadmium vacancy

and a cadmium interstitial, and an oxygen vacancy together with an oxygen interstitial. In this case, the formation energies do not depend on the choice of the chemical potential as in equation (3.9). As it was suggested that the interstitial atoms will finally cluster [113] we consider the formation energy of a cadmium vacancy in its ground state (V_{Cd}^{2-}) together with a neutral Cd_i, and an oxygen vacancy in its ground state (V_O^{2+} and V_O^{+}, depending on E_F) together with a neutral oxygen interstitial O_i. The formation energies as function of the Fermi level, after applying the band gap correction scheme, are shown in Fig. 4.4.

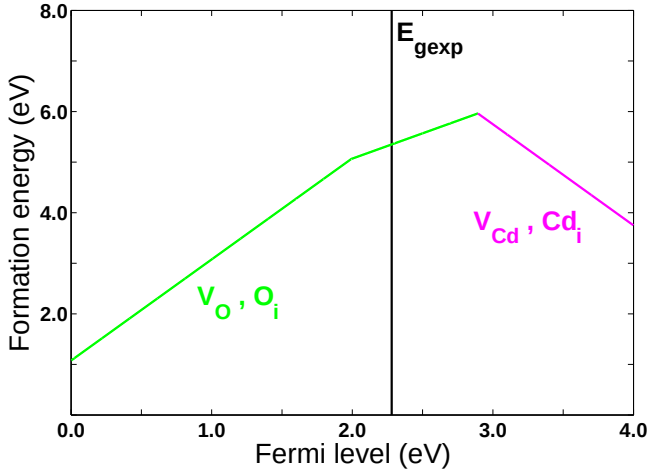

Figure 4.4: Formation energies as a function of Fermi level in CdO for $V_O + O_i$ and $V_{Cd} + Cd_i$.

The crossing between these different charge states of these double defects is found to be at 0.61 eV above the conduction band minimum. Note that this crossing is higher than found before for the V_O^{+} and V_{Cd}^{2-} case in the oxygen poor limit and is closer to the experimental observation of pinning of the Fermi level of 1 eV above the conduction band minimum. It is clear that in order to obtain a better agreement with experiment, it is necessary to have a better knowledge of the end states of the knocked-out oxygen and cadmium atoms after the ion bombardment, or at least an average value of their chemical potential in case there is a dynamical equilibrium between different end states.

4.6 Hydrogen defects

A charge neutrality level is however better defined for single defect species, like the hydrogen interstitial impurities, although it might be difficult to realize only one type of defect in the experiment. In this case, the absolute value of the formation energy of the positively and negatively charged defect depends on the choice of the chemical potential of hydrogen (and thus the experimental conditions), but not the crossing $H(+/-)$ between them.

Thus, it is of interest to investigate hydrogen impurities as they are a source of unintentional n-type doping, as hydrogen is commonly present in the various growth and processing environments. We find that hydrogen can be incorporated on interstitial sites (H_i) as well as on substitutional oxygen sites (H_O) in CdO. Let us first consider hydrogen in its interstitial form. H_i forms a strong bond with an oxygen atom. The O-H bond is, in all charge states, oriented along the [100] direction and the bond length is 0.98 Å, very close to the bond length in H_2O. The calculated formation energies of the interstitial hydrogen in the charge states H_i^+, H_i^0 and H_i^- are also shown in Fig. 4.3(a) as function of the Fermi energy level, again without any applied band gap correction scheme. We find that the formation energy is negative and only slightly larger than the V_O^{2+} oxygen vacancy up to $E_F = 1.31$ eV (in oxygen poor conditions). We find that within LDA the transition level between H_i^+ and H_i^0 is 1.86 eV. The LDA+U approach shifts it further till 1.91 eV (see Fig. 4.3(b)). Extrapolating further to the experimental value of the direct band gap at Γ leads to a crossing between the H_i^+ and H_i^0 levels at 2.45 eV. Just as in the 2+ charge state of the oxygen vacancy, no defect level is occupied for H_i^+, and the LDA+U formation energy will not change anymore when an extra band gap correction is applied. The other extrapolated formation energy, for H_i^0, is shown in Fig. 4.3(c). Interstitial hydrogen is thus a shallow donor in CdO and therefore a plausible cause of n-type conductivity, as also found in Refs. [119, 125], and like it is in ZnO, SnO_2, and In_2O_3. The Fermi level stabilization will be reached at the H^+ and H^- crossing, i.e. 0.43 eV above the conduction band minimum. This value is in a good agreement with the experimental value of 0.4 eV reported in Ref. [112].

As the second type of hydrogen incorporation, we consider hydrogen substitutional. H_O is sixfold coordinated and forms a multicenter bond with its six nearest neighbor Cd atoms. These six Cd atoms are only about 0.03 Å pushed away from their equilibrium position, for all charge states of the defect. Within this substitution, the H 1s orbital makes a bond with an electron in the doubly occupied state of the oxygen vacancy and locates deep in the valence band, while the third electron is transferred to the conduction band

minimum. So in the case of H_O^+ the defect state is empty and the formation energy obtained with the LDA+U approach will not change anymore when an extra band gap correction scheme is applied. The formation energies of the other charge states follow then from the extrapolation of the transition points. The formation energies are also included in Fig. 4.3(a) for the LDA results, Fig. 4.3(b) for the LDA+U results and Fig. 4.3(c) shows the extrapolated results for the conditions that favor the occurrence of these defects most, i.e., for oxygen poor conditions. Finally, the extrapolated transition level between H_O^+ and H_O^0 is found to be 2.58 eV. We can again conclude that H_O acts as a shallow donor. Furthermore, note that under these oxygen poor conditions, the formation energy of H_O is substantially higher than that of H_i. However, once a substitutional hydrogen defect is created, its stability is obtained by calculating the binding energy of H_O^+ with respect to V_O^{2+} and H_i^+ for $E_F < 1.99$ eV

$$E_f[H_O^+] - (E_f[H_i^+] + E_f[V_O^{2+}]) = 4.02 \text{ eV} - 2E_F \tag{4.4}$$

and with respect to V_O^+ and H_i^+ for $E_F > 1.99$ eV

$$E_f[H_O^+] - (E_f[H_i^+] + E_f[V_O^+]) = 2.02 \text{ eV} - E_F \tag{4.5}$$

These results are independent of the chemical potentials for hydrogen and oxygen. If $E_F > 2.02$ eV, the binding energy becomes negative and at $E_F = E_g$ it is -0.26 eV. This shows that once H_O^+ is formed, it will not dissociate in a H_i^+ and a V_O^+ defect in n-type CdO. As a consequence, even in the presence of hydrogen impurities, the conductivity will depend on the oxygen partial pressure.

4.7 Comparison of the results with a similar study

As stated in the introduction, a related study on the sources of conductivity in CdO has appeared recently. In Ref. [115] the HSE06 functional (with 25% mixing of Hartree-Fock exchange) is used to study intrinsic defects and hydrogen impurities in CdO. Here we make a comparison between our results obtained using the extrapolation method and the ones of Ref. [115] using the hybrid functional approach. Such a comparison between the extrapolation technique and hybrid functional calculations for defects in ZnO, SnO_2 and TiO_2 has already been reported in Ref. [103]. It is shown that within both methods, the positions of the transition levels with respect to the valence and conduction band edges are in good agreement, but the formation energies

are lower in the HSE approach. This difference in the formation energies is related to the downward shift of the VBM. The position of the VBM is assumed to be well approximated within the LDA+U method and the remaining correction for the band gap occurs only in the conduction band. However in the HSE approach further corrections for the position of the VBM are considered and thus it can describe the system more accurately [126]. The difference between the two methods might be larger for acceptor-like defects. Since an acceptor-like defect level has valence band character, no extra band gap correction scheme is applied in the approximation based on the extrapolation.

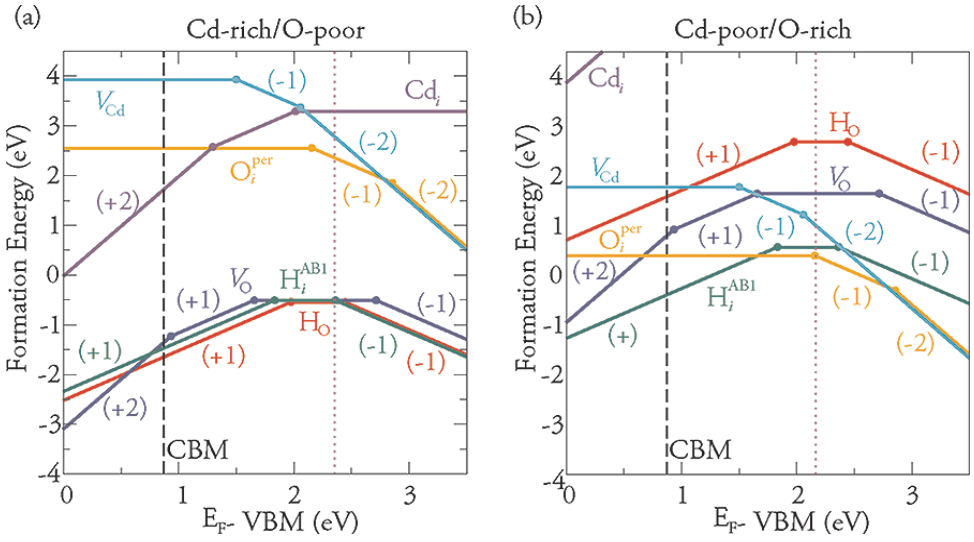

Figure 4.5: Formation energies for intrinsic and hydrogen defects under (a) Cd-rich/O-poor conditions and (b) Cd-poor/O-rich conditions. The solid dots represent the transition levels. The black dashed line indicates the position of the conduction band maximum (CBM), with the purple vertical dotted line representing the maximum achievable Fermi level before compensation occurs (Taken from Ref. [115]).

Such a comparison between our results (using the extrapolation technique for the band gap correction) and those of Ref. [115] (using HSE06 functional for the band gap correction) can also be useful. Figure 4.5 shows the formation energies for intrinsic and hydrogen defects under both Cd-rich/O-poor conditions and Cd-poor/O-rich conditions taken from Ref. [115] (dashed line in Fig. 4.3(c) corresponds with $E_F = 0$ in Fig. 4.5). It is found that V_O and H impurities are the dominant defects in CdO. The V_O acts as a doubly

ionized shallow donor, and the H impurities act as shallow donors in CdO. Acceptor-like defects such as V_{Cd} and O_i are also studied, and it is concluded that p-type CdO will never be realized as the formation energies of the p-type defects are too high in energy. Finally, the doping limits of CdO have been addressed. By using the ionization levels of all defects, it is found that the compensation by p-type defects does not occur until > 1.2 eV above the CBM depending on the growth conditions. Comparing the results shows that for donor-like defects the computationally less expensive extrapolation technique yields results similar to the HSE ones. All donor-like defects such as H_i, H_O, V_O, and Cd_i act as shallow donors in CdO with transition points above the conduction band. Although the positions of the transition levels with respect to the valence and conduction band edges are not exactly the same, the characters of donor-like defects are in good agreement within both approaches. The calculated formation energies are also lower in the HSE approach, similar to the conclusion in Ref. [103]. On the contrary, for the calculations related to the acceptor-like defects such as V_{Cd} and O_i the outcome is different. For example, in case of V_{Cd} our results show a shallow acceptor behavior whereas in Ref. [115] it is a deep acceptor. This difference can be attributed to the approximation made for the position of the VBM with the extrapolation technique.

4.8 Conclusions

We can conclude that it is easier to realize a TCO with CdO then with ZnO, because also oxygen vacancies cause n-type behavior and act as shallow donors, while they create deep levels in ZnO. This agrees with the experimental observations in Ref. [112, 113] where native defects -most likely oxygen vacancies- where shown to be donors in n-type CdO. We also found that cadmium vacancies are shallow acceptors, however with a higher formation energy than oxygen vacancies. It is also shown that in the case of native defects, the charge neutrality level is not uniquely defined and depends on the chemical potentials of the species and a comparison with experiment can only be made if the chemical potentials of the species in experiment are known. Furthermore, we have also investigated the effect of a hydrogen interstitial in CdO and it is shown that it acts as a shallow donor. The charge neutrality level for the hydrogen interstitial is better defined, since the crossing between different charge states does not depend on the chemical potential of hydrogen. We find that the Fermi level stabilization for hydrogen interstitial will be reached at 0.43 eV above the conduction band minimum, in a good agreement with its experimental value of 0.4 eV. [112] We have also studied

hydrogen substitutional on an oxygen site, which acts as a shallow donor, too. Once hydrogen substitutes the oxygen vacancy, it is more stable than its interstitial form and it makes a multicenter bond with its Cd neighbors. This indicates that if the conductivity in CdO is dependent on the oxygen pressure, not only oxygen vacancies can be responsible for the unintentional n-type conductivity, but also substitutional hydrogen can contribute. Comparing our results with similar study (using HSE06 functional for the band gap correction) [115] shows that for donor-like defects our less computationally expensive extrapolation technique yields results in good agreement with the HSE ones. Therefore the extrapolation technique can be used to predict the shallow or deep character of a donor-like defect.

Chapter 5

Group III Elements (Al, Ga, In) Doped in ZnO

5.1 Introduction

Doped ZnO is an alternative to traditional Sn-doped In_2O_3 in several applications, due to its optical and electrical properties [127], its high chemical and mechanical stability, and its abundance and non-toxicity [128]. When doped with Al, Ga or In, ZnO thin films can be highly conductive (resistivity reduced to 2-4$\times 10^{-4}\,\Omega$ cm), and have very good optical transmittance (more than 80%) in the visible range [129, 130, 131, 132, 133].

First-principles investigations of native point defects [96] and hydrogen impurities [105] in ZnO have been performed previously using standard density functional approaches. More recently, hybrid functional [134, 135, 108] as well as screened exchange [136] and *GW* based [109] approaches have been used to study intrinsic defects in ZnO. However, to our knowledge, no such studies have been carried out yet on Al, Ga, and In-doped ZnO.

In this chapter, we consider Al, Ga, and In-doped ZnO. After applying a band gap correction, we do a defect study on these systems. For a band gap correction, we use both an extrapolation method and a hybrid functional scheme and we make a comparison between these two approaches.

The results of this chapter were published as: R. Saniz, Y. Xu, M. Matsubara, M. N. Amini, H. Dixit, D. Lamoen, and B. Partoens, Journal of Physics and Chemistry of Solids **74** 45−50 (2013)

5.2 Methods

5.2.1 Calculation details

We perform first-principles calculations using density functional theory (DFT) within the local density approximation (LDA), the LDA+U approach, and the screened hybrid functional of HSE06 [60] (with 37.5% mixing of Hartree-Fock exchange), as implemented in the Vienna ab initio simulation package [66, 116]. Electron-ion interactions are treated using projector augmented wave potentials [67, 68, 65]. The Zn $3d\,4s$, Al $3s\,3p$, Ga $3d\,4s\,4p$, and In $4d\,5s\,5p$ states were treated as valence states. The crystallographic parameters for ZnO in the ideal wurtzite structure, which is its ground state phase, were calculated to be $a = 3.22$ Å, and c/a=1.602 with an internal parameter of $u = 0.381$. These compare very well with the experimental values of $a = 3.25$ Å, and c/a=1.603 and $u = 0.382$ [137].

To model the behavior of an impurity in ZnO, we used a $3\times3\times2$ supercell containing 72 atoms, corresponding to a doping concentration of 0.93, 2.38, 3.85 wt % for Al, Ga, In, respectively. This corresponds to a defect concentration of $1.16 \times 10^{21} cm^{-3}$ (or 1.41 at.%). These rather heavy dopings (not the dilute limit) are well within the experimental range of doping concentrations (about $1 \sim 5$ wt %) considered for ZnO-based TCOs [129, 132, 138, 139]. In all impurity-doped calculations, the atomic positions were relaxed (keeping the supercell lattice parameters constant). We considered substitutional impurity at one of the Zn sites within the 72-atom supercell. Convergence with respect to **k** points and energy cutoff was checked. The electronic wave functions were expanded in plane waves up to a kinetic energy cutoff of 400 eV and the convergence with respect to self-consistent iterations was assumed when the total energy difference between cycles was less than 10^{-4} eV, and the geometry relaxation tolerance was better than 0.01 eV/Å. For the Brillouin-zone integrations, a $4 \times 4 \times 3$ Monkhorst-Pack **k**-point mesh [63] was found to be sufficient for an impurity-doped 72-atom supercell.

5.2.2 Defect formation energies

The formation energy of a point defect or impurity is a key quantity, playing a central role in determining its equilibrium concentration. As it is discussed before, the formation energy of a defect or impurity in different charge states is defined with Eq.(3.9).

The chemical potentials for the atoms depend on the experimental growth conditions. For zinc and oxygen, we assume the bounds imposed by the formation of ZnO. Extreme O-rich conditions place an upper limit $\mu_O = \mu_{O[O_2]}$

to the oxygen chemical potential. The zinc chemical potential is similarly subject to an upper bound: under extreme Zn-rich conditions, $\mu_{\mathrm{Zn}} = \mu_{\mathrm{Zn[bulk]}}$. To find lower bounds, the energy per formula unit of bulk ZnO can be expressed as

$$E[\mathrm{ZnO}] = \mu_{\mathrm{Zn[bulk]}} + \mu_{\mathrm{O[O_2]}} + \Delta H_f(\mathrm{ZnO}) = \mu_{\mathrm{Zn}} + \mu_{\mathrm{O}}, \tag{5.1}$$

where $\Delta H_f(\mathrm{ZnO})$ is the enthalpy of formation of ZnO. Thus, for instance, the lower limit on the zinc chemical potential is $\mu_{\mathrm{Zn}}^{\mathrm{min}} = \mu_{\mathrm{Zn[bulk]}} + \Delta H_f(\mathrm{ZnO})$. This corresponds to extreme O-rich conditions, with $\mu_{\mathrm{O[O_2]}} = \frac{1}{2}E[\mathrm{O_2}]$. For the dopants chemical potentials, μ_{X} (X=Al, Ga, or In), the upper limit of the chemical potential is given by the elemental bulk phase. However, in O-rich conditions μ_{X} is limited by the formation of $\mathrm{X_2O_3}$, i.e.,

$$2\mu_{\mathrm{X[bulk]}} + 3\mu_{\mathrm{O[O_2]}} + \Delta H_f(\mathrm{X_2O_3}) = 2\mu_{\mathrm{X}} + 3\mu_{\mathrm{O}}. \tag{5.2}$$

$\Delta H_f(\mathrm{X_2O_3})$ is the formation energy of $\mathrm{X_2O_3}$. Thus, for instance, in O-rich conditions the chemical potential for Al decreases to $\mu_{\mathrm{Al}} = \mu_{\mathrm{Al[bulk]}} + \Delta H_f(\mathrm{X_2O_3})/2$.

Of great importance in the study of impurities, which we aim to determine, are the defect transition energy levels, $\epsilon(q/q')$. These are defined as the value of the Fermi level where the formation energy of q equals that of q'. The meaning of this level is that for Fermi-level positions below $\epsilon(q/q')$, charge state q is stable, while for Fermi-level positions above $\epsilon(q/q')$, charge state q' is stable.

5.3 Results and discussion

5.3.1 Electronic structure

The band structure for undoped ZnO is given in Fig. 5.1(a). There is good agreement with previous calculations for ZnO [140]. A highly dispersive band at the bottom of the conduction band can be observed. The calculated band gap is 0.72 eV for undoped ZnO, close to the value found in previous calculations [140, 86]. The band gap underestimation with respect to the experimental value (3.43 eV), is a well known LDA artefact. We address this problem in the following subsection. With one Zn atom substituted by Al, Ga or In, the calculated band structures are given in Figs. 5.1(b)-(d). The band structures obtained in Ref. [139] with similar supercells are consistent with ours.

Doping with Al affects very little the band structure of ZnO, although a small splitting of degenerate states in the conduction bands can be observed.

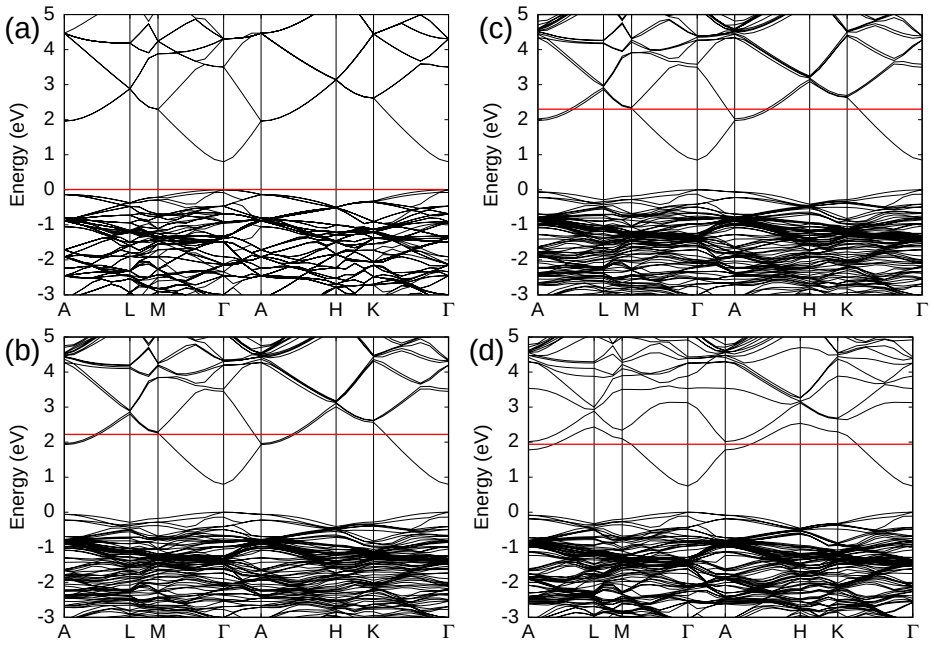

Figure 5.1: Band structure for ZnO in a supercell geometry (a) and Al(b)-, Ga(c)-, In(d)-doped ZnO. For pure ZnO(a), the VBM is set at 0 eV. The red solid lines in (b), (c) and (d) represent the Fermi energy in each figure.

The impurity band is completely hybridized with the host bands. However, an analysis of the conduction band minimum calculating the projected weights of the Kohn-Sham wavefunction shows that it consists predominantly of Zn-4*s* states. The case of Ga doping is largely similar, with the difference that the splitting in the lowest conduction band is somewhat larger and that there is a band gap narrowing of 10% (to 0.65 eV). In the case of In doping, the band structure shows a more significant modification. The lowest conduction band splitting is stronger and the bandgap in this case is now 0.57 eV, i.e., 21% narrower. But, again, the projected weights of the Kohn-Sham wavefunction shows that the conduction band minimum is dominated by Zn-4*s* states. The band gap reduction with respect to ZnO is a result of electron-electron exchange and electron-impurity ion interactions [141, 139]. In Ref. [139], in particular, it is shown that the interaction between dopant states and ZnO conduction band states lead to an increasing splitting of the lowest conduction band with cation size, and a consequent tendency of the fundamental gap to decrease. In Fig. 5.1 one can also see that in these systems there is a non-negligible filling of the lowest conduction band by the

dopant electrons. This gives rise to the Burstein-Moss energy shift observed in optical experiments [139].

Note that in the band structures in Fig. 5.1 for the doped cases dopant concentrations are to high to create flat defect levels (see discussion in section 3.3.3 on the limitations of the ab initio approach). However since the total energies are converged, the formation energies for the dilute limit can be obtained, and the shallow or deep character of the defects can be determined and is done in the next section.

5.3.2 Formation energies and corrections

As mentioned before, the LDA seriously underestimates band gaps. This has a repercussion on the values of the formation energies, and the relevance to experiment of the transition energy levels predicted by the LDA is highly uncertain. In the case of ZnO, the error is aggravated because the LDA underestimates the binding energy of the Zn d electrons. To compare the calculated transition levels with the experimental results, it is necessary to add corrections. As mentioned in chapter 3, several approaches have been proposed to improve this problem. The extrapolation method based on the LDA+U approximation [86] is more recent and, given its success, is one of the methods which we use. Here we briefly recall the main idea. The method is based on the calculation of the formation energies for the different charge states both with the LDA and LDA+U exchange-correlation functionals. The latter, by correcting the position of the Zn d levels, lowers the valence band maximum and pushes upward to conduction band minimum. Thus, it partially corrects the band gap error in pure ZnO, opening it from E_g^{LDA} to $E_g^{\mathrm{LDA}+U}$. Regarding the transition energy levels, the predicted values suffer from the band gap problem and, therefore, need to be corrected. This is done as follows. The opening of the gap in the LDA+U case leads to an upward shift from $\epsilon(q/q')^{\mathrm{LDA}}$ to $\epsilon(q/q')^{\mathrm{LDA}+U}$. Proceeding now with a linear extrapolation, the corrected transition levels correspond to an opening of the gap up to its experimental value. From these one can easily determine the corrected formation energies for different Fermi levels. This method was used with success to the study of native defects in ZnO [86], hydrogen impurities and native defects in CdO [142], and hydrogen doping in In_2O_3 [107].

In Fig. 5.2 we present the formation energies for Al_{Zn}, Ga_{Zn}, and In_{Zn} in the $1+, 0$, and $1-$ charge states. Figures 5.2(a), (c), and (e) present the PAW based LDA (PAW-LDA) results. Figures 5.2(b), (d), and (f) present the corresponding corrected results following the LDA+U plus extrapolation method (PAW-LDA+U+X) (a value of $U = 4.7$ eV is used for Zn (see Ref. [49])). The formation energies presented correspond to Zn-rich condi-

tions. It is clear that the corrected transition levels obtained are all well in the conduction band.

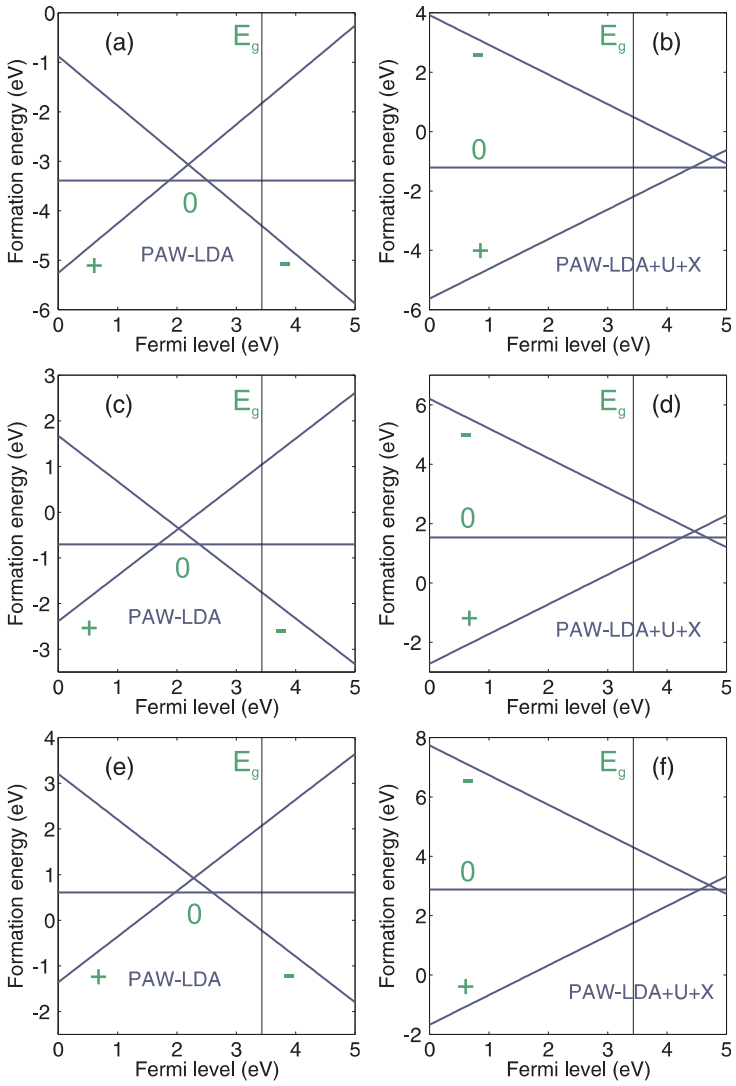

Figure 5.2: The formation energies obtained with the PAW-LDA and PAW-LDA+U+X methods. Figs. 5.2(a) and 5.2(b) are for Al_{Zn}, without and with correction schemes, respectively. Similarly, Figs. 5.2(c) and 5.2(d) correspond to Ga_{Zn}, and Figs. 5.2(e) and 5.2(f) to In_{Zn}. The calculations are for Zn rich conditions. The vertical line indicates the experimental gap value.

A computational scheme that in principle does not suffer from the band gap problem is the hybrid functional approach of Heyd-Scuseria-Ernzerhof

(HSE) [60, 100]. For a more complete study and comparison, we also carry out the calculation of the formation energies, in the Al case, using HSE functional. This method has been shown to yield rather accurate band gaps in semiconductors and insulators and has been used recently with success to study defect levels in ZnO [135].

In Fig. 5.3, we show the HSE formation energies (PAW-HSE) for Al_{Zn} in the 1+, 0, and 1− charge states, together with the results from the LDA+U and extrapolations method (PAW-LDA+U+X). Figure 5.3 clearly shows that the extrapolation scheme indeed predicts reliable transition levels comparing to the HSE method. This comparison lends further support to the claim in Ref. [103] regarding the reliability of the LDA+U and extrapolation scheme to calculate the transition levels in defect systems. The formation energies obtained as a function of Fermi level, under Zn-rich and O-rich conditions, show that in all cases the impurities considered act as shallow donors.

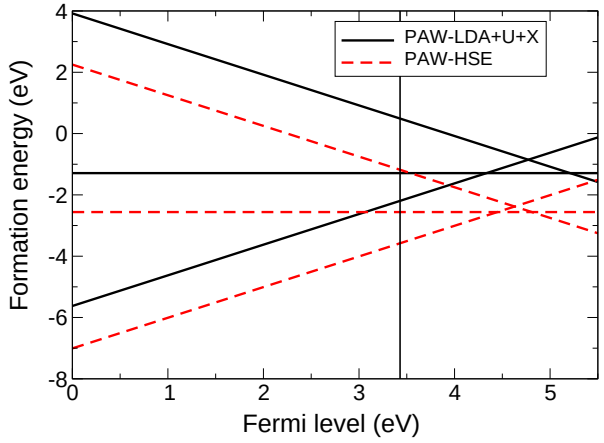

Figure 5.3: Comparison of the formation energies for different charge states in the case of Al_{Zn} using the extrapolation method (PAW-LDA+U+X) and the HSE hybrid functional (PAW-HSE). The thermodynamic transition levels obtained in both approaches are seen to be very close to each other.

We can further see that, in the case of substitutional impurities, the formation energies for Al impurities are clearly lower than those for Ga and In in Zn-rich conditions. In O-rich conditions, on the other hand, the formation energy for substitutional Ga is lower than for Al, albeit only marginally, and both are moderately lower than in the case of In. Thus in the former case, doping with Al can be expected to lead to a comparatively higher carrier concentration [9], while in the latter case Ga and Al should have

similar concentrations, but higher than in the case of In. The difference in relative positions of the dopant formation energies in Zn-rich and O-rich conditions is essentially due to the difference in enthalpies of formation of the different dopant oxides, which strongly modifies the dopant chemical potential (see Eq. (5.2) and discussion thereafter). Note also that, overall, the formation energies in O-rich conditions are clearly higher than in Zn-rich conditions. This indicates that the latter conditions will lead to higher doping concentrations compared to the former. We keep our discussion here at a qualitative level, because we do not claim accuracy in the absolute values of the formation energies we obtain with the applied methods.

5.4 Conclusion

To summarize, we have studied by first principles calculations the electronic structure and formation energies of group III elements (Al, Ga, In) doped in ZnO. It is shown that all three dopants are shallow donors, and that the preferred charge state is 1+ in all cases. To overcome the LDA band gap error in the calculation of formation energies, we have applied two correction approaches: an extrapolation scheme based on the LDA+U method and the application of the hybrid HSE functional. A comparison shows that the extrapolation method is able to predict the transition levels correctly, but not the formation energies. An advantage of such extrapolation technique is the faster convergency of the total energies, but it works only in presence of localized d electrons in the system.

Chapter 6

Hydrogen Passivation in (Al,Ga,In)-Doped ZnO

6.1 Introduction

The incorporation of hydrogen in a material can strongly affect its electronic properties. Furthermore, its behavior depends on the host into which it is introduced. Mostly, interstitial hydrogen is amphoteric, i.e. it can act either as a donor (H_i^+) or an acceptor (H_i^-) [143]. Which of these two prevails depends on the Fermi level: it acts as a donor in p-type materials and as an acceptor in n-type materials. Consequently, it counteracts the conductivity caused by extrinsic dopants. It is important to realize that this passivation of extrinsic dopants by hydrogen is not caused by the formation of a neutral complex. The formation of such a neutral complex may just be the consequence after compensation, i.e. after the trapping of a free hole or electron by hydrogen. Afterwards, the positively charged H and negatively charged acceptor, or negatively charged H and positively charged donor attract and may form a neutral complex.

In ZnO however, the behavior of hydrogen is not amphoteric [143]. Nominally undoped ZnO shows n-type conductivity and it was first predicted by first-principles calculations based on density functional theory [105], and later experimentally verified [144, 145], that interstitial hydrogen acts as a shallow donor in ZnO and can cause this n-type behavior.

ZnO is a wide band gap (∼3.4 eV at room temperature [146]) semiconductor with many possibilities for technological applications as a transparent

The results of this chapter were published as: M. N. Amini, M. Matsubara, R. Saniz, D. Lamoen, and B. Partoens, Physical Review B **86**, 165207 (2012)

conductor in solar cells [147], flat panel displays [7], etc. It is well-known that the electronic conductivity of ZnO can be dramatically improved by doping it with group III elements Al, Ga or In [148]. This makes ZnO an alternative for indium tin oxide, which shows highest conductivity among transparent conducting oxides but is less abundant and therefore more expensive. It is then also important to know what limits the conductivity of ZnO doped by Al, Ga or In. Properties such as formation energy, energy band structure and equilibrium geometry of Al, Ga and In doped ZnO were studied systematically and it was shown that all three dopants are indeed shallow donors and that they possess the intrinsic qualities to be good n-type transparent conducting oxides [97].

As the concentration becomes high, the interaction between defects becomes unavoidable. Because it is very difficult to remove hydrogen from the crystal growth environment, it is then also natural to ask what the influence is of interstitial hydrogen on Al, Ga or In doped ZnO. Recently a number of experiments were reported where both H and group III elements are co-doped into ZnO. It was shown that the conductivity of ZnO co-doped with H and group III elements is better than that doped with group III elements up to certain amount of H inclusion [149, 150, 151, 152, 153].

Apart from single hydrogen dopants, the influence of hydrogen on doped ZnO structures has been studied before by first principles calculations. It was found that hydrogen passivates nitrogen dopants [154], silver dopants [155] and Zn vacancies [156] in ZnO, and forms complexes. This is not very surprising, as in all these cases, hydrogen, which is a (positive) shallow donor, is attracted to a (negative) acceptor impurity. This is not unique to hydrogen. Also donor-like As_{Zn} and acceptor-like V_{Zn} attract each other and form a complex in As doped ZnO [157]. Recently, also the attractive interaction between two donor impurities was predicted by first principles studies in ZnO, namely the deep donor V_O (the oxygen vacancy) and the shallow donor Zn_i [158] (the Zn interstitial).

In this chapter, we consider the two shallow donors interstitial hydrogen H_i and substitutional X_{Zn} with X = Al, Ga or In.

6.2 Methods

We performed density functional theory calculations as implemented in the Vienna ab initio simulation package (VASP) code [116, 67]. In order to examine interactions between defects, a large supercell consisting of 192 atoms was

considered [1]. A single Al, Ga or In atom was chosen to substitute a Zn atom, while for the H atom, an extensive number of positions around the group III element were considered. For all these configurations the formation energies for different charge states were calculated using the method of Ref. [86], which combines local-density approximation (LDA) and LDA+U [49] calculations with an extrapolation scheme to overcome the band-gap problem (we have chosen U = 4.7 eV, as obtained in Ref. [49]). This method was recently confirmed to give reliable results for the transition energies between different charge states of the impurity, both for ZnO with interstitial H [103] as for ZnO doped with a group III element [97] (discussed in chapter 5), by comparing the results with hybrid functional calculations.

6.3 Results and discussion

As we will compare the formation energies of the defect complexes with the corresponding isolated defects, we first considered the individual interstitial hydrogen H_i and the substitutional X_{Zn} (with X = Al, Ga, or In) defects. As expected, the +1 charge state of the substitutional X_{Zn} defect is the ground state for all values of the Fermi energy in the band gap. The results are presented in chapter 5 [97]. For the interstitial hydrogen H_i defect, different positions are possible. Our calculations confirm that the bond center position (labeled $BC_{\|}$ according to Ref. [105]), with the H atom positioned between a Zn and an O atom is the preferential interstitial position. Furthermore, our formation energies are in agreement with the results presented in Ref. [102].

Let us now consider the defect complexes. As for the isolated interstitial hydrogen H_i defect, we considered many different positions, and we find that, for all charge states, the lowest formation energy is obtained when the H atom is located close to the octahedral interstitial position next to an Al, Ga or In atom (in the notation defined in Ref. [105], this position can be called the antibonding $AB_{Al,\perp}$ configuration). Note that this position differs from the isolated H_i defect. We can now compare the formation energies for two noninteracting impurities, obtained by adding the formation energy of a single interstitial H atom (H_i) at the $BC_{\|}$ position and a single Al, Ga, or In dopant in ZnO (X_{Zn}), with the formation energy of the defect complexes, with the H atom at the $AB_{Al,\perp}$ position. The results are shown in Figs. 6.1, 6.2 and 6.3 for the codoping cases H-Al, H-Ga, and H-In, respectively.

[1] Our supercell consists of 192 atoms ($4\times4\times3$ unit cells). Wave functions are expanded with plane wave basis sets up to a cutoff energy of 400 eV and the Brillouin zone is sampled with the k-point grids of $2 \times 2 \times 2$. Optimization of ionic positions is allowed to proceed until the largest force component is less than 0.01 eV/Å.

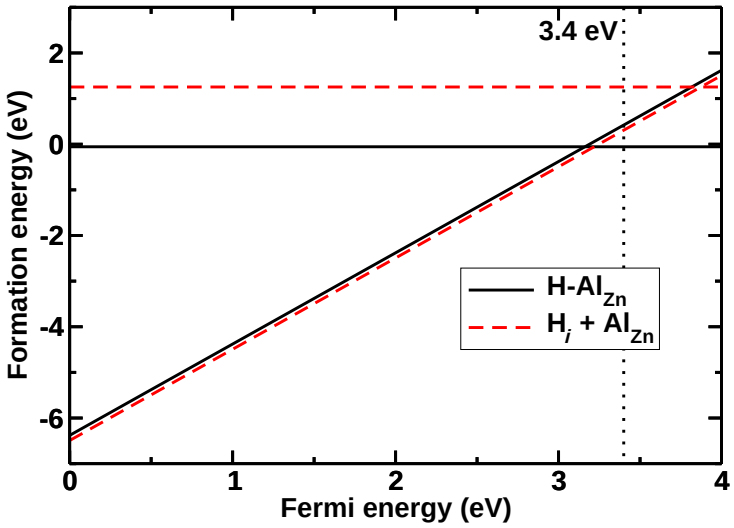

Figure 6.1: Formation energy as function of Fermi energy for the $H - Al_{Zn}$ complex (full black curve) and for two noninteracting interstitial hydrogen H_i and substitutional Al_{Zn} impurities (dashed red curve), in the oxygen poor limit.

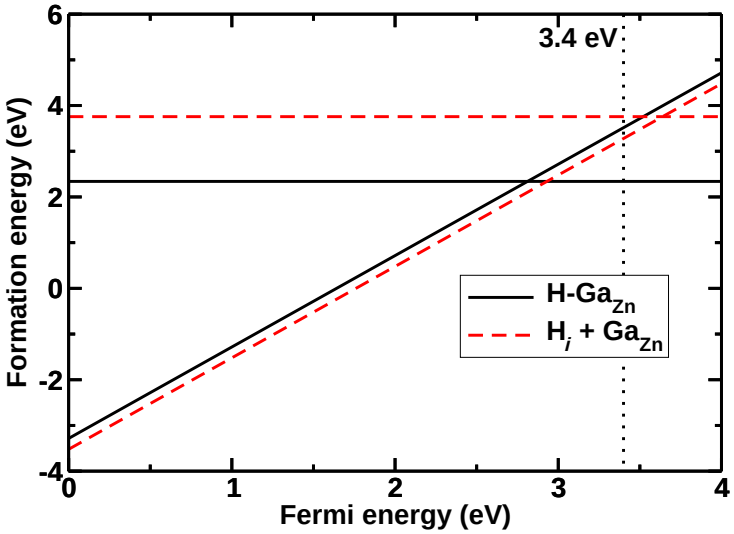

Figure 6.2: As Fig. 6.1, but for Ga-H co-doped ZnO.

The shown curves are for the oxygen poor limit. For the oxygen rich limit, all curves shift down with 3.43 eV. This choice has no influence on our conclusions, as they are only based on the crossing points between the

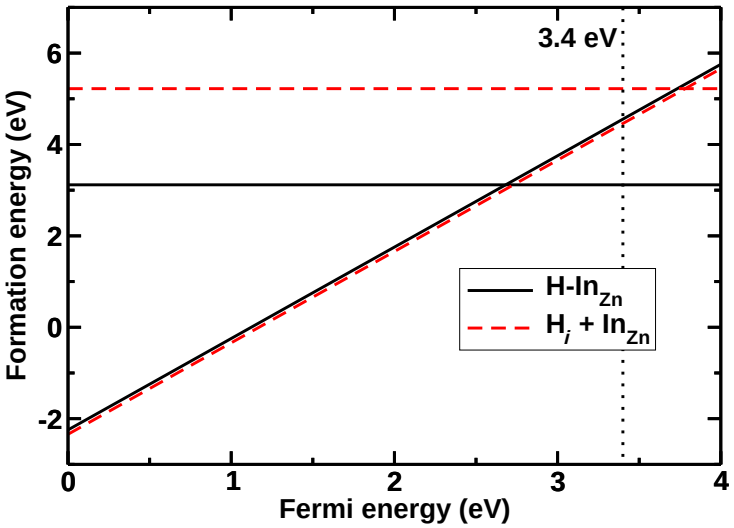

Figure 6.3: As Fig. 6.1, but for In-H co-doped ZnO.

formation energy curves for different charge states. As both H and (Al, Ga or In) can give away a single electron, the +2 charge state is the ground state for small values of the Fermi energy. (The +1 case is not shown, as it never becomes the ground state.) It is clear that the case of two non-interacting, thus infinitely separated, impurities has the lowest formation energy. In this +2 charge state, both shallow donors repel each other. More importantly, however, for Fermi energy values close to the band gap of 3.4 eV, the neutral H-(Al,Ga,In) complex has the lowest formation energy. Furthermore, the crossing between the non-interacting charge case +2 and the neutral complex occurs in the band gap, i.e. a deep level is formed. This crossing occurs at 0.18 eV, 0.47 eV and 0.67 eV below the bottom of the conduction band for Al-H, Ga-H, and In-H, respectively. This is a consequence of the large decrease in formation energy of the neutral complex in comparison to the formation energy of two non-interacting neutral impurities: 1.31 eV for Al-H, 1.42 eV for Ga-H, and 2.11 eV for In-H. As a consequence, the shallow donor H binds to and passivates the shallow donor (Al, Ga or In).

The formation of a deep level is also clear from the density of states (DOS). As an example, the DOS for the Al-H co-doped case obtained within the LDA approximation is shown in Fig. 6.4. The neutral complex is considered in its ground state configuration. Comparing Figs. 6.4(a) and (b) for the pure ZnO crystal and the co-doped case, a sharp peak appears in the ZnO band gap. From the projected (local) DOS plots on H (Fig. 6.4(c)) and Al (Fig. 6.4(d)) we observe that this deep donor level has H s and Al p char-

acter. While an individual interstitial H_i and a substitutional Al_{Zn} atom in ZnO have both a defect level in the conduction band with these characters, a bonding level is formed in the case they form a complex, which lowers the energy to a value in the band gap.

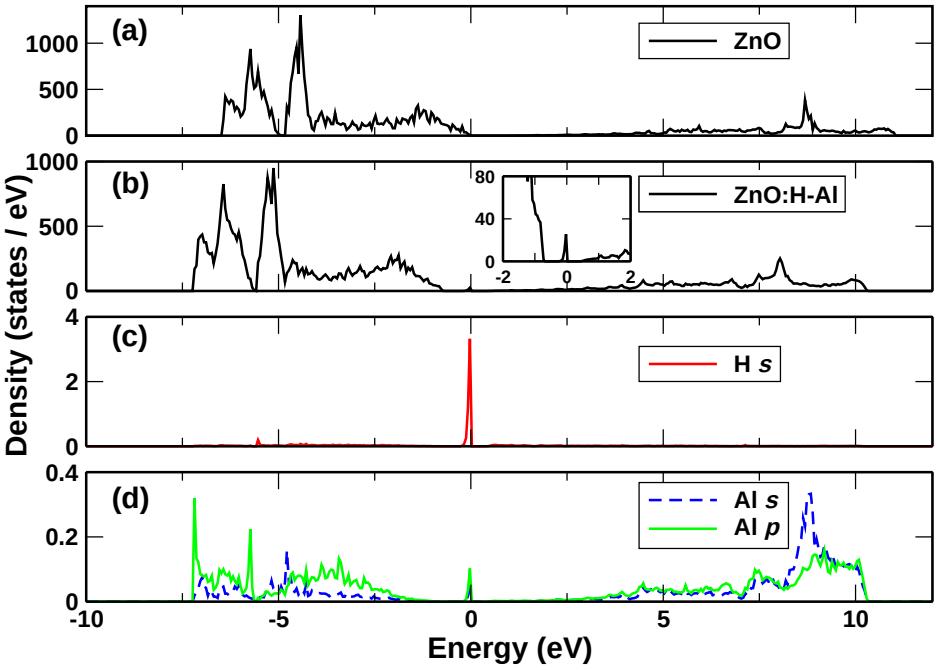

Figure 6.4: Calculated DOS, with zero energy taken at the Fermi level: (a) total DOS for the pure ZnO crystal; (b) total DOS for the Al-H co-doped ZnO, the inset is a zoom around the Fermi level; (c) projected (local) DOS on the H site; (d) projected (local) DOS on Al site.

To gain a better understanding of the physics behind this finding, we considered the bond length in the neutral complex. The bond between both shallow donors is clearly reflected in the interatomic distances. In the neutral case, the equilibrium distance between the interstitial H atom and the substitutional group III atom is 1.86 Å for the Al case, 1.77 Å for the Ga case and 1.87 Å for the In case. However, in the +2 case, these distances increase till close to 3.15 Å for all three cases, showing a clear repulsion. As an example, for the Al-H co-doped ZnO, the structure of the neutral Al-H complex is shown in Fig. 6.5(a) and (b), and for the repelling +2 case in Fig. 6.5(c) and (d). It is also interesting to compare these bond lengths in the case of the neutral complex with those of the corresponding molecular species AlH, GaH and InH, which are 1.65 Å, 1.66 Å, and 1.84 Å [159]. The

Al-H and Ga-H bond length are thus longer in comparison to the length in the molecular species, especially in the Al-H case, while the In-H bond length is much closer to the molecular structure InH. This shows that there is indeed a bond in the neutral H-X complex, although weaker than in the molecular case.

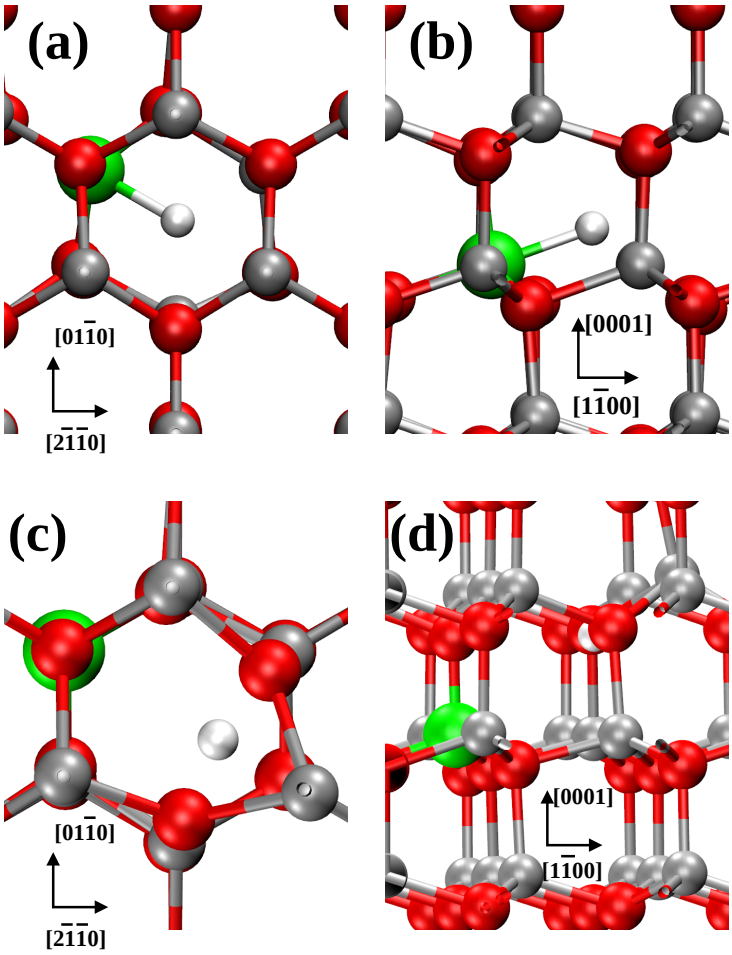

Figure 6.5: (a) and (b) The Al-H neutral complex. (c) and (d) The +2 charge case of the Al-H complex. Red atom is Zn, grey atom is O, green atom is Al, white atom is H. These figures are generated by VMD version 1.8.7 [160].

To support this view and to propose an experimental way to detect these complexes, we also studied a vibrational property. The microscopic geometry for hydrogen in semiconductors is usually determined through observation of the infrared spectrum of the related local vibrational mode. In order to facilitate the experimental observation of the H-(Al, Ga, In) complex, we

calculate the H-X stretching mode. As the H atom is so light we also take into account the anharmonic effect. Therefore the potential curve is fitted by the following formula [161]

$$V(x) = \frac{k}{2}x^2 + \alpha x^3 + \beta x^4. \tag{6.1}$$

We have taken displacements up to ± 30 % of the X-H bond length along the bond direction. By applying perturbation theory to the one-dimensional Schrödinger equation an approximated analytical solution in the case of the anharmonic potential [eq. (6.1)] is given by [162]

$$\omega = \omega_{\mathrm{H}} + \Delta\omega_{\mathrm{A}} = \sqrt{\frac{k}{\mu}} - 3\frac{\hbar}{\mu}\left[\frac{5}{2}\left(\frac{\alpha}{k}\right)^2 - \frac{\beta}{k}\right], \tag{6.2}$$

where ω is the frequency of the mode, ω_H and $\Delta\omega_A$ its harmonic and anharmonic contribution, and μ is the reduced mass. The obtained results for the frequency of the local vibrational modes are shown in Table (5.1). Again we can compare with the corresponding frequencies of the molecular species. These results are also included in Table (5.1) under ω_{mol} (taken from Ref. [159]). Note that the obtained frequencies for the complex are smaller than in their molecular equivalents. The difference is most pronounced for Al-H, and the smallest for In-H. The larger the difference, the weaker the bond is in the complex in comparison with the molecular equivalent. This trend is consistent with the trend that was observed for the bond lengths. This then also explains why the defect level of the complex is deepest in the In-H case.

Table 6.1: Calculated harmonic frequencies (ω_H), anharmonic contributions (ω_A) and total frequencies (ω) of the local vibrational mode of the X-H complex, and the corresponding frequency (ω_{mol}) in the corresponding molecular structure, taken from Ref. [159]. All frequencies are expressed in cm^{-1}.

Complex	ω_H	$\Delta\omega_A$	ω	ω_{mol} [159]
H-Al	1266	-54	1212	1682
H-Ga	1265	-64	1201	1604
H-In	1350	-71	1280	1475

6.4 Conclusion

To summarize, we have studied by first principles calculations the co-doping of ZnO with hydrogen and a group III element (Al, Ga, or In). While these impurities are known to be shallow donors in ZnO, and are therefore expected to repel each other, we show on the contrary that they attract each other, resulting in a neutral complex which forms a deep level. Hydrogen thus passivates the group III impurity in ZnO, which puts a limit on its n-type conductivity. In semiconductors in which hydrogen shows amphoteric behavior, passivation of a shallow impurity does not mean that a complex is formed, the formation of such a complex may just be a consequence of the passivation. In ZnO however, in which hydrogen acts as a shallow donor, it is the pairing between hydrogen and the substitutional shallow donor into a neutral complex that realizes the passivation.

Chapter 7

Origin of p-type Conductivity in ZnM_2O_4 (M=Co, Rh, Ir)

7.1 Introduction

As it is discussed in chapter 1, TCOs constitute a unique class of materials which combine two physical properties together - high optical transparency and high electrical conductivity. Most of the TCO materials exhibit n-type conductivity and development of an efficient p-type TCO is one of the global materials challenges [2].

Delafossite $CuXO_2$ (X=Al, Ga and In) oxides were a first group of p-type materials which were studied since 1997 [163]. These studies were followed by considering the possibility of using ZnM_2O_4 (M=Co, Rh, Ir) spinel structures as p-type TCOs [164, 165, 166]. Experimentally one has shown that polycrystalline samples of ZnM_2O_4 spinels exhibit p-type conductivity. The reported electrical conductivities without doping the structures are 0.39 S cm^{-1}, 2.75 S cm^{-1} and 3.39 S cm^{-1} for $ZnCo_2O_4$, $ZnRh_2O_4$ and $ZnIr_2O_4$ respectively, all at room temperature [166]. The conductivity increases $\sim$ 7-10 times when Co is replaced by Rh or Ir. The electronic band structures of these ternary spinels are, however, very similar. Hence the reasons for enhanced conductivity while going from Co to Rh or Ir are not apparent and formation energies of native defects need to be studied.

In order to study defect formation energies, a good understanding of the bulk electronic properties is necessary, especially the band gap. However, scattered experimental results are presented in the literature. The experi-

The results of this chapter were published as: M. N. Amini, H. Dixit, R. Saniz, D. Lamoen, and B. Partoens, Phys. Chem. Chem. Phys., 2014, DOI: 10.1039/C3CP53926A.

mental study of Dekkers *et al.* [166] assumed that the band gap and transparency in these spinels originate from the ligand field splitting between d orbitals of the M^{3+} elements. The d orbitals (filled with 6 electrons) in these structures split into three t_{2g} and two e_g orbitals due to the octahedral arrangement of the M ion and these levels create the band gap. In this reference, the band gaps of $ZnCo_2O_4$, $ZnRh_2O_4$ and $ZnIr_2O_4$ are found to be 2.26 eV, 2.74 eV and 2.97 eV, respectively. It is known that ligand field splitting increases with increasing atomic number, leading to the following band gap ordering: $E_g^{ZnCo_2O_4} < E_g^{ZnRh_2O_4} < E_g^{ZnIr_2O_4}$. However, a different trend is observed in other experimental reports. Refs. [164, 165, 167, 168] indicate a decrease in the band gap with increasing the atomic number from Co to Rh. Theoretical studies based on LDA, LDA+U [167], GGA [168], the advanced hybrid exchange-correlation functional HSE06 [169] and the Tran-Blaha modified Becke-Johnson potential (TB-MBJ) [170] also find this trend: the band gap decreases with heavier cation substitution in ZnM_2O_4 spinels. The HSE06 and the TB-MBJ results also seem to overestimate the band gaps. Therefore a re-examination of the experimental results was proposed in some theoretical works [169, 170]. Moreover these studies also indicate a lack of dispersion for the valence band maximum (VBM) resulting in a heavy hole mass.

Defects play an important role in controlling the electronic properties in TCOs along with the dopant - which is the main source of conductivity in an otherwise insulating oxide. The unintentional conductivity observed in TCO materials is often attributed to the presence of native defects. Recently, the formation energy of native defects in many spinel oxides including $ZnCo_2O_4$ and $ZnRh_2O_4$ has been calculated using the GGA+U formalism [171, 172, 173, 174]. Antisite defects, in which either type of cation is substituted by the other, are found to be the leading cause of electrical conductivity in the spinel structure. An indication of how easily n-type or p-type conductivity can be obtained by considering the position of the band edges with respect to the vacuum level [175]. Materials with a high valence band are more likely to be doped p-type. However, it is not known how the band edges compare to the vacuum level in these spinels.

Motivated by these observations, we address the following topics in this work. First we calculate the bulk electronic structure properties to compare with the available literature. To contribute to the discussion on the re-examination of the experimental band gaps and the validity of the HSE06 functional to describe these spinel structures, we calculate their electronic structure also within the GW approach. Next we want to understand why these spinels are p-dopable by examining their band alignment relative to the well-known TCO ZnO. And finally we calculate explicitly the formation en-

ergies of native acceptor defects to understand which defects are responsible for the observed p-type behaviour, and why the p-type behaviour improves with cation size among the three spinels $ZnCo_2O_4$, $ZnRh_2O_4$ and $ZnIr_2O_4$. It is known that the formation energy calculations based on GGA suffer from the band gap error. Motivated by the agreement between the HSE06 and GW results for the bulk systems, we rely in this work on the HSE06 functional [60], which is considered to be the state-of-the-art method for first-principles defect calculations [103]. We will compare our results and point out the differences with the results obtained with the GGA+U method of Ref. [173].

We also calculate the range of accessible chemical potentials and study the stability of ternary spinels with respect to the stable binary oxides. It has been observed that the antisite defect is the most stable defect and we also analyze the atomic geometries of defects to understand why it is the leading cause of disorder. Further, we calculate the self-trapping energy of the holes in these spinel oxides. It is known that the hole conductivity can be limited by the spatial localization of a self-trapped hole or a small polaron [176, 177, 178, 179]. Thus it is important to calculate the self-trapping energy of holes to understand whether these excess carriers are lattice-bound or not. Such a study is critical for p-type TCOs. It should also be noted that for the $ZnRh_2O_4$ spinel, analysis of the experimentally high temperature electrical properties indicated an activated mobility, indicative of small polaron conduction [167], while a theoretical study based on the DFT+U calculations predicts that the self-trapped hole is unstable [180]. Next, Hall measurements together with a re-examination of the experimental results [180] confirmed this theoretical prediction. Therefore we also address the existence of polarons within the HSE06 approach to test the capabilities of the HSE06 functional.

This chapter is further organized as follows. First the computational details are described. Then, the results obtained for structural and electronic properties along with the band alignments are discussed . Finally, we discuss the formation energies of the cation vacancies and the antisite defect under different growth conditions that can be realized in the experiments.

7.2 Computational details

We perform first-principles calculations using density functional theory (DFT) within the screened hybrid functional of HSE06 [60], as implemented in the Vienna ab initio simulation package [66, 116]. We have used 25% mixing of Hartree-Fock exchange in the HSE06 functional. Electron-ion interactions

are treated using projector augmented wave potentials [67, 68, 65]. The Zn ($4s^2 3d^{10}$), Co ($4s^1 3d^8$), Rh ($5s^1 4d^8$), Ir ($6s^1 5d^8$), and O ($2s^2 2p^6$) electrons are treated as valence electrons. Within the GW approach [181, 182], 1000 bands are used to converge the band gap for both the screening and the self-energy calculation. The defects are simulated by adding (removing) atoms to (from) a 112-atom 2×2×2 supercell. A 2×2×2 mesh of special k-points based on the Monkhorst-Pack scheme [63] is chosen for the integrations over the Brillouin zone. The electron wavefunctions are described using a plane-wave basis set with an energy cutoff of 400 eV. Note that the convergence with respect to self-consistent iterations was assumed when the total energy difference between cycles was less than 10^{-4} eV and the geometry relaxation for different charge states continued until the transition level position differences were less than 10 meV.

7.3 Structural properties

The spinel structure (space group $Fd\bar{3}m$) is characterized by the lattice parameter a and an internal parameter u. The Zn atoms are located at Wyckoff positions 8a (1/8, 1/8, 1/8) tetrahedral sites, whereas M (M=Co,Rh,Ir) atoms are located at the 16d (1/2, 1/2, 1/2) octahedral sites and the O atoms at 32e (u, u, u) of the face-centered cubic lattice. The ZnM_2O_4 spinel structure is shown schematically in Fig. 7.1. The optimized lattice constant, calculated using the HSE06 functional is in remarkably good agreement with experiment. These values are reported in Table (7.1).

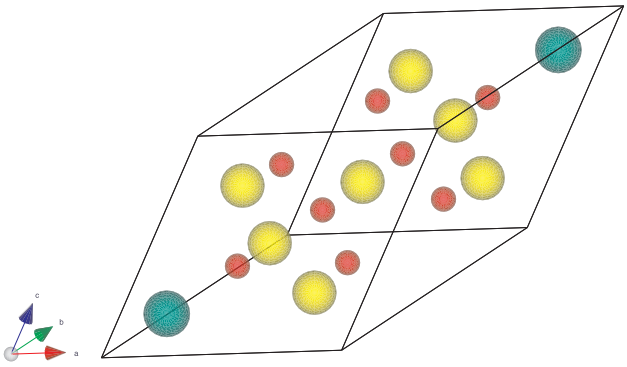

Figure 7.1: Primitive cell of the ZnM_2O_4 spinel structure: the Zn atoms in green color are tetrahedrally coordinated with the oxygen atoms shown in red and the M atom (in yellow) are octahedrally coordinated with the oxygen atoms.

Table 7.1: HSE06 optimized and experimental lattice constant (in Å) along with the optimized internal parameter (u).

Oxide	HSE	u parameter	Exp. [166]
$ZnCo_2O_4$	8.02	0.264	8.10
$ZnRh_2O_4$	8.49	0.260	8.49
$ZnIr_2O_4$	8.59	0.260	8.51

7.4 Electronic band structure and projected density of states

The electronic band structures of ZnM_2O_4 spinels calculated using the HSE06 functional are shown in Fig. 7.2. All the three spinels have an indirect band gap. The VBM for $ZnCo_2O_4$ is near W along the $W - L$ direction while it is located at the X point for both $ZnRh_2O_4$ and $ZnIr_2O_4$ spinels. The conduction band minimum (CBM) is located near X along the $\Gamma - X$ direction for both $ZnCo_2O_4$ and $ZnRh_2O_4$ structure while for $ZnIr_2O_4$ spinel it is located at the Γ point. Experimental band gap values for $ZnCo_2O_4$, $ZnRh_2O_4$, and $ZnIr_2O_4$ are 2.26, 2.74, and 2.97 eV [166] while our calculated band gap values within HSE06 (PBE) are 3.88 (0.99), 2.91 (1.07), and 2.53 (0.79) eV for $ZnCo_2O_4$, $ZnRh_2O_4$, and $ZnIr_2O_4$ respectively and all confirm the results from a theoretical electronic study of these spinels in Ref. [169]. It should be noted that all these spinels are characterized by a flat dispersion of the VBM, which results in heavy holes with large effective masses, indicating poor p-type conductivity.

The calculated total and projected density of states (PDOS) are shown in Fig. 7.3. Experimentally, the Zn 3d peaks are reported to occur at $\sim$ -8.8 eV, $\sim$ -9.2 eV and $\sim$ -9.5 eV for $ZnCo_2O_4$, $ZnRh_2O_4$ and $ZnIr_2O_4$ respectively [166]. We observe that the Zn $3d$ peaks occur at -6.8 eV, -7.8 eV and -9 eV for $ZnCo_2O_4$, $ZnRh_2O_4$ and $ZnIr_2O_4$ respectively in the band structure calculated using the HSE06 functional. The Zn d states are positioned closer to their experimental counterpart than those reported in PBE-GGA calculations [169]. As evident from PDOS, the CBM of $ZnCo_2O_4$/$ZnRh_2O_4$ spinel has a strong Co/Rh d character whereas it is made up of Ir s, Zn s and O s states in the case of $ZnIr_2O_4$ (the CBM of $ZnIr_2O_4$ is highlighted in Fig. 7.4: overlapping black, red and magenta lines for the CBM represent Ir-s, Zn-s and O-s states respectively). Also the CBM for $ZnIr_2O_4$ is located at the Γ point. This is in contrast with the claim of Dekkers *et. al.* [166] that the CBM is made up of Ir $5d$ states as predicted by the ligand field theory but is in good agreement with an earlier theoretical report [169]. Fur-

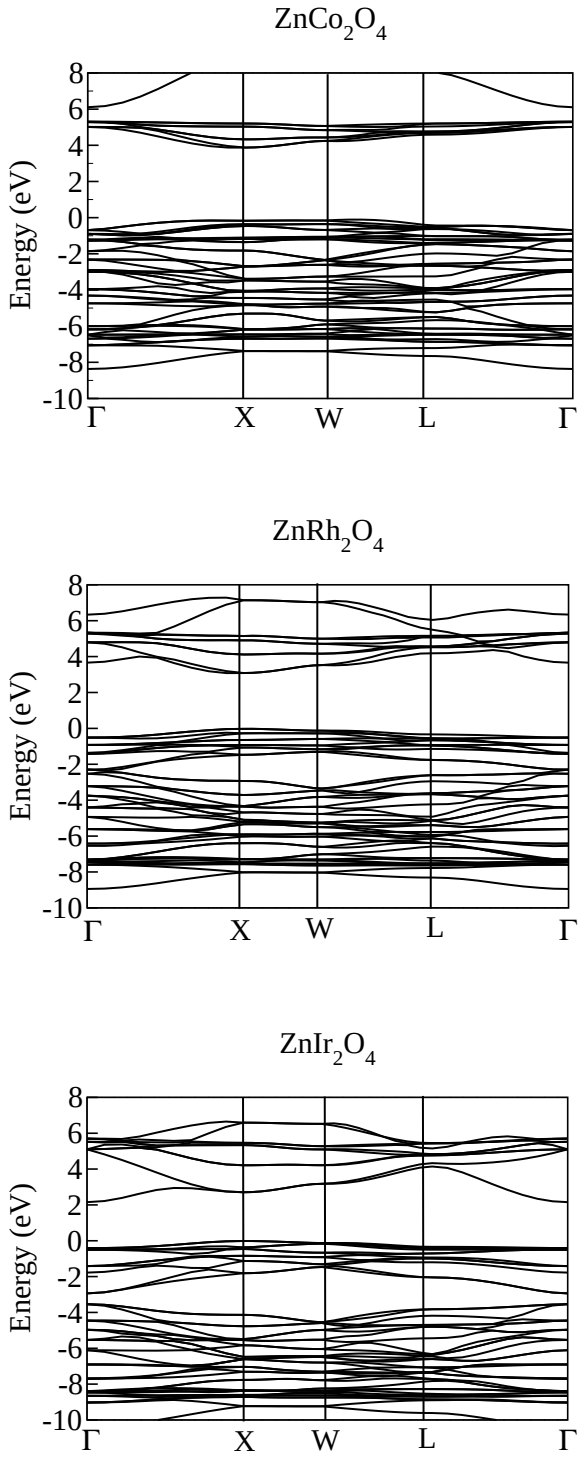

Figure 7.2: Electronic band structure calculated using HSE06.

H

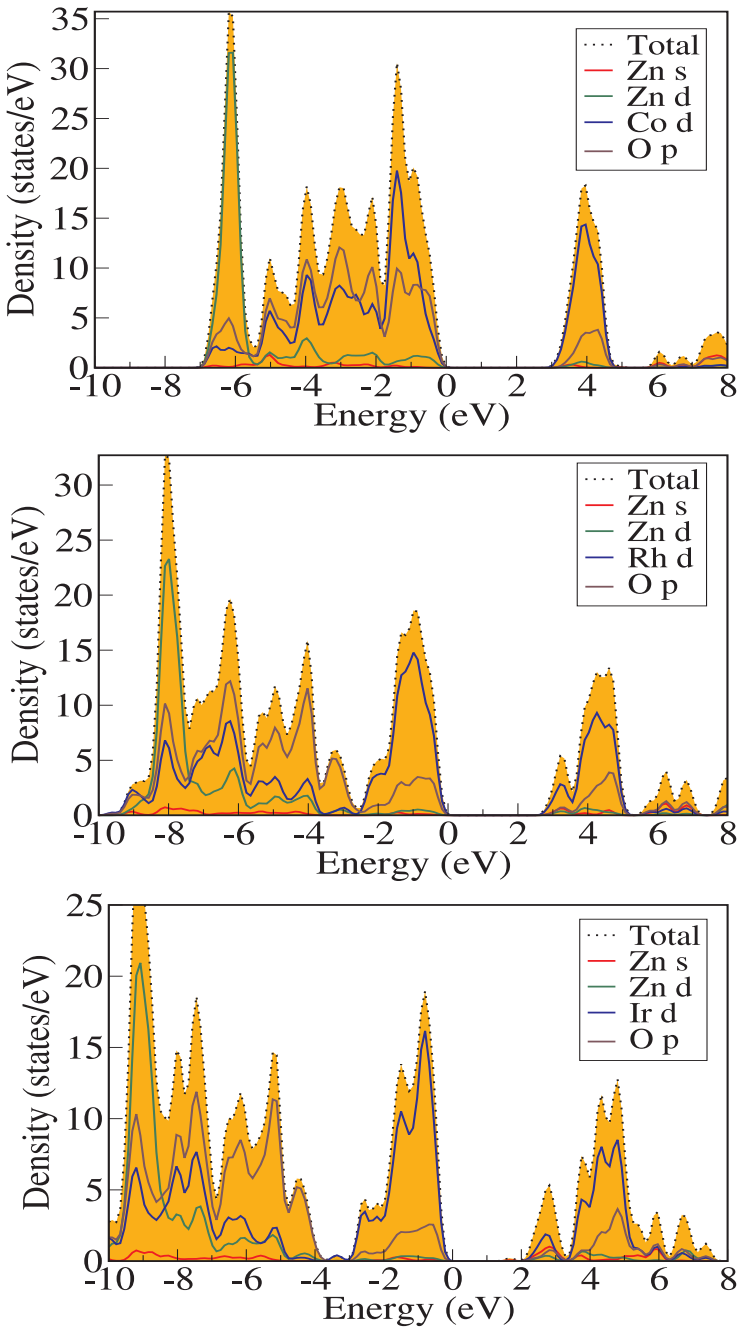

Figure 7.3: (Total and projected density of states calculated using HSE06 for $ZnCo_2O_4$, $ZnRh_2O_4$ and $ZnIr_2O_4$.

H

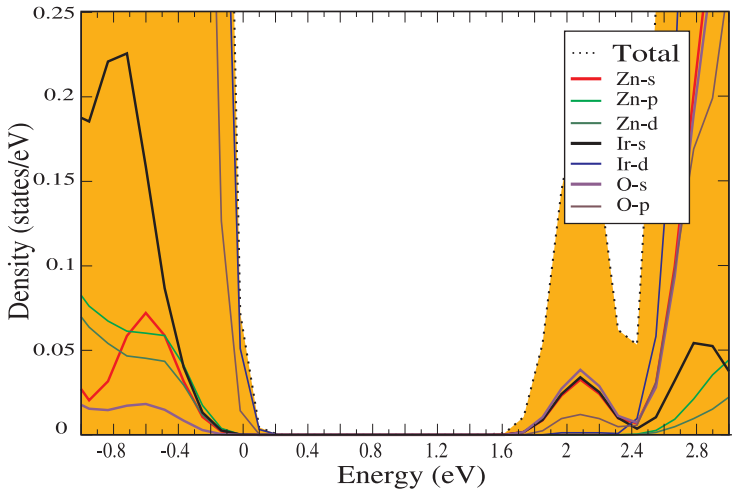

Figure 7.4: Total and projected density of states calculated using HSE06 for $ZnIr_2O_4$ close to the CBM.

thermore, this trend is also in agreement with the experimental results of Refs. [164, 165, 167, 168] for the $ZnCo_2O_4$ and $ZnRh_2O_4$ systems.

Nevertheless, the band gap values obtained with the HSE06 functional overestimate all experimental results. This motivated us to perform GW calculations for these spinel structures. Single shot GW calculations (G_0W_0) are performed on top of the hybrid results. The obtained band gap values and the Zn 3*d* peak positions are listed in Table (7.2). One can note that the difference between the GW and HSE06 result is reasonably small, supporting the validity of the HSE06 functional to describe the electronic properties of these spinels. Sometimes another approach is followed, in which the exchange mixing parameter in the HSE06 functional is not the standard value, but tuned to correspond with the experimental band gap. (For example, for $ZnRh_2O_4$, the experimental band gap of 2.1 eV is obtained for an exchange mixing of 15.28 %.) However, a single shot GW calculation on top of the extreme case of no exchange mixing, which is the PBE approach, leads again to a band gap value of 3.34 eV, indicating that tuning the exchange mixing is not a valid approach in this case. These GW findings support the claim for experimental re-examination of the band gap in these spinels. In the following we rely on the HSE06 functional with the standard exchange mixing.

Table 7.2: HSE06 band gap, GW band gap, and the Zn 3*d* peak position (in eV) for ZnM_2O_4 spinel. Note that since bands are almost flat close to the CBM and the VBM, we've calculated the band gaps at high symmetry points close to the CBM and the VBM.

Oxide	HSE06 gap	GW gap	Zn 3*d* peak (exp)	Zn 3*d* peak (HSE06)	Zn 3*d* peak (GW)
$ZnCo_2O_4$	3.96	3.99	-8.8	-6.8	-8.2
$ZnRh_2O_4$	2.88	3.33	-9.2	-7.8	-8.1
$ZnIr_2O_4$	2.37	2.75	-9.5	-9	-9.2

7.5 Band alignment and dopability

It is possible to obtain a first idea for p-type and/or n-type dopability of a material by comparing its VBM and CBM with other known materials. One can align the VBM and CBM of different semiconductors using a simple branch-point energy technique [175]. The BPE is the energy at which the gap states change behavior from donor- to acceptor-like. The BPE is the midgap energy averaged over the Brillouin zone

$$E_{BP} = \frac{1}{2N_k}\sum_k [\frac{1}{N_{CB}}\sum_i^{N_{CB}} \varepsilon_{c_i}(k) + \frac{1}{N_{VB}}\sum_j^{N_{VB}} \varepsilon_{v_j}(k)] \tag{7.1}$$

N_k is the number of points in the k meshes. N_{CB} and N_{VB} are the number of conduction and valence bands which are considered, and ε_c and ε_v are their corresponding energies. Recently, this method has been applied successfully to align band edges in semiconductors [183, 184]. Using the HSE06 hybrid functional, the band alignment diagram of wurtzite ZnO and $ZnCo_2O_4$, $ZnRh_2O_4$, and $ZnIr_2O_4$ spinels are shown in Fig. 7.5.

The BPE is a reference level to predict the n or p-type dopability of semiconductors. If it is closer to the VBM (CBM), then the material tends to act as p-type (n-type) semiconductor. If the CBM lies below the BPE, n-type conductivity may occur. In the case of ZnO the CBM lies below the BPE which is a known fact for ZnO that exhibits unintentional n-type conductivity. For $ZnCo_2O_4$, and $ZnRh_2O_4$ spinels, the CBM is also made from flat d-states as well as the VBM. Since the BPEs are somewhere in the gap, this in comparison to ZnO shows the slight tendency of p-dopability. However, this does not apply to $ZnIr_2O_4$ whose band gap is made up of *d-s* splitting according to the band structure results. Since *s* orbitals are

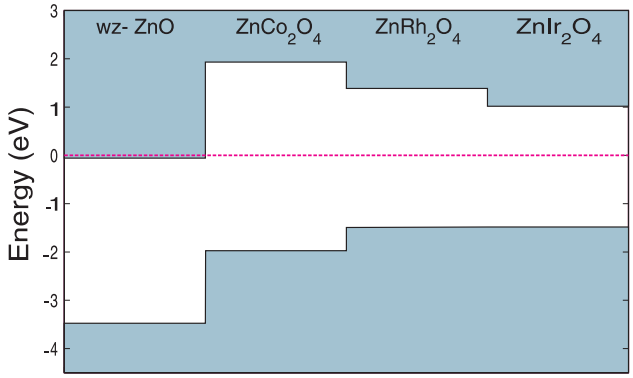

Figure 7.5: Band alignment in ZnO, $ZnCo_2O_4$, $ZnRh_2O_4$, and $ZnIr_2O_4$. BPE is used as reference level and is set to zero.

more disperse the BPE is closer to the CBM in comparison to the two other structures.

7.6 Formation energy calculations

The concentration of point defects and impurities depends on their formation energies. As it is discussed in chapter 3, the formation energy of a defect or impurity in different charge states is defined with Eq.(3.9). The formation energy equation indicates that the defect formation energy depends sensitively on the chemical potential of both atomic species and electrons (often referred to as the Fermi energy - E_F). This is because in forming the defect, particles are exchanged between the host material and the chemical reservoirs. For ternary systems, the chemical potentials of each constituent species can be varied to reflect specific equilibrium growth conditions, but are always globally constrained by the calculated formation enthalpy of the host in order to maintain its stability. The formation enthalpy of the ZnM_2O_4 spinel is

$$\begin{aligned} \triangle H_f^{ZnM_2O_4} &= E[ZnM_2O_4] - \mu_{Zn}^{Zn\ bulk} - 2\mu_M^{M\ bulk} - 4\mu_O^{O_2\ molecule} \\ &= -12.85\ \text{eV}(Co) \\ &= -7.81\ \text{eV}(Rh) \\ &= -5.62\ \text{eV}(Ir) \end{aligned} \tag{7.2}$$

Here $\mu_{Zn}^{Zn\ bulk}/\mu_M^{M\ bulk}$ correspond to the energy of a Zn/M atom in their bulk structures and $\mu_O^{O_2\ molecule}$ corresponds to the energy of an O atom in an oxygen molecule (calculated using spin polarized calculations).

7.6.1 Accessible chemical potential

The chemical potential depends on the experimental growth conditions which can vary from X-poor to X-rich, where X could be one of Zn, Co, Rh, Ir or O elements. In addition, further constraints are also imposed by formation of competing binary oxides such as ZnO or MO. Thus the range of accessible chemical potentials are fixed by the thermodynamic conditions such that the ZnM_2O_4 spinel is formed without decomposing into competing other binary or ternary phases. Here we will discuss the range of accessible chemical potentials for each of the spinels studied.

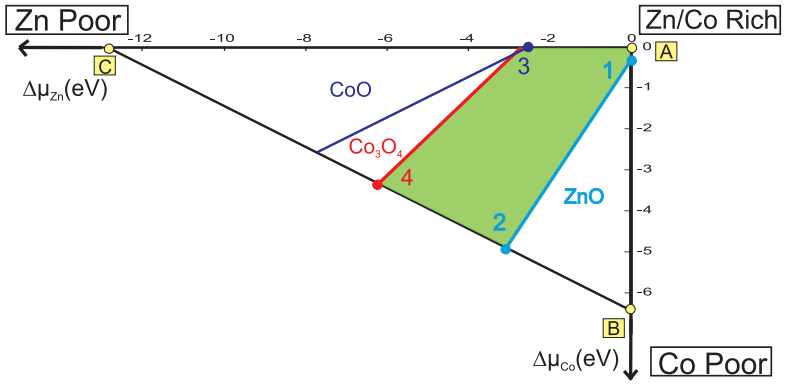

Figure 7.6: Calculated ranges of accessible chemical potentials for $ZnCo_2O_4$ spinel.

Firstly we consider the $ZnCo_2O_4$ spinel. The competing binary oxides are ZnO in the wurtzite structure, CoO in the rocksalt phase and Co_3O_4 also in the spinel phase. Thus in addition to Eq.(7.2), the relative chemical potentials of Zn, Co and O must satisfy following conditions

$$\begin{aligned} \triangle H_f^{ZnO} &= E[ZnO] - \mu_{Zn}^{Zn\ bulk} - \mu_O^{O_2\ molecule} && (7.3)\\ &= \Delta\mu_{Zn} + \Delta\mu_O && (7.4)\\ &= -3.06 \text{ eV} \end{aligned}$$

$$\begin{aligned} \triangle H_f^{CoO} &= E[CoO] - \mu_{Co}^{Co\ bulk} - \mu_O^{O_2\ molecule} && (7.5)\\ &= \Delta\mu_{Co} + \Delta\mu_O && (7.6)\\ &= -2.53 \text{ eV} \end{aligned}$$

$$\triangle H_f^{Co_3O_4} = E[Co_3O_4] - 3\mu_{Co}^{Co\ bulk} - 4\mu_O^{O_2\ molecule} \tag{7.7}$$

$$= 3\Delta\mu_{Co} + 4\Delta\mu_O \tag{7.8}$$

$$= -9.99 \text{ eV}$$

Here $\Delta\mu_{Zn} = \mu_{Zn}^{ZnO} - \mu_{Zn}^{Zn\ bulk}$ and $\Delta\mu_O = \mu_O^{ZnO} - \mu_O^{O_2\ molecule}$ indicating the possible variation of the Zn and O chemical potential when ZnO is formed. The same holds for other binary and ternary oxide systems that are considered here. Furthermore $\Delta\mu_{Zn} \leq 0$, $\Delta\mu_{Co} \leq 0$, $\Delta\mu_O \leq 0$ to avoid the elemental precipitation. The resulting accessible range of the chemical potentials, is illustrated in Fig. 7.6 in a two-dimensional ($\Delta\mu_{Zn}$, $\Delta\mu_{Co}$) plane. The vertices of the stability triangle are formed from the host condition (Eq.(7.2)) giving the limits of Zn/Co rich, Zn poor and Co poor environments, respectively. The hypotenuse of this triangle reflects the oxygen rich condition.

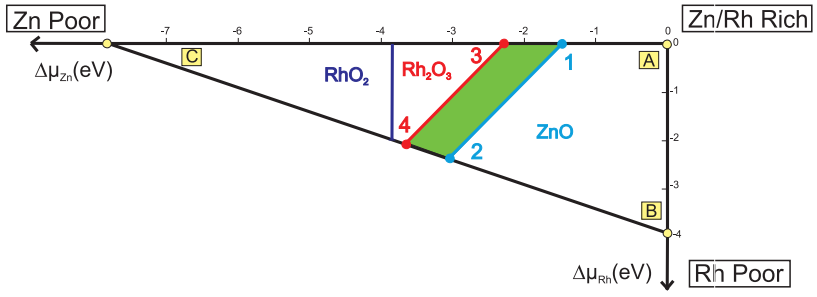

Figure 7.7: Calculated ranges of accessible chemical potentials for $ZnRh_2O_4$ spinel.

Similarly for $ZnRh_2O_4$ spinel we have additional constraints induced by formation of binaries - ZnO in the wurtzite, Rh_2O_3 in the corundum and RhO_2 in the tetragonal rutile phase.

$$\triangle H_f^{ZnO} = E[ZnO] - \mu_{Zn}^{Zn\ bulk} - \mu_O^{O_2\ molecule} \tag{7.9}$$

$$= -3.06 \text{ eV}$$

$$\triangle H_f^{Rh_2O_3} = E[Rh_2O_3] - 2\mu_{Rh}^{Rh\ bulk} - 3\mu_O^{O_2\ molecule} \tag{7.10}$$

$$= -4.15 \text{ eV}$$

$$\triangle H_f^{RhO_2} = E[RhO_2] - \mu_{Rh}^{Rh\ bulk} - 2\mu_O^{O_2\ molecule} \tag{7.11}$$

$$= -1.98 \text{ eV}$$

The triangle of the chemical potentials for $ZnRh_2O_4$ spinel is shown in Fig. 7.7 and the stable region is shown by shaded area. Note that the accessible range is now restricted to a narrow region in comparison with the $ZnCo_2O_4$ spinel.

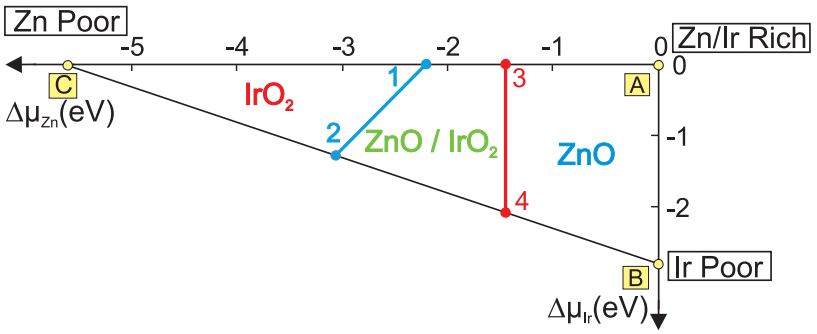

Figure 7.8: Calculated ranges of accessible chemical potentials for $ZnIr_2O_4$ spinel.

In contrast to the results mentioned above, we do not observe a stable region in which $ZnIr_2O_4$ spinel is formed without decomposing into the binaries: ZnO and IrO_2. Again the two dimensional phase space for accessible chemical potentials is determined from following equations

$$\begin{aligned} \triangle H_f^{ZnO} &= E[ZnO] - \mu_{Zn}^{Zn\ bulk} - \mu_O^{O_2\ molecule} \\ &= -3.06 \text{ eV} \end{aligned} \tag{7.12}$$

$$\begin{aligned} \triangle H_f^{IrO_2} &= E[IrO_2] - \mu_{Ir}^{Ir\ bulk} - 2\mu_O^{O_2\ molecule} \\ &= -2.09 \text{ eV} \end{aligned} \tag{7.13}$$

The results obtained for the accessible chemical potentials are shown in Fig. 7.8. The constraints induced by competing binary oxides overlap with each other indicating that the $ZnIr_2O_4$ spinel would readily decompose into ZnO and IrO_2. This supports the fact that in experiments bulk $ZnIr_2O_4$ could not be synthesized by solid-state synthesis using ZnO and IrO_2 and for the thin film fabrication of $ZnIr_2O_4$, a multi-component $ZnO:(IrO_2)_2$ target is essential [166].

All the above mentioned enthalpies of formation are obtained within the HSE06 approach. It is instructive to compare these values with the reported experimental values, as given in Table (7.3). Note that a reasonable agreement is obtained, within tenths of eV, which is of the same order as the differences between different reported experimental values, when available.

Table 7.3: Comparison between the enthalpies of formation for the competing binary phases obtained within the HSE06 approach and the reported experimental values.

Oxide	Experimental (eV)	HSE06 (eV)
ΔH (ZnO)	-3.60 [185]	-3.06
ΔH (CoO)	-2.46 [186]	-2.53
ΔH (Co_3O_4)	-9.23 [186]	-9.99
ΔH (Rh_2O_3)	-3.55 [185], -3.73 [187]	-4.15
ΔH (RhO_2)	-2.54 [187] , -1.91 [185]	-1.98
ΔH (IrO_2)	-2.84 [186] , -2.57 [187]	-2.09

We also want to note that the stability triangles for $ZnCo_2O_4$ and $ZnRh_2O_4$ are similar to those presented in Ref. [172] obtained within the GGA+U approximation, but not identical. The stability regions with the HSE06 are larger. The chemical potentials determine the formation energies of defects, but not the transition levels. As such, these small differences in stability triangles have no influence on the final results.

7.6.2 Formation energies

The calculated formation energies for the cation vacancy and the antisite defects, Zn_M (Zn replacing M), are shown in Fig. 7.9, 7.10, and 7.11 for different growth conditions. The Fermi energy varies between the VBM up to the CBM. For the case of $ZnCo_2O_4$ and $ZnRh_2O_4$ spinel the formation energies are plotted at the values of chemical potentials that correspond to the vertices of the stability region in which the ternary spinel is formed without decomposing into the binary oxides. Since $ZnIr_2O_4$ spinel is a metastable structure and cannot be synthesized from binary oxide systems, we have chosen metal (Zn/M) rich or oxygen rich conditions while plotting the formation energies. This corresponds to the points A, B and C as discussed in Fig. 7.8.

In the case of $ZnCo_2O_4$ spinel, we observe that the antisite defect Zn_{Co} is a deep acceptor. However, note that the crossing between the neutral and -1 charge states occurs only 0.14 eV above the VBM and therefore may also contribute to p-type conductivity. The antisite Zn_{Co} has lower formation energy than the other defects at vertices 1 and 2 of the stability region. At the remaining vertices (3 & 4) the Zn vacancy appears to be stable and prefers -2 charged state. The formation energies of the cation vacancies at the vertex 1 & 2 are high indicating that the antisite defect is the leading cause

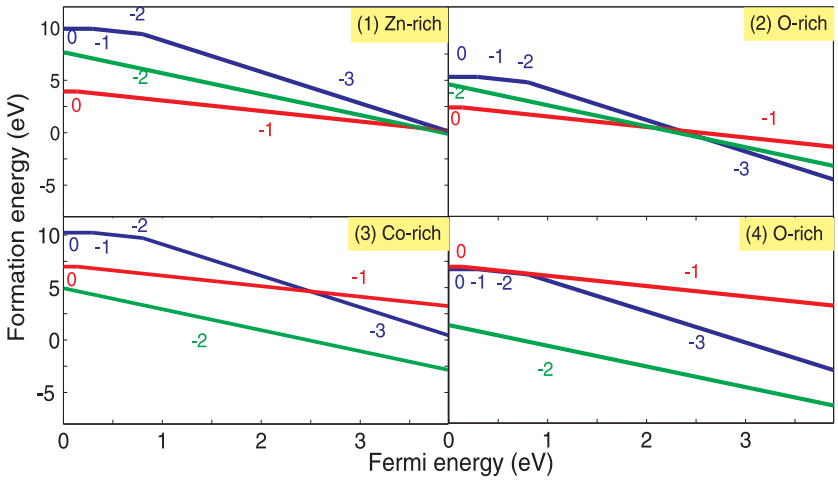

Figure 7.9: Calculated defect formation energies as a function of Fermi energy at the values of chemical potentials that corresponds to the vertices of the stability region for $ZnCo_2O_4$. Blue lines are V_{Co}, green lines are V_{Zn} and red lines are Zn_{Co}.

of disorder in $ZnCo_2O_4$ spinel. However under Co or oxygen rich conditions the Zn vacancy has the lowest formation energy and thus the observed p-type conductivity is probably a result of both the antisite defect and the Zn vacancy. Thus under both metal and O rich conditions the antisite defect has a high formation energy, which will limit the number of charge carriers. We can compare our results with a similar study on $ZnCo_2O_4$ from Perkins et al. [173] based on GGA+U calculations. It was also found that the antisite Zn_{Co} is an acceptor with a transition level at 0.34 eV above the VBM which was called a reasonably shallow level. However, it is deeper compared to our transition point (0.14 eV above the VBM). The V_{Zn} defect, on the other hand, was found to be an amphoteric defect in this Ref., while in our DFT study based on the HSE06 hybrid functional it is shown to be a shallow acceptor and thus also contributes to the observed p-type conductivity.

Figure 7.10 corresponds to the $ZnRh_2O_4$ spinel. Both the Zn vacancy and the antisite defect, Zn_{Rh}, are shallow acceptors while the Rh vacancy is a deep acceptor. We observe a crossover between the charged defect states as a function of Fermi energy. In comparison to $ZnCo_2O_4$, the formation energy of the antisite defect is lower and therefore it might result in a higher concentration of charge carriers.

As it is shown in Fig. 7.8, the stability lines in the triangle are switched and the $ZnIr_2O_4$ ternary compound is not stable with respect to its considered binaries. Thus in order to compare the results with the two other

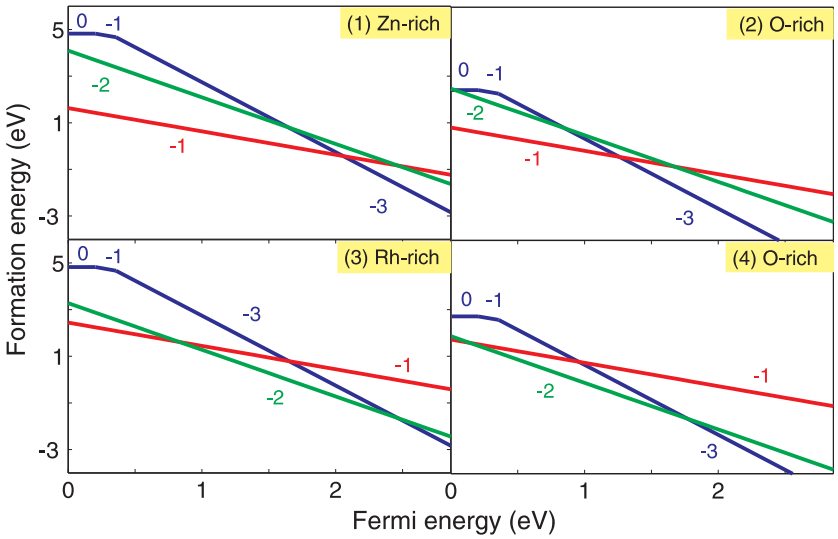

Figure 7.10: Calculated defect formation energies as a function of Fermi energy at the values of chemical potentials that corresponds to the vertices of the stability region for $ZnRh_2O_4$. Blue lines are V_{Rh}, green lines are V_{Zn} and red lines are Zn_{Rh}.

spinels, we have shown the formation energies calculated using the chemical potentials at the points A, B and C for all three spinels considered in this study. These points correspond to elemental (Zn/M/O) rich condition. The native defects in $ZnIr_2O_4$ exhibit a similar behavior as in the case of $ZnRh_2O_4$ and we observe that both Zn vacancy and the antisite defect - Zn_{Ir} are shallow acceptors. The Ir vacancy acts like a shallow acceptor. Under metal rich conditions (point A), the antisite defect has the lowest formation energy; however close to the conduction band we observe a crossover with the M-cations. Antisite defect is also the most stable defect under M-poor conditions (point B) and the formation energy of M-cations is also lowered as a consequence of lower chemical potential. Under the Zn-poor conditions (point C) the Zn vacancy is the most stable defect among all spinels. Since the $ZnCo_2O_4$ and $ZnRh_2O_4$ spinels are obtained using solid state synthesis of binary oxides and $ZnIr_2O_4$ is a metastable phase [164, 165, 166], the oxygen rich conditions are unlikely in these experiments. This excludes the possibility of point B & C in the range of accessible chemical potentials and we believe that only point A can be relevant in experiments. Thus with metal rich conditions the antisite defect is the leading cause of disorder. Furthermore the formation energy of the antisite defect, Zn_M, decreases while going down the group and it corroborates the enhanced p-type conductivity reported for the $ZnRh_2O_4$ and $ZnIr_2O_4$ spinels.

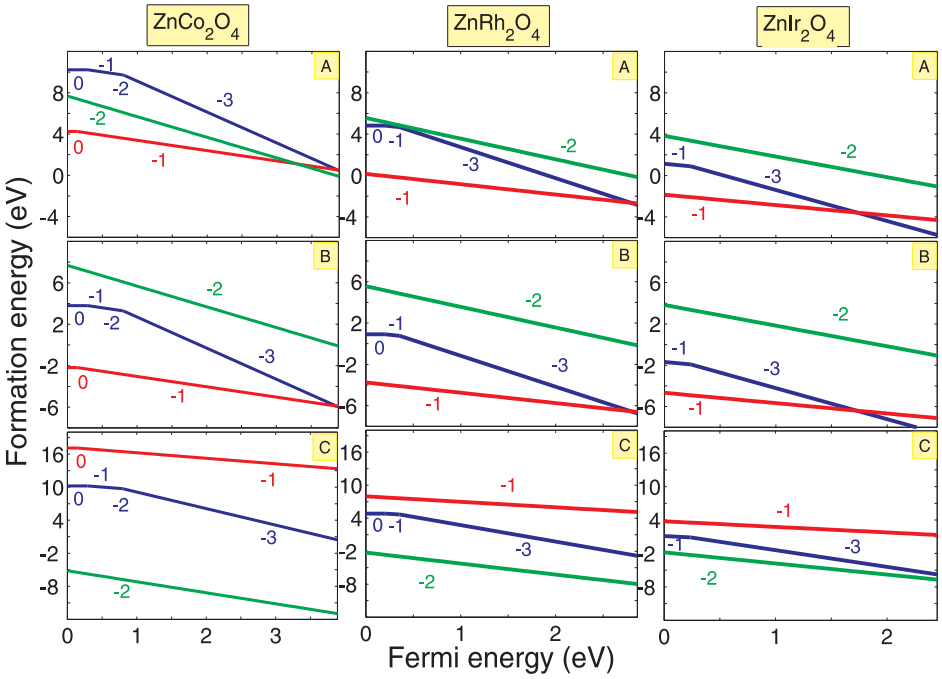

Figure 7.11: Calculated defect formation energies as a function of Fermi energy under different metal (point A & B) and oxygen rich (point C) condition for ZnM_2O_4. Blue lines are V_M, green lines are V_{Zn} and red lines are Zn_M.

7.7 Atomic geometries

For a more complete description of the cation vacancy and the antisite defects, we further analyze the atomic geometries as shown in Fig. 7.12. In the spinel structure, the Zn atoms occupy tetrahedral sites while M atoms occupy the octahedral positions. The optimized cation-anion (Zn/M - O) bond lengths are summarized in Table (7.4). When either cation (Zn/M) is removed to create a vacancy, we notice the oxygen atoms that were coordinated with the vacancy site are now pulled towards the cations of another type (M/Zn). This results in a reduction of those cation-anion bond lengths by $\sim 3.5\%$.

On the other hand, in the case of the antisite defect when the M cation is replaced by the Zn atom at the octahedral site, we notice that the Zn-O bond length is increased by 2% as shown in Fig. 7.12c. This is because of the larger ionic radius of the Zn atom compared to the M cations.

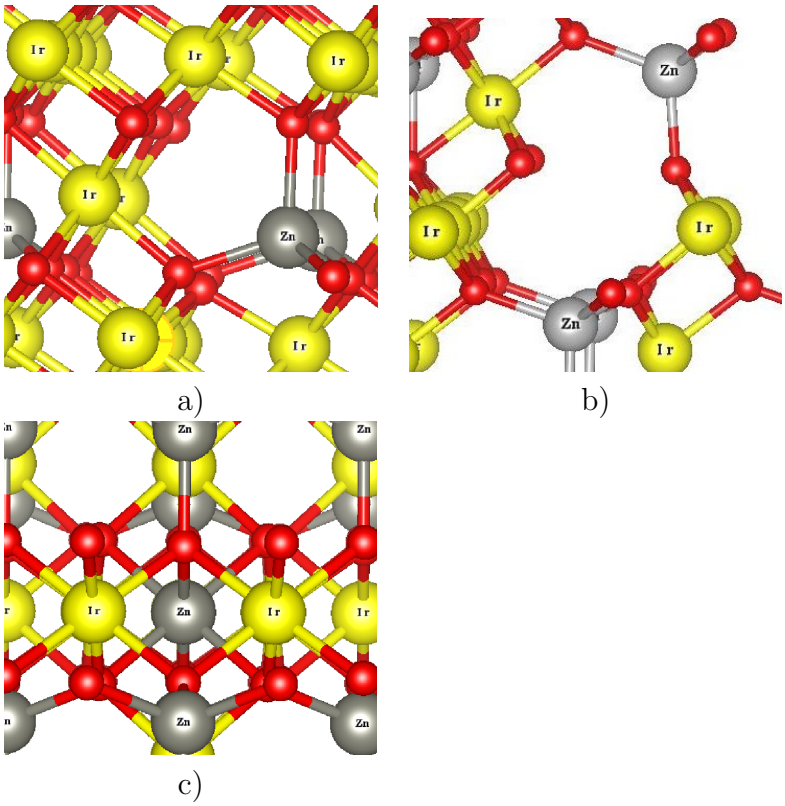

Figure 7.12: Relaxed atomic geometries for the prototype case of $ZnIr_2O_4$ spinel. Zn, Ir vacancy and the Zn_{Ir} antisite defect are shown in Fig. a), b) and c) with the Zn, Ir and O atoms shown with the gray, yellow and red color respectively.

Table 7.4: Cation-anion bond lengths for nearest neighbor in case of vacancy and the antisite defect (in Å).

Site	Unrelaxed	Relaxed
V_{Co}	1.89	1.82
V_{Rh}	2.04	1.97
V_{Ir}	2.06	1.98
V_{Zn} ($ZnCo_2O_4$)	1.90	1.86
V_{Zn} ($ZnRh_2O_4$)	2.05	1.99
V_{Zn} ($ZnIr_2O_4$)	2.05	2.00
Zn_{Co}	1.89	1.93
Zn_{Rh}	2.05	2.10
Zn_{Ir}	2.06	2.10

7.8 Polaron effects

Having flat non-dispersed bands around the Fermi level results in large density of states and effective mass in these spinels and therefore the conductivity is limited in these oxides. Furthermore, this might lead to the formation of localized small polarons, which are localized holes trapped by local lattice distortions that are called self trapped holes (STH) [188]. The stability of the STH in a given material is defined by the self-trapping energy E_{ST}

$$E_{ST} = E_{tot}[X_mO_n : h^+] - E_{tot}[X_mO_n : \eta^+] \tag{7.14}$$

where $E_{tot}[X_mO_n : h^+]$ and $E_{tot}[X_mO_n : \eta^+]$ are the total energies of a supercell of the unrelaxed crystal containing a hole in the VBM, and the total energy of the further relaxed supercell containing a hole. $E_{ST} > 0$ indicates that the self-trapped holes are stable.

Table 7.5: Calculated self-trapping energy in (eV) for studied oxides using the hybrid functional.

Oxide	E_{ST} (eV)
$ZnCo_2O_4$	0.00
$ZnRh_2O_4$	0.16
$ZnIr_2O_4$	0.13

The calculated self-trapping energies (E_{ST}) are listed in the Table (7.5). From the results obtained, we observe that for $ZnCo_2O_4$ the holes are unlikely to be self-trapped. On the other hand, for $ZnRh_2O_4$ and $ZnIr_2O_4$ the

self-trapping energy is 0.16 and 0.13 eV respectively, suggesting that STH are present in these oxides. These results based on the HSE06 functional predict that the conductivity in these spinels is likely to be further limited by polarons. Recently however, calculations based on the DFT+U approach by Nagaraja *et. al.* [180] have suggested that the self-trapping energy of holes is endothermic indicating that the band character is responsible for the conductivity and not polarons. Although the presence of small polarons in $ZnRh_2O_4$ was reported in Ref. [167], re-examination of the experimental data together with Hall measurements [180] contradicted this self-trapping. This shows that the use of the HSE06 functional should be used with caution to study the self-trapping mechanism.

7.9 Conclusions

We have reported a comprehensive first-principles study of formation energies of acceptor like defects in ZnM_2O_4 (M=Co, Rh, and Ir) spinels using a hybrid functional. The validity of the HSE06 functional to describe these spinel structures was supported by GW calculations. The electronic band structure shows a non-dispersed VBM indicative of a heavy hole mass for these oxides. The ternary $ZnCo_2O_4$ and $ZnRh_2O_4$ spinels are stable structures with respect to the formation of binary oxides - ZnO, CoO, Co_3O_4, RhO_2 and Rh_2O_3, whereas the $ZnIr_2O_4$ spinel is a metastable phase.

A systematic study of the formation energy with different chemical potentials that correspond to different experimental growth conditions, helps to identify the stable defects. For $ZnCo_2O_4$ we observe that the Zn vacancy becomes a stable defect when the chemical potential of Zn is lowered and also acts as a shallow acceptor, in contrast to a recent GGA+U study [173] which found it as an amphoteric defect. Similarly a crossover between the antisite defect and cation vacancy is observed for $ZnRh_2O_4$ spinel. However under elemental M-rich and O-rich conditions, the antisite defect has the lowest formation energy in all the three spinels and it acts as a shallow acceptor defect in both $ZnRh_2O_4$ and $ZnIr_2O_4$ structures, while it is a deep acceptor for the $ZnCo_2O_4$ spinel, but with a transition level of only 0.14 eV above the VBM. The analysis of relaxed atomic geometries shows that the Zn-O bond length increases by 2% in the case of the antisite defect, while it results in $\sim$3.5% bond reduction in case of vacancies. Furthermore, the formation energy of the antisite defect for $ZnCo_2O_4$ is higher than the remaining two oxides studied and this explains why the conductivity increases while moving from Co to Rh/Ir. Finally, our analysis of STH using the HSE06 functional in these spinels indicates that there are only stable STHs

in case of the $ZnRh_2O_4$ and $ZnIr_2O_4$ spinel. This is not in agreement with recent experiments, which shows that this hybrid functional is not able to describe this subtle phenomenon correctly.

We can summarize the advantages and disadvantages of each spinel system in the following. For $ZnCo_2O_4$ the holes introduced by antisite defects are unlikely to be self-trapped, however their formation energy under both M-rich and O-rich conditions is high which limits the number of charge carriers. For $ZnRh_2O_4$ and $ZnIr_2O_4$ spinels, the formation energy of the antisite defect is systematically lowered and thus a larger number of charge carriers is likely to be created. This nicely corroborates the enhanced conductivity in $Zn(Rh/Ir)_2O_4$ spinel reported experimentally.

Chapter 8

The Oxygen Vacancy in ZnO: From Bulk to Slabs

8.1 Introduction

A key characteristic of dopant impurities is their deep or shallow nature. The standard theoretical approach to examine this in the case of dopants in bulk semiconductors is through calculations of formation energies as a function of the Fermi level, as applied in the previous chapters. The neutral as well as different charge states of the defect have to be considered. The position of the thermodynamic transition level between different charge states determines if a defect has a shallow or deep character. Up to now, such transition levels have been determined with ab initio methods only for bulk crystal structures. Nevertheless, the character of a defect in a nanostructure might differ from its character in the bulk material. However, the above method cannot be transferred directly to nanostructures. In calculations for a charged defect, a uniform background charge is considered. While this is well-defined for bulk crystal calculations, the total energy of a charged nanostructure depends linearly on the width of the vacuum as a result of the interaction between the charged system and the compensating background. Therefore, total energies obtained from calculations for charged nanostructures cannot be used to determine formation energies. In this chapter we propose a method to determine the transition levels between different charge states without using the formation energy of a defect in a charged state. As an example, we focus on the oxygen vacancy in ZnO slabs.

ZnO is a commonly used semiconductor material, which was already introduced and studied in chapters 5 and 6 of this thesis. Although the band gap of ZnO in the wurtzite structure has a large value of 3.4 eV [146], un-

doped ZnO reveals n-type conductivity at room temperature. Originally it was believed that this n-type behavior was caused by oxygen vacancies [104]. However, ab initio calculations have revealed that the oxygen vacancy in ZnO is a deep level [108], and the observed conductivity has been attributed to defects involving H impurities [144, 145, 105]. Not only bulk crystals, but also thin films and nanoparticles of ZnO are grown and studied nowadays [189, 190, 191, 192]. Therefore we have chosen to apply our method to the oxygen vacancy defect in a ZnO slab. The electronic structure of this defect is well known in bulk ZnO, and we investigate here how its properties change in a nanostructure, i.e. we investigate the dependence of the transition level (and thus the ionization energy) on the distance of the vacancy to the surface.

8.2 Computational details

First-principles total-energy calculations are performed using density functional theory (DFT) within the Perdew-Burke-Ernzerhof (PBE) [38] approach and the screened hybrid functional of HSE06 [60], as implemented in the Vienna ab initio simulation package [66, 116]. We have used 37.5% mixing of Hartree-Fock exchange in the HSE06 functional, which was shown before to give the correct band gap of bulk ZnO [103]. Electron-ion interactions are treated using projector augmented wave potentials [67, 68, 65]. The Zn ($4s^2 3d^{10}$), and O ($2s^2 2p^6$) electrons are treated as valence electrons. A 4×4×4 and 4×4×1 meshes of special k-points based on the MonkhorstPack scheme [63] are chosen for the integrations over the Brillouin zone in bulk and slab structures, respectively. The electron wavefunctions are described using a plane-wave basis set with an energy cutoff of 400 eV. The convergence with respect to self-consistent iterations was assumed when the total energy difference between cycles was less than 10^{-4} eV and the geometry relaxation tolerance was better than 0.01 eV/Å. (We do not use the HSE06 functional for atomic position relaxation in the case of the supercell because of its computational cost and because the PBE functional is known to yield reliable structural parameters.)

8.3 The oxygen vacancy in bulk ZnO

We study ZnO in the bulk wurtzite structure and defects are simulated by removing atoms from a 72-atom supercell. Figure 8.1 shows this structure. Removing an oxygen atom from the supercell creates four Zn dangling bonds.

The effect of the oxygen vacancy, V_O, in ZnO has been studied within several theoretical approaches previously [98, 86]. It is shown both theoretically and experimentally that the oxygen vacancy acts as a deep donor in ZnO [108, 193, 194].

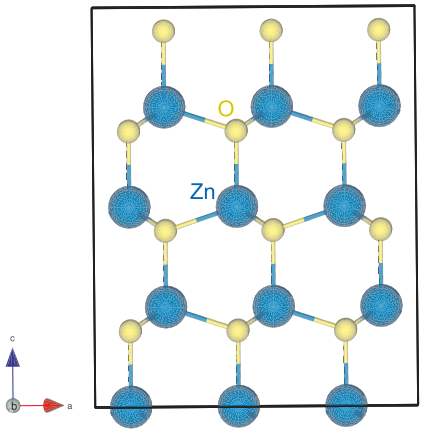

Figure 8.1: ZnO bulk structure in a supercell with 72-atom.

In order to test the validity of the new method we propose, we first reproduce the result of the standard approach with the HSE06 functional. The formation energy of an oxygen vacancy in bulk ZnO in different charge states is defined in Eq.(3.9) and is given by

$$E_f[V_O^0] = E_{tot}[V_O^0] - E_{tot}[ZnO^{bulk}] + \frac{1}{2}E(O_2^{molecule}) + q[E_F + E_v + \Delta V] \quad (8.1)$$

$E_{tot}[V_O^0]$ is the total energy from a supercell calculation with an oxygen vacancy and $E_{tot}[ZnO^{bulk}]$ is the total energy for the equivalent perfect supercell. The third term indicates the chemical potential of an oxygen which is the energy of the reservoirs with which atoms are being exchanged. This chemical potential depends on the experimental growth conditions. Here we assume oxygen rich conditions and it is equal to half of the total energy of an isolated oxygen molecule. E_F is the electronic reservoir chemical potential (Fermi energy), measured with respect to the VBM, E_v, of the undoped system. ΔV aligns the reference potentials in the defect and perfect cells in a region far from the defect, where the potential is bulk-like. Since it is known from literature that the 1+ charge state of the V_O is not stable in ZnO (and we have also verified it), we only consider the neutral and 2+ charge states. The full lines in Fig. 8.2(a) show these formation energies as function of the Fermi level for both 0 and 2+ relaxed situations. The transition, labeled

as point 1, occurs clearly deep in the gap at 2.50 eV above the VBM, i.e. 0.93 eV below the CBM, showing the deep donor character of V_O in ZnO. As discussed in section 3.5.3, this crossing in formation energies between the relaxed neutral and the relaxed 2+ charge states is referred to as the thermal ionization energy. However, the excitation energy measured in optical experiments is different from the thermodynamic transition level, because the atoms do not have the time to relax to their ground state positions corresponding to the new situation[1]. Therefore, the optical ionization energy can be found by considering the formation energy of 2+ charged V_O, but with the coordinates of the relaxed neutral situation, $V_O^{2+}[R(0)]$. This formation energy, as function of the Fermi level is shown by the dashed line with slope +2 in Fig. 8.2(a). The crossing between the $V_O^{2+}[R(0)]$ and $V_O^0[R(0)]$ occurs at 0.66 eV above the VBM, and is labeled by point 2. The optical ionization is thus found to be 2.77 eV.

This crossing point 2 in Fig. 8.2(a) can in good approximation also be determined without relying on the formation energy of the charged system. The red curve in Fig. 8.3 shows the density of states of the relaxed neutral $V_O^0[R(0)]$ supercell calculation. The alignment is made with the density of states of the pure system. One can observe an occupied peak close to the VBM in this density of states. This peak corresponds to the two electrons in the dangling bonds in the oxygen vacancy. From the DOS, we observe that it is located at ~ 0.78 eV above the VBM of the pure system, thus at 2.65 eV below the CBM. This is a good approximation for the optical ionization energy. The position of this peak is also marked with label 2 in Fig. 8.2(b), and corresponds thus approximately with point 2 in Fig. 8.2(a). The thermal ionization energy however, cannot be determined directly from such a density of states calculation for a neutral system. But indirectly, it can.

As mentioned, the total energy of a charged slab calculation cannot be used to determine a defect formation energy. However, this does not mean that a charged slab calculation is meaningless: the relaxed positions and density are correct. Let us consider the formation energy of $V_O^0[R(2+)]$, given by the horizontal dashed line in Fig. 8.2(a). Its crossing with the $V_O^{2+}[R(2+)]$ formation energy line should correspond to a peak in the DOS of the $V_O^0[R(2+)]$ system. To see this, it is instructive to consider some intermediate coordinates between the relaxed coordinates of 0 (labeled $R(0)$) and 2+ (labeled $R(2+)$) charge states. These intermediate coordinates are labeled by X_i with $i = [1:7]$. Figure 8.3 shows the DOS of these intermediate situations, all for

[1]The optical transition energy in this chapter is the minimal energy needed to excite an electron to the minimum of the conduction band, or the simultaneous excitation of both electrons. We do not consider the optical ionization of the second electron after ionization of the first one.

the neutral charge state. One can see that the peak in the density of states, from which the optical ionization energy could be determined, increases in energy, and finally ends up in the conduction band. Figure 8.2(b) shows the formation energies for all these intermediate systems, together with the position of the peaks in the DOS plot.

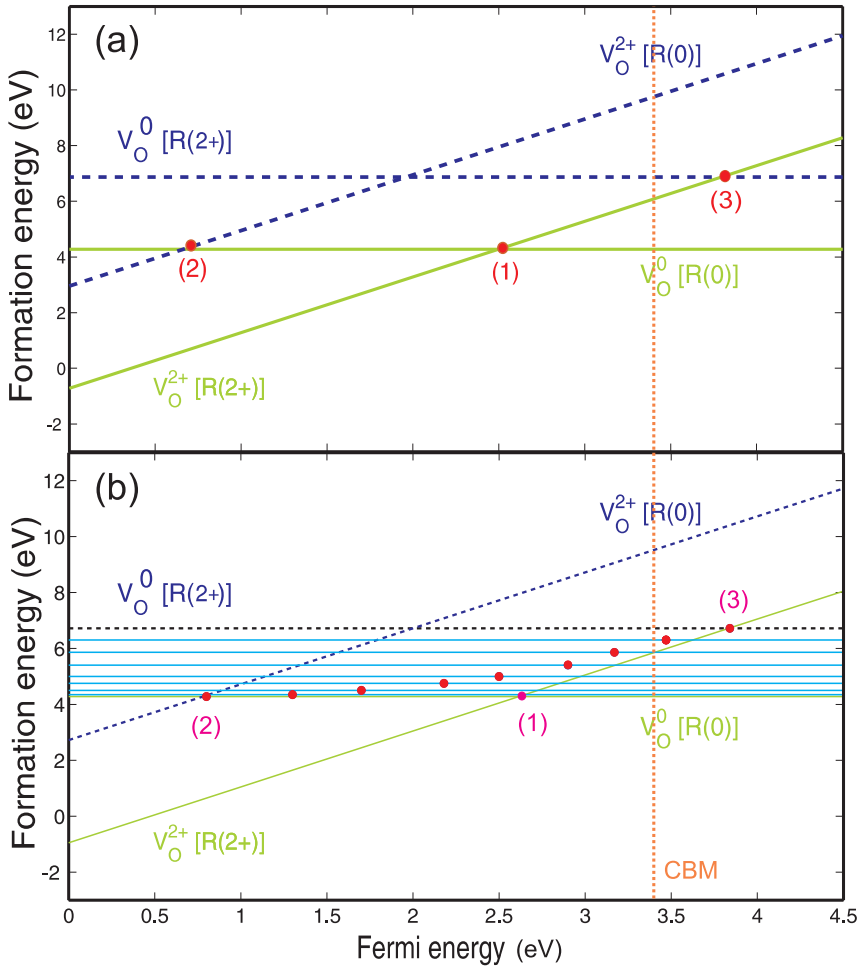

Figure 8.2: (a) The formation energy as a function of the Fermi energy for V_O in bulk ZnO obtained from the directly calculated formation energies using the hybrid HSE06 functional, (b) the formation energies for some intermediate coordinates between $R[0]$ and $R[2+]$. ($V_O^q[R(q')]$ indicates the oxygen vacancy defect in charge state q in the relaxed coordinates of the charge state q').

The final peak position for the neutral system considered in the relaxed

coordinates $R[2+]$ is 3.84 eV above the VBM and is marked as point 3 in Fig. 8.2(b). As just mentioned, this must be approximately equal to the crossing point between the formation energies of $V_O^0[R(2+)]$ and $V_O^{2+}[R(2+)]$, i.e. point 3 in Fig. 8.2(a). An estimate for the thermal ionization energy can now be obtained easily by drawing a line with slope +2 through this point 3 shown in Fig. 8.2(b). This is our approximation for the formation energy of $V_O^{2+}[R(2+)]$. The crossing with the formation energy line for the relaxed neutral $V_O[R(0)]$ system is our estimate for point 1, the thermal transition level. We find that it is given by 2.62 eV above the VBM, leading to a thermal ionization energy of 0.81 eV. Comparing with the value of 0.93 eV obtained with the standard approach shows that we can indeed obtain a good estimate for the thermal ionization energy without using total energies of charged supercells.

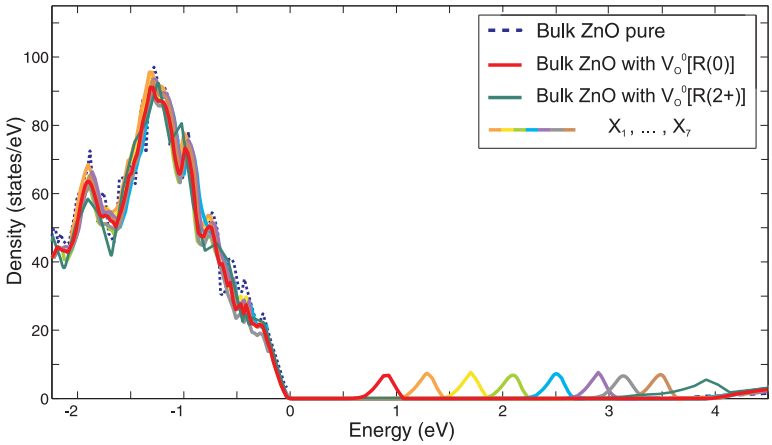

Figure 8.3: The DOS for pure and with V_O^0 in 0, +2 and 7 intermediate coordinates in bulk ZnO.

In the above scheme, the optical and thermal ionization energies of the defect state are obtained from two DOS plots, i.e. for the systems $V_O^0[R(0)]$ and $V_O^0[R(2+)]$. However, if the atomic defect level moves into the conduction band as in the above example for $V_O^0[R(2+)]$, it might be difficult to determine its exact position due to hybridization with the conduction bands. However, only the DOS of the $V_O^0[R(0)]$ case is also sufficient. The peak position in this DOS gave us point 2 in Fig. 8.2(b). As already discussed, the line with slope +2 through this point must correspond to the formation energy for the defect $V_O^{2+}[R(0)]$[2].

[2]In fact this is equivalent to subtracting twice the Fermi energy from the energy of system $V_O^0[R(0)]$ obtained from the supercell calculation, and adding twice the energy $2E_F$.

We find that further relaxing this system lowers the total energy with 3.67 eV. In this way we obtain the formation energy for system $V_O^{2+}[R(2+)]$, which is again the green line passing between point 1 and 3 in Fig. 8.2(b). The crossing between the formation energies for the systems $V_O^0[R(0)]$ and $V_O^{2+}[R(2+)]$ turns out to be at 2.61 eV. Therefore the thermal ionization energy is found to be 0.82 eV, in good agreement with previous approaches. In this last approach we did make use of the total energies of the charged calculations, however only of their relative difference. We never compared total energies of a neutral and a charged system and therefore this approach is also applicable to nanostructures.

8.4 The oxygen vacancy in a thin ZnO slab

In previous section, we have proposed and verified a method to calculate the optical and thermal ionization energy without calculating formation energies for charged systems explicitly. Here we apply this approach to the oxygen vacancy in a thin ZnO slab structure and investigate how these ionization energies depend on the position of the oxygen vacancy. Furthermore we want to investigate the preferential position of an oxygen vacancy. This preferential position together with the corresponding ionization energies will determine the transport properties of the nanostructures. Figure 8.4 shows the passivated ZnO slab we consider. Fractionally charged hydrogen atoms are used to passivate the dangling bonds on both up and down surfaces of the slab. When a surface atom has i valence electrons distributed between 4 bonds in the tetrahedral position, this atom supplies $i/4$ electrons for each of the bonds. Therefore a passivating H atom should provide $(8-i)/4$ additional electrons to complete the bond. Therefore at the top surface of our ZnO slab, ended by Zn atoms, we need H atoms with fractional charge 3/2 while at the bottom surface, ended by O atoms, we need H atoms with fractional charge 1/2 [195]. The thickness of this slab is ~ 16 $\mathring{A}$ (i.e. 3 bulk unit cells in the [0001] direction) and the vacuum thickness is ~ 18 $\mathring{A}$. The calculated band gap of this thin slab is 3.74 eV using the HSE06 functional. The increase in the band gap with respect to the bulk value of 3.43 eV is due to the confinement effect.

To justify the supercell size, we consider two different ZnO slab supercells, one with 84 atoms (a 3×2 supercell) and the other one with 126 atoms (a 3×3 supercell). We consider an oxygen vacancy defect in the middle of the supercell for both cases and relax the corresponding atomic coordinates. Figure 8.5 shows the ionic configurations around the vacancy atom after the relaxation. Distances from some nearest neighbors to the vacancy site are

listed in Table 8.1. It is clear that the changes in the distances are not too large (less than 3%)[3]. Therefore we can safely choose the smaller supercell with 84 atoms for our calculations which reduces the computational time.

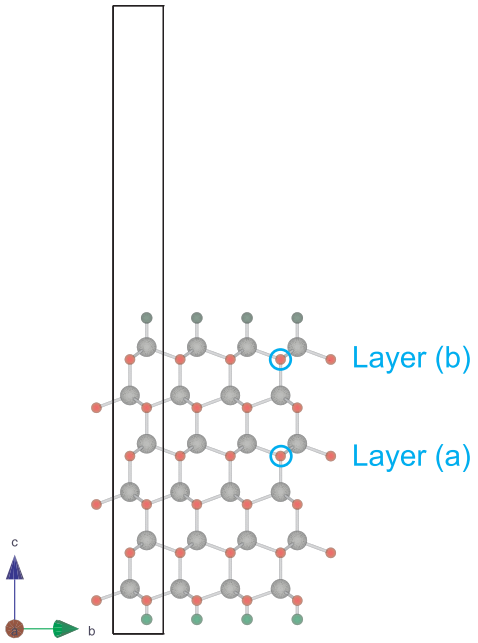

Figure 8.4: The ZnO slab with hydrogen passivated surfaces. The two considered positions of the oxygen vacancies are labeled by (a) and (b).

Table 8.1: Distances between nearest neighbors of the oxygen vacancy in ZnO slab with 84 and 126 atoms in the supercell.

Distance (Å)	84 atom supercell	126 atom supercell
d_1	3.23	3.20
d_2	1.82	1.77
d_3	1.59	1.60
d_4	1.76	1.77

We consider two positions for the oxygen vacancy in this supercell with 84 atoms. First we remove an oxygen atom from a layer in the middle of the slab which is labeled as (a) in Fig. 8.4. The formation energy of the

[3]We also verify this by calculating the formation energy of V_O in both cases. The difference between the formation energies is 28 meV.

neutral defect is obtained by the standard approach. In order to determine the optical ionization energy for the oxygen vacancy in the middle of the slab, we show the total DOS for the pure ZnO slab and the slab for the system $V_O^0[R(0)]$ in Fig. 8.6. We can deduce that the optical ionization energy is 2.9 eV, which can be compared with 2.65 eV for bulk ZnO. The opening of the band gap has thus slightly moved up this defect level in the band gap.

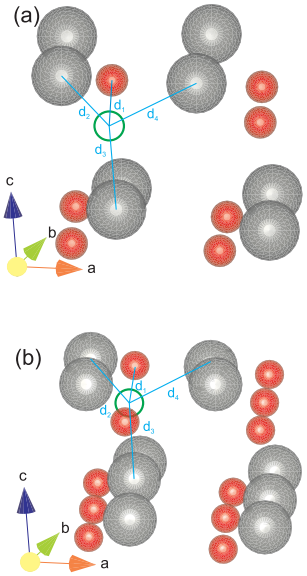

Figure 8.5: The ionic configurations around the V_O positioned in layer (b) of Fig. 8.4 (green circle) after relaxation in the ZnO slab for a supercell with (a) 84 atoms and (b) 126 atoms.

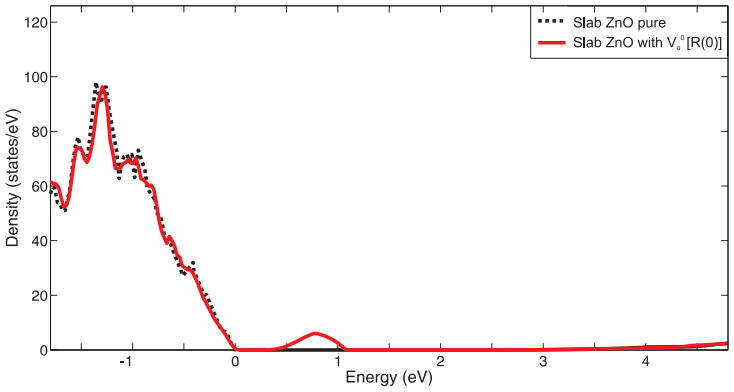

Figure 8.6: DOS for the pure and $V_O^0[R(0)]$ thin ZnO slab.

Now similar to the bulk case, we can estimate the formation energy for V_O^{2+} and the thermal ionization energy for V_O in the ZnO slab. The final result is presented in Fig. 8.7 by the blue curves. We find that the formation energy of $V_O^{2+}[R(2+)]$ crosses the formation energy of $V_O^0[R(0)]$ at a Fermi level of 3 eV above the VBM, leading to a thermal ionization energy of 0.74 eV. Comparing this result with the thermal ionization energy in bulk ZnO of 0.82 eV, we can conclude that the thermal ionization energy has slightly decreased, in contrast to the optical ionization energy. Note also that the formation energy for the neutral defect $V_O^0[R(0)]$ has slightly increased in comparison to the bulk result which is probably a confinement effect. The energy gain upon relaxation for system $V_O^{2+}[R(2+)]$ is larger in case of the slab, leading to the smaller thermal ionization energy in comparison with V_O in bulk ZnO.

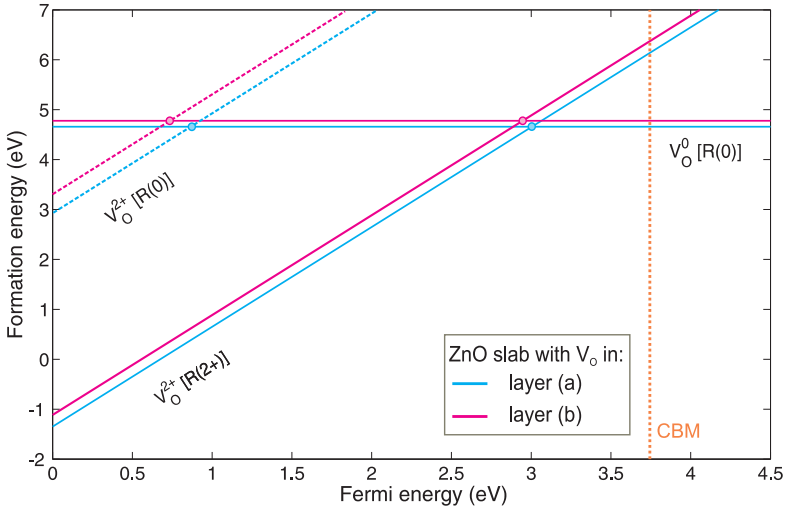

Figure 8.7: The formation energy as a function of the Fermi energy for V_O at position (a) and (b) in the thin ZnO slab.

It is now also interesting to investigate how these ionization energies change when the oxygen vacancy moves towards the surface of the ZnO slab. Therefore we create an oxygen vacancy close to the surface marked as (b) in Fig. 8.4. The obtained results are shown by the red curves in Fig. 8.7. No new DOS calculations were performed, but only relative energy differences with the system with the oxygen vacancy in the center were used. We observe that the formation energy has increased and both the optical as well as the thermal ionization energy have increased by moving the oxygen vacancy to the surface. Therefore, the oxygen vacancies prefer to sit in the center

of the slab where they have a slightly lower thermal (-0.05 eV) and optical (-0.13 eV) ionization energy. Table 8.2 summarizes the obtained formation and ionization energies.

Table 8.2: Formation (at $E_F = 0$) and ionization energies (IE) of V_O in ZnO bulk and slab structures (all in eV).

V_O in ZnO	E_g	$IE_{The.}$	$IE_{Opt.}$	$E_f^0[R(0)]$	$E_f^{2+}[R(0)]$	$E_f^{2+}[R(2+)]$
Bulk	3.43	0.82	2.65	4.28	2.72	-0.95
Slab (a)	3.74	0.74	2.90	4.66	2.98	-1.35
Slab (b)	3.74	0.79	3.03	4.78	3.36	-1.13

8.5 Conclusions

Up to now, almost all first-principles defect studies in the literature have considered defects in bulk systems. Studies of defects in nanostructures are limited to neutral defects in the neutral charge state. The reason is that the total energy of a charged nanostructure depends linearly on the width of the vacuum and can therefore not be used to determine formation energies. Here we proposed a method to determine the transition levels between different charge states without using the formation energy of a defect in a charged state.

We have shown the validity of our approach by considering the oxygen vacancy V_O in bulk ZnO, which is known to act as a deep donor. We have determined the defect transition levels by the standard approach using the hybrid HSE06 functional, and compared the result with our newly proposed method. A good agreement was obtained. Next we have applied the method to study the same defect in a thin ZnO slab. We found that the optical ionization energy of the V_O increased in the thin slab in comparison to the bulk result, while the thermal ionization energy decreased. We also observed that both ionization energies increased if the V_O moved towards the surface of the slab and that the preferential position of the oxygen vacancy is at the center of the slab.

We believe that this new method will allow the study of all kinds of intrinsic and extrinsic defects in semiconductor nanostructures. The combination of the preferential position of a defect, together with the corresponding ionization energies, will give insight into the opto-electronic and transport properties of nanostructures.

Summary and Outlook

The study of defects and impurities is an important area in semiconductor physics. Defects can be used to control the electronic and optoelectronic properties of materials. However, to achieve such control, knowledge of the fundamental processes that control doping is necessary. First-principles calculations have already made important contributions to the understanding of these fundamental processes of doping in different semiconductors.

An important class of materials with an already widespread application area is the transparent conducting oxides (TCOs). These materials combine electrical conductivity and optical transparency and are essential for photovoltaic and optoelectronic applications. The electronic structure of TCOs has therefore been a subject of interest for a long time.

In this thesis we provide a first-principles study of defects in TCO materials using density functional theory (DFT). An introduction to TCO materials, their properties, fabrications, and applications are presented in **chapter 1**. It is followed by a general explanation of the basics of DFT, a quantum mechanical approach for ground state calculations, in **chapter 2**. Then in **chapter 3**, different kinds of defects are classified and some important issues such as donor, acceptor, shallow, deep, formation energy, transition level, optical and thermal ionization energies are introduced. The underestimation of the band-gap by the commonly used LDA or GGA functionals may lead to large errors in the electronic properties. To deal with this problem, different approaches can be employed such as an extrapolation method based on the LDA+U approximation, and the hybrid functional approach which have led to considerable improvement of the study of defects in materials. The extrapolation technique is used in chapters 4, 5 and 6, and the hybrid functional approach is used in chapters 5, 7 and 8 of this thesis.

The understanding of the source of the unintentional conductivity in TCOs has been a topic of intense research in the last decade. For exam-

ple TCOs such as ZnO, SnO_2, and In_2O_3 show typically n-type conductivity. While originally oxygen vacancies were held responsible for this conductivity, ab initio studies have revealed that the oxygen vacancy is a deep donor level in ZnO and therefore cannot account for the unintentional conductivity. On the other hand, these studies also revealed that instead interstitial and substitutional hydrogen forms a shallow donor in these oxides. Cadmium oxide (CdO) is one of the TCO materials which possesses large carrier concentrations together with large electron mobilities in the bulk. Therefore it can act as a strong n-type semiconductor. In **chapter 4**, we have used first-principles calculations based on DFT to study point defects in CdO within the local density approximation and beyond (LDA+U). Hydrogen interstitials and oxygen vacancies are found to act as shallow donors and can be interpreted as the cause of conductivity in CdO. Hydrogen can also occupy an oxygen vacancy in its substitutional form and also acts as a shallow donor. Similar to what was found for ZnO and MgO, hydrogen creates a multicenter bond with its six Cd neighbors in CdO. The charge neutrality level for native defects and hydrogen impurities has been calculated. It is shown that in the case of native defects, it is not uniquely defined. Indeed, this level depends highly on the chemical potentials of the species and one can obtain different values for different end states in the experiment. Therefore, a comparison with experiment can only be made if the chemical potentials of the species in the experiment are well defined. However, for the hydrogen interstitial defect, since this level is independent of the chemical potential of hydrogen, one can obtain a unique value for the charge neutrality level. We find that the Fermi level stabilizes at 0.43 eV above the conduction band minimum in the case of the hydrogen interstitial defect, which is in good agreement with the experimentally reported value of 0.4 eV.

In **chapter 5**, we have studied by first principles calculations the electronic structure and formation energies of group III elements (Al, Ga, In) doped in ZnO. Doped ZnO is an alternative to traditional Sn-doped In_2O_3 in several applications, due to its optical and electrical properties, its high chemical and mechanical stability, and its abundance and non-toxicity. When doped with Al, Ga or In, ZnO thin films can be highly conductive, and have very good optical transmittance (more than 80%) in the visible range. It is shown that all three dopants (Al, Ga, In) are shallow donors in ZnO, and that the preferred charge state is +1 in all cases. To overcome the LDA band gap error in the calculation of formation energies, two correction approaches are applied: an extrapolation scheme based on the LDA+U method and the application of the hybrid HSE06 functional. A comparison between them shows the reliability of the extrapolation technique to predict the transition levels correctly. An advantage of such extrapolation technique is the faster

convergence of the total energies, but it can only be applied if localized d electrons are present in the system. The obtained formation energies are also less accurate within the extrapolation technique.

The incorporation of hydrogen in a material can strongly affect its electronic properties. In most oxides, hydrogen is an amphoteric defect, i.e. it can act as a donor as well as an acceptor, depending on the Fermi level. Therefore it will counteract the conductivity caused by extrinsic dopants. However, in ZnO, hydrogen is a shallow donor. Therefore, we investigate in **chapter 6**, the effect of the presence of both hydrogen and an extrinsic defect (Al, Ga or In) in ZnO. The hydrogen interstitial and the substitutional Al_{Zn}, Ga_{Zn} and In_{Zn} are considered in ZnO. They all act as shallow donors and lead to n-type conductivity in ZnO. Although shallow donors are expected to repel each other, we show by first principles calculations that in ZnO these shallow donor impurities attract and form a complex, leading to a donor level deep in the band gap. This puts a limit on the n-type conductivity of (Al,Ga,In)-doped ZnO in the presence of hydrogen.

Most of the TCO materials exhibit n-type conductivity and development of an efficient p-type TCO is one of the global materials challenges. In **chapter 7**, ZnM_2O_4 (M=Co, Rh, Ir) spinels are considered as a class of potential p-type transparent conducting oxides (TCO). We report the formation energy of acceptor-like defects using first principles calculations with an advanced hybrid exchange-correlation functional (HSE06) within density functional theory (DFT). Due to the discrepancies between the theoretically obtained band gaps with this hybrid functional and the -scattered- experimental results, we also perform GW calculations to support the validity of the description of these spinels with the HSE06 functional. Our results support the claim for experimental re-examination of the band gap in these spinels. The considered defects are the cation vacancy and antisite defects, which are supposed to be the leading source of disorder in the spinel structures. We also discuss the band alignments in these spinels. The calculated formation energies indicate that the antisite defects Zn_M (Zn replacing M, M=Co, Rh, Ir) and V_{Zn} act as shallow acceptors in $ZnCo_2O_4$, $ZnRh_2O_4$ and $ZnIr_2O_4$, which explains the experimentally observed p-type conductivity in those systems. Moreover, our systematic study indicates that the Zn_{Ir} antisite defect has the lowest formation energy in the group and it corroborates the highest p-type conductivity reported for $ZnIr_2O_4$ among the group of ZnM_2O_4 spinels. To gain further insight into factors affecting the p-type conductivity, we have also investigated the formation of localized small polarons by calculating the self-trapping energy of the holes.

The standard theoretical approach to determine the characteristic of dopant impurities in bulk semiconductors is through calculations of forma-

tion energies as a function of the Fermi level, as applied in the previous chapters. However, this method cannot be applied to nanostructures since the total energy of a charged nanostructure depends linearly on the width of the vacuum as a result of the interaction between the charged system and the compensating background. Therefore studies of defects in nanostructures are limited to neutral defects in the neutral charge state. In the last chapter of this thesis, **chapter 8**, we propose a method to determine the transition levels between different charge states without explicitly the formation energy of a defect in a charged state. We show the validity of our approach by considering the oxygen vacancy V_O in bulk ZnO, which is known to act as a deep donor. We have determined the defect transition levels by the standard approach using the hybrid HSE06 functional, and compared the result with our newly proposed method. A good agreement was obtained. Next we have applied the method to study the same defect in a thin ZnO slab. We found that the optical ionization energy of the V_O increases in the thin slab in comparison to the bulk result, while the thermal ionization energy decreases. We also observed that both ionization energies increase if the V_O moved towards the surface of the slab and that the preferential position of the oxygen vacancy is at the center of the slab.

To conclude, this thesis presents first-principles studies of defects in TCOs using DFT. For a quantitative and accurate prediction of the formation energies and transition levels of defects the extrapolation technique and hybrid functional approaches are used. There are still many interesting systems to be explored. The effect of the presence of native defects and impurities can be studied for any other TCO or semiconducting material in bulk or slab configuration. The efficiency of a dopant and its theoretically obtained ionization energy can be determined to help interpreting experimental results as well as to propose materials with desired defect properties. In particular, the following topics could be studied:

- Complexes of dopants are important systems to be studied, since the interaction between donor and acceptor dopants may lower the formation energy providing a more stable system. As an example in Ref. [196], it is shown that N-doped ZnO films can exhibit p-type behavior under appropriate circumstances. It is established by performing several experimental characterization techniques that a complex of V_{Zn}-N_O-H is the cause of such behavior and acts as a shallow acceptor with an ionization energy of 130 meV. Theoretical verifications of these claims can be accomplished by DFT calculations.

- As it is mentioned in the thesis there are already many known n-type TCOs, but the lack of good p-type TCOs limits the presence of active electronic devices. So it is important to find appropriate dopants that can cause p-type conductivity in TCO materials. For example in Ref. [197], a high-throughput computational study is done on thousands of binary and ternary oxides to identify some promising compounds with a wide band gap and low effective hole mass. Several p-type candidates are proposed for the design and development of future p-type transparent conducting oxides. An important step is now to determine which defects have a shallow character in these proposed systems.

- The character of a defect in a nanostructure might differ from its character in the bulk material. Since total energies obtained from calculations for charged nanostructures cannot be used to determine formation energies, we have proposed in chapter 8 a new method to determine the formation energies and the transition levels between different charge states without using the formation energy of a charged system. This technique can now be applied to a variety of systems. An example of the interesting physical insight that is likely to be obtained is given in Ref. [198]. This experimental work showed that the ionization energy of a Si_{Ga} impurity in GaAs increases if the Si_{Ga} defect is located close to the surface. This observation is not understood and our method allows to investigate this problem using first-principles techniques.

Samenvatting en Vooruitzicht

De studie van defecten en onzuiverheden is een belangerijk onderzoeksdomein in de halfgeleiderfysica. Defecten kunnen gebruikt worden om de elektronische en opto-elektronische eigenschappen van materialen te controleren. Echter om zulke controle te bekomen is een goed inzicht nodig in de fundamentele processen die dopering bepalen. Ab initio berekeningen hebben reeds belangrijke bijdragen geleverd tot het begrijpen van deze fundamentele processen rond dopering in verschillende halfgeleiders.

Een belangerijke klasse van materialen met een ruim toepassingsgebied zijn de transparante geleidende oxides (TCOs). Deze materialen combineren elektrische geleidbaarheid en optische transparantie en zijn essentieel voor fotovoltaïsche en opto-elektronische toepassingen. De elektronische structuur van TCOs is daarom een onderwerp dat al sinds geruime tijd bestudeerd wordt.

In deze thesis maken we een ab initio studie van defecten in TCO materialen, gebruik makende van dichtheidsfunctionaaltheorie (DFT). Een inleiding tot TCO materialen, hun eigenschappen, fabricatie en toepassingen komt aan bod in **hoofdstuk 1**. Dit wordt gevolgd door een algemene uitleg over de principes van DFT, een kwantummechanische aanpak voor grondtoestandsberekeningen, in **hoofdstuk 2**. Vervolgens worden in **hoofdstuk 3** verschillende soorten defecten geclassificeerd en worden enkele belangrijke begrippen zoals donor, acceptor, diep en ondiep, vormingsenergie, transitieniveau, optische en thermische ionisatie-energie geïntroduceerd. De onderschatting van de bandkloof door de veelgebruikte LDA of GGA functionalen kan leiden tot grote fouten in de elektronische eigenschappen. Om dit probleem aan te pakken kunnen verschillende methodes gebruikt worden, zoals een extrapolatie methode gebasseerd op de LDA+U benadering, en de hybride functionalen die hebben geleid tot een significante verbetering van de studie van defecten in materialen. De extrapolatie methode wordt gebruikt

in hoofdstukken 4, 5 en 6, en de hybride functionaal methode wordt gebruikt in hoofdstukken 5, 7 en 8 van deze thesis.

Sinds een vijftiental jaar is het begrijpen van de bron van niet-intentionele geleiding in TCOs een belangrijk onderwerp van onderzoek. TCOs zoals ZnO, SnO_2 en In_2O_3 tonen typisch *n*-type geleiding. Hoewel oorspronkelijk ontbrekende zuurstofatomen hiervoor verantwoordelijk werden gehouden hebben ab initio studies duidelijk gemaakt dat een ontbrekend zuurstofatoom een diep donorniveau in ZnO veroorzaakt zodat het niet de oorzaak van de niet-intentionele dopering kan zijn. Aan de andere kant bleek uit deze studies ook dat in de plaats daarvan interstitiële en substitutionele waterstofatomen ondiepe donors vormen in deze oxiden. Cadmium oxide (CdO) is ook een TCO-materiaal met grote ladingsconcentraties samen met een grote elektronmobiliteit. Daarom kan het zich gedragen als een sterke *n*-type halfgeleider. In **hoofdstuk 4** hebben we ab intio berekeningen gebruikt op basis van DFT om puntdefecten te bestuderen in CdO. Interstitieel waterstof en ontbrekende zuurstofatomen blijken te werken als ondiepe donors en kunnen beschouwd worden als de oorzaak van geleiding in CdO. Waterstof kan ook de plaats van een ontbrekend zuurstofatoom bezetten en dit defect is ook een ondiepe donor. Gelijkaardig aan wat werd gevonden voor ZnO en MgO vormt zo'n substitutioneel waterstof ook een multigecentreerde binding met zes Cd-buren in CdO. Het ladingsneutraal-niveau ('*charge neutrality level*') van intrinsieke defecten en waterstofonzuiverheden werd berekend. In het geval van intrinsieke defecten werd aangetoond dat dit niveau niet uniek bepaald is. Het niveau hangt inderdaad sterk af van de chemische potentialen van de elementen en men kan verschillende waarden verkrijgen naar gelang de groeicondities. Daarom kan een vergelijking met experimenten enkel gemaakt worden als de chemische potentialen in het experiment goed gedefinieerd zijn. Voor het interstitieel waterstofdefect kan men echter wel een unieke waarde voor het ladingsneutraal-niveau vinden omdat dit niveau onafhankelijk is van de chemische potentiaal van waterstof. We vinden in dit geval dat het Fermi-niveau 0.43 eV boven het minimum van de conductieband gestabiliseerd wordt, wat goed overeenkomt met de gerapporteerde experimentele waarde van 0.4 eV.

In **hoofdstuk 5** hebben we ab initio berekeningen uitgevoerd voor de elektronische structuur en de vormingsenergieën van groep III elementen (Al, Ga, In) in ZnO. Gedopeerd ZnO vormt een alternatief voor de traditionele Sn-gedopeerde In_2O_3 in verschillende toepassingen door de optische en elektrische eigenschappen, de hoge chemische en mechanische stabiliteit en omdat het veel voorkomend en niet toxisch is. Wanneer dunne ZnO-films gedopeerd worden met Al, Ga of In kunnen ze heel geleidend worden en hebben ze een heel goede optische transmissie (meer dan 80 %) in het zicht-

bare spectrum. We toonden dat alle drie de doperingsatomen (Al, Ga en In) ondiepe donoren zijn in ZnO en dat de geprefereerde ladingstoestand +1 is. Om de fout in de bandkloof te verminderen, werden twee corrigerende methodes toegepast: een extrapolatieschema gebaseerd op de LDA+U techniek en de toepassing van de HSE06 hybride functionaal. Een vergelijking tussen de twee toont de betrouwbaarheid van de extrapolatietechniek om de overgangsniveaus correct te voorspellen. Een voordeel van zo'n extrapolatietechniek is de snellere convergentie van de totale energieën, maar het kan enkel toegepast worden als er gelokaliseerde *d*-elektronen aanwezig zijn in het systeem. De vormingsenergieën verkregen met de extrapolatietechniek zijn ook minder nauwkeurig.

De toevoeging van waterstof in een materiaal kan een grote invloed hebben op de elektronische eigenschappen. Waterstof gedraagt zich als een amfoterisch defect in de meeste oxides, waarmee we bedoelen dat het zich zowel als een donor als een acceptor kan gedragen afhankelijk van het Fermi niveau. Daarom kan het de geleiding die veroorzaakt wordt door extrinsieke dopering tegenwerken. In ZnO daarentegen gedraagt waterstof zich als een ondiepe donor. In **hoofdstuk 6** onderzoeken we daarom het effect van de aanwezigheid van waterstof en een extrinsiek defect (Al, Ga of In) in ZnO. Hierbij beschouwen we interstitieel waterstof samen met substitutioneel Al_{Zn}, Ga_{Zn} en In_{Zn}. Dit zijn allemaal ondiepe donoren en resulteren dus in *n*-type geleiding in ZnO. Met behulp van ab initio berekeningen vinden we dat deze ondiepe donor onzuiverheden in ZnO elkaar aantrekken en samen een complex vormen. Dit leidt tot een diep donor niveau in de bandkloof. De *n*-type geleiding in (Al, Ga, In) gedopeerd ZnO zal dus gelimiteerd worden in de aanwezigheid van waterstof.

De meeste TCO materialen hebben een goede *n*-type geleiding maar de ontwikkeling van een efficiënte *p*-type TCO blijft een van de grote uitdagingen. In **hoofdstuk 7** beschouwen we ZnM_2O_4 (M=Co, Rh, Ir) spinelstructuren als een mogelijke klasse *p*-type geleidende TCOs. We bekijken de vormingsenergie van acceptor-defecten aan de hand van hybride functionaal berekeningen (HSE06). Er blijkt een (groot) verschil te zijn tussen de bandkloven bekomen met de hybride functionaal en de uiteenlopende experimenteel gemeten waarden. Om het gebruik van de hybride functionaal te rechtvaardigen worden er ook GW berekeningen gedaan op deze spinelstructuren. Onze resultaten geven aan dat de experimentele resultaten voor de bandkloof van deze spinelstructuren heronderzocht moeten worden. De defecten die we beschouwen in deze materialen zijn kation vacatures en antisites, die een belangrijke bron van wanorde zijn in de spinelstructuren. We bespreken eveneens de band alignering van deze materialen. De berekende vormingsenergieën geven aan dat de Zn_M en V_{Zn} antisite defecten

zich gedragen als ondiepe acceptoren in $ZnCo_2O_4$, $ZnRh_2O_4$ en $ZnIr_2O_4$. Dit verklaart de waargenomen p-type geleiding in deze systemen. Onze systematische studie geeft aan dat het Zn_{Ir} antisite defect de laagste vormingsenergie heeft en eveneens de hoogste p-type geleiding geeft voor $ZnIr_2O_4$ binnen de groep van de ZnM_2O_4 spinelstructuren. Om verder inzicht te verwerven in de mogelijke factoren die meespelen in het bepalen van de p-type geleiding, hebben we eveneens de vorming van gelokaliseerde kleine polaronen bekeken door de energie voor zelf-opsluiting van holtes te berekenen.

De algemene theoretische benadering om de eigenschappen van gedopeerde onzuiverheden in bulk halfgeleiders te bepalen is door middel van berekening van de vormingsenergieën in functie van het Ferminiveau, zoals toegepast in de vorige hoofdstukken. Deze methode kan echter niet toegepast worden op nanostructuren omdat de totale energie van een geladen nanostructuur afhankelijk is van de breedte van het opgenomen vacuüm als gevolg van de interactie tussen het geladen systeem en de compenserende achtergrond. Om deze reden zijn studies van defecten in nanostructuren beperkt tot neutrale defecten in de neutraal geladen toestand. In het laatste hoofdstuk van deze thesis, **hoofdstuk 8**, stellen we een methode voor om de overgangsniveaus tussen verschillende geladen toestanden te bepalen zonder de expliciete vormingsenergie van een defect in een geladen toestand. We tonen de validiteit van onze benadering aan door een zuurstof vacature V_O in bulk ZnO te bestuderen, een gekende diepe donor. We hebben de defectovergangsniveaus bepaald aan de hand van de standaard benadering met gebruik van de hybride HSE06 functionaal, en we hebben het resultaat vergeleken met onze nieuwe voorgestelde methode. Een goede overeenkomst werd bekomen. Vervolgens hebben we de methode toegepast om hetzelfde defect te onderzoeken in een dunne ZnO laag. We vonden dat de optische ionizatie-energie van de V_O in de dunne slab toenam in vergelijking met het bulk resultaat, terwijl de thermische ionizatie-energie daalde. We vonden ook dat beide ionizatie-energieën stegen als de V_O naar het oppervlak van de dunne laag bewoog en dat de voorkeurspositie van de zuurstof vacature zich in het midden van de dunne laag bevindt.

Samenvattend presenteert deze thesis ab initio studies van defecten in TCOs, gebruikmakend van DFT. Voor een kwantitatieve en nauwkeurige voorspelling van de vormingsenergieën en overgangsniveaus van defecten werden de extrapolatie techniek en de benadering met hybride functionalen gebruikt. Er zijn nog steeds veel interessante systemen om te onderzoeken. Het effect van de aanwezigheid van intrinsieke defecten en onzuiverheden kan bestudeerd worden voor elk TCO of halfgeleidend material in bulk of dunne laag configuratie. De efficiëntie van een dopering en zijn theoretisch verkregen ionizatie-energie kan bepaald worden om te helpen bij de interpretatie

van experimentele resultaten alsook bij de ontwikkeling van materialen met gewenste defecteigenschappen. In het bijzonder zijn volgende onderwerpen interessant om te bestuderen:

- Complexen van onzuiverheden zijn belangrijke systemen om te bestuderen, omdat de interactie tussen donor en acceptor onzuiverheden de vormingsenergie kan reduceren en daarbij een stabieler system kan vormen. In Ref. [188] bijvoorbeeld, wordt aangetoond dat N-gedopeerde ZnO films p-type gedrag kunnen vertonen onder bepaalde omstandigheden. Dit is verwezenlijkt door verschillende experimentele karakterisatietechnieken toe te passen waarbij werd aangetoond dat een complex van V_{Zn}-N_O-H de oorzaak is van zulk gedrag en zich gedraagt als een ondiepe acceptor met een ionizatie-energie van 130 meV. Theoretische vergelijkende studies van deze bevindingen kunnen uitgevoerd worden door gebruik te maken van DFT berekeningen.

- Zoals vermeld in de thesis zijn er reeds veel n-type TCOs gekend, maar het gebrek aan goede p-type TCOs beperkt de aanwezigheid van actieve elektronische apparaten. Daarom is het belangrijk om onzuiverheden te vinden die leiden tot p-type geleiding in TCO materialen. In Ref. [189] bijvoorbeeld, werd een high-troughput computationele studie uitgevoerd op duizenden binaire en ternaire oxides om veelbelovende samenstellingen met een brede bandkloof en lage effectieve gatenmassa te identificeren. Verschillende p-type kandidaten werden voorgesteld voor potentiële toekomstige p-type TCOs. Een belangrijke stap is nu de defecten te bepalen die een ondiep karakter vertonen in deze voorgestelde systemen.

- Het karakter van een defect in een nanostructuur kan verschillen van zijn karakter in een bulk materiaal. Omdat totale energieën verkregen uit berekeningen voor geladen nanostructuren niet gebruikt kunnen worden om de vormingsenergieën rechtstreeks te bepalen, stelden we in hoofdstuk 8 een nieuwe methode voor om de vormingsenergieën en overgangsniveaus tussen verschillende geladen toestanden te bepalen zonder gebruik te maken van de vormingsenergie van een geladen systeem. Een voorbeeld van het interessante fysisch inzicht dat met deze nieuwe methode verkregen zou kunnen worden wordt getoond in Ref. [190]. Dit experimenteel werk toont dat de ionizatie-energie van een Si_{Ga} onzuiverheid in GaAs stijgt als het Si_{Ga} defect dicht bij het oppervlak gelegen is. Deze waarneming is nog niet verklaard. Onze nieuwe methode laat toe dit probleem te onderzoeken met ab initio technieken.

Bibliography

[1] H. Hosono. Recent progress in transparent oxide semiconductors: Materials and device application. *Thin Solid Films*, 515:6000 – 6014, 2007.

[2] T. Minami. Transparent conducting oxide semiconductors for transparent electrodes. *Semicond. Sci. Technol.*, 20:S35–S44, 2005.

[3] K. Bädeker. Über die elektrische leitfähigkeit und die thermoelektrische kraft einiger schwermetallverbindungen. *Ann. Phys. (Leipzig)*, 22:749, 1907.

[4] G. Rupprecht. Untersuchungen der elektrischen und lichtelektrischen leitfähigkeit dünner indiumoxydschichten. *Zeitschrift für Physik*, 139(5):504–517, 1954.

[5] S. Major K.L. Chopra and D.K. Pandya. Transparent conductors - a status review. *Thin Solid Films*, 102(1):1 – 46, 1983.

[6] A. L. Dawar and J. C. Joshi. Semiconducting transparent thin films: their properties and applications. *Journal of Materials Science*, 19(1):1–23, 1984.

[7] R. G. Gordon. Criteria for choosing transparent conductors. *MRS Bulletin*, 25:52–57, 8 2000.

[8] P. Drude. Zur elektronentheorie der metalle. *Annalen der Physik*, 306(3):566–613, 1900.

[9] C. G. Van de Walle and J. Neugebauer. First-principles calculations for defects and impurities: Applications to III-nitrides. *Journal of Applied Physics*, 95(8):3851–3879, 2004.

[10] Z. M. Jarzebski. Preparation and physical properties of transparent conducting oxide films. *physica status solidi (a)*, 71(1):13–41, 1982.

[11] http://www.azonano.com/article.aspx?articleid=3429.

[12] http://www.products.cvdequipment.com.

[13] http://en.wikipedia.org/wiki/sputter deposition.

[14] http://groups.ist.utl.pt/rschwarz/.

[15] O Melikhova, J Cizek, I Prochazka, R Kuzel, M Novotny, J Bulir, J Lancok, W Anwand, G Brauer, J Connolly, E McCarthy, S Krishnamurthy, and J-P Mosnier. Defect studies of ZnO films prepared by pulsed laser deposition on various substrates. *Journal of Physics: Conference Series*, 443(1):012018, 2013.

[16] A. Luque and S. Hegedus. *Handbook of Photovoltaic Science and Engineering*. Wiley, 2011.

[17] H. Hyodo M. Kurita H. Yanagi H. Kawazoe, H. Yasakuwa and H. Hosono. P-type electrical conduction in transparent thin films of $CuAlO_2$. *Nature*, 389:939–942, 1997.

[18] H. Hosono D. C. Paine E. Fortunato, D. Ginley. Transparent conducting oxides for photovoltaics. *MRS Bulletin*, 32:242–247, 2007.

[19] http://www.idtechex.com/tcf.

[20] R. M. Martin. Electronic structure: Basic theory and practical methods. *Cambridge University Press*, 2004.

[21] M. Born and J. R. Oppenheimer. Zur quantentheorie der molekeln. *Ann Physik*, 84:457, 1927.

[22] D. R. Hartree. The wave mechanics of an atom with a non-coulomb central field. part I - theory and methods. *Proc. Cam. Phil. Soc.*, 24:89–110, 1928.

[23] D. R. Hartree. The wave mechanics of an atom with a non-coulomb central field. part II - results and discussion. *Proc. Cam. Phil. Soc.*, 24:111–132, 1928.

[24] D. R. Hartree. The wave mechanics of an atom with a non-coulomb central field. part III - term values and intensities in series in optical spectra. *Proc. Cam. Phil. Soc.*, 24:426–437, 1928.

[25] J. C. Slater. The theory of complex spectra. *Phys. Rev.*, 34:1293–1322, Nov 1929.

[26] C. Møller and M. S. Plesset. Note on an approximation treatment for many-electron systems. *Phys. Rev.*, 46:618–622, Oct 1934.

[27] C. D. Sherrill and H. F. Schaefer III. The configuration interaction method: Advances in highly correlated approaches. volume 34 of *Advances in Quantum Chemistry*, pages 143 – 269. Academic Press, 1999.

[28] H. Kümmel. Origins of the coupled cluster method. *Theoretica chimica acta*, 80(2-3):81–89, 1991.

[29] P. Hohenberg and W. Kohn. Inhomogeneous electron gas. *Physical Review*, 136:B864–B871, 1964.

[30] W. Kohn and L. J. Sham. Self-consistent equations including exchange and correlation effects. *Physical Review*, 140:A1133–A1138, 1965.

[31] M. Levy. Universal variational functionals of electron densities, first-order density matrices, and natural spin-orbitals and solutions of the v-representability problem. *Proc. Natl. Acad. Sci. USA*, 76:606265, 1979.

[32] E. H. Lieb. Density functionals for coulomb systems. *Int. J. Quantum Chem.*, 24:24377, 1983.

[33] P. A. M Dirac. Note on Exchange Phenomena in the Thomas Atom. *Proceedings of the Cambridge Philosophical Society*, 26:376385, 1930.

[34] J. C. Slater. A simplification of the hartree-fock method. *Physical Review*, 81:385–390, 1951.

[35] D. M. Ceperley and B. J. Alder. Ground state of the electron gas by a stochastic method. *Phys. Rev. Lett.*, 45:566–569, Aug 1980.

[36] J. P. Perdew and Y. Wang. Accurate and simple analytic representation of the electron-gas correlation energy. *Phys. Rev. B*, 45:13244–13249, Jun 1992.

[37] J. P. Perdew. Density functional theory and the band gap problem. *International Journal of Quantum Chemistry*, 30(3):451–451, 1986.

[38] J. P. Perdew, K. Burke, and M. Ernzerhof. Generalized gradient approximation made simple. *Phys. Rev. Lett.*, 77:3865–3868, Oct 1996.

[39] C. S. Wang, B. M. Klein, and H. Krakauer. Theory of magnetic and structural ordering in iron. *Phys. Rev. Lett.*, 54:1852–1855, Apr 1985.

[40] T. C. Leung, C. T. Chan, and B. N. Harmon. Ground-state properties of Fe, Co, Ni, and their monoxides: Results of the generalized gradient approximation. *Phys. Rev. B*, 44:2923–2927, Aug 1991.

[41] A. D. Becke. Density-functional exchange-energy approximation with correct asymptotic behavior. *Phys. Rev. A*, 38:3098–3100, Sep 1988.

[42] C. Lee, W. Yang, and R. G. Parr. Development of the colle-salvetti correlation-energy formula into a functional of the electron density. *Phys. Rev. B*, 37:785–789, Jan 1988.

[43] K. Terakura, T. Oguchi, A. R. Williams, and J. Kübler. Band theory of insulating transition-metal monoxides: Band-structure calculations. *Phys. Rev. B*, 30:4734–4747, Oct 1984.

[44] G. A. Sawatzky and J. W. Allen. Magnitude and origin of the band gap in NiO. *Phys. Rev. Lett.*, 53:2339–2342, Dec 1984.

[45] J. Zaanen V. I. Anisimov and O. K. Andersen. Band theory and mott insulators: Hubbard U instead of stoner I. *Phys. Rev. B*, 44:943–954, Jul 1991.

[46] V. I. Anisimov, I. V. Solovyev, M. A. Korotin, M. T. Czyżyk, and G. A. Sawatzky. Density-functional theory and NiO photoemission spectra. *Phys. Rev. B*, 48:16929–16934, Dec 1993.

[47] W. E. Pickett, S. C. Erwin, and E. C. Ethridge. Reformulation of the LDA$+U$ method for a local-orbital basis. *Phys. Rev. B*, 58:1201–1209, Jul 1998.

[48] M. Cococcioni and S. D. Gironcoli. Linear response approach to the calculation of the effective interaction parameters in the LDA+U method. *Phys. Rev. B*, 71:035105, Jan 2005.

[49] D. Segev A. Janotti and C. G. Van de Walle. Effects of cation d states on the structural and electronic properties of III-nitride and II-oxide wide-band-gap semiconductors. *Phys. Rev. B*, 74:045202, Jul 2006.

[50] J. Heyd, J. E. Peralta, G. E. Scuseria, and R. L. Martin. Energy band gaps and lattice parameters evaluated with the Heyd-Scuseria-Ernzerhof screened hybrid functional. *The Journal of Chemical Physics*, 123(17):174101, 2005.

[51] J. P. Perdew and M. Levy. Physical content of the exact kohn-sham orbital energies: Band gaps and derivative discontinuities. *Phys. Rev. Lett.*, 51:1884–1887, Nov 1983.

[52] J. F. Janak. Proof that $\partial E/\partial n_i = \epsilon_i$ in density-functional theory. *Phys. Rev. B*, 18:7165–7168, Dec 1978.

[53] A. R. Williams and U. von Barth. Theory of the inhomogeneous electron gas. *Lundqvist, Stig; March, Norman H. (Eds.)*, 1983.

[54] U. von Barth. Electronic structure of complex materials. *NATO Advanced Studies Institutes Series B, Physics, P. Phariseau and W. Temmermann, Eds. (Plenum, New York)*, 113, 1984.

[55] J. P. Perdew, R. G. Parr, M. Levy, and J. L. Balduz. Density-functional theory for fractional particle number: Derivative discontinuities of the energy. *Phys. Rev. Lett.*, 49:1691–1694, Dec 1982.

[56] A. D. Becke. A new mixing of hartree-fock and local density-functional theories. *J. Chem. Phys.*, 98:1372, 1993.

[57] K. Kim and K. D. Jordan. Comparison of density functional and MP2 calculations on the water monomer and dimer. *The Journal of Physical Chemistry*, 98(40):10089–10094, 1994.

[58] P. J. Stephens, F. J. Devlin, C. F. Chabalowski, and M. J. Frisch. Ab initio calculation of vibrational absorption and circular dichroism spectra using density functional force fields. *The Journal of Physical Chemistry*, 98(45):11623–11627, 1994.

[59] C. Adamo and V. Barone. Toward reliable density functional methods without adjustable parameters: The PBE0 model. *J. Chem. Phys.*, 110:6158, 1999.

[60] G. E. Scuseria J. Heyd and M. Ernzerhof. Hybrid functionals based on a screened coulomb potential. *J. Chem. Phys.*, 118:8207, 2003.

[61] F. Tran and P. Blaha. Accurate band gaps of semiconductors and insulators with a semilocal exchange-correlation potential. *Phys. Rev. Lett.*, 102:226401, Jun 2009.

[62] M. J. Lucero, T. M. Henderson, and G. E. Scuseria. Improved semiconductor lattice parameters and band gaps from a middle-range screened hybrid exchange functional. *Journal of Physics-condensed Matter*, 24(14):145504, April 2012.

[63] H. J. Monkhorst and J. D. Pack. Special points for brillouin-zone integrations. *Phys. Rev. B*, 13:5188–5192, Jun 1976.

[64] P. Schwerdtfeger. The pseudopotential approximation in electronic structure theory. *ChemPhysChem*, 12(17):3143–3155, 2011.

[65] P. E. Blöchl. Projector augmented-wave method. *Phys. Rev. B*, 50:17953–17979, Dec 1994.

[66] G. Kresse and J. Furthmüller. Efficiency of ab-initio total energy calculations for metals and semiconductors using a plane-wave basis set. *Computational Materials Science*, 6(1):15 – 50, 1996.

[67] G. Kresse and D. Joubert. From ultrasoft pseudopotentials to the projector augmented-wave method. *Phys. Rev. B*, 59:1758–1775, Jan 1999.

[68] B. Adolph, J. Furthmüller, and F. Bechstedt. Optical properties of semiconductors using projector-augmented waves. *Phys. Rev. B*, 63:125108, Mar 2001.

[69] P. Y. Yu and M. Cardona. Fundamentals of semiconductors : Physics and materials properties, fourth edition. *Springer-Verlag, Berlin*, 2001.

[70] D.A. Drabold and S. K. Estreicher. Theory of defects in semiconductors. *Springer-Verlag, Berlin*, 2007.

[71] J. Neugebauer A. Pasquarello A. Alkauskas, P. Deák and C. G. Van de Walle. Advanced calculations for defects in materials. *Wiley-VCH Verlag & Co.*, 2011.

[72] C. Wagner and W. Schottky. Theory of regular mixed phases. *Z. Phys. Chem.*, B11:163, 1930.

[73] J. Frenkel. über die wärmebewegung in festen und flüssigen körpern. *Z. Physik*, 35(8-9):652–669, 1926.

[74] S. T. Pantelides. The electronic structure of iriipurities and other point defects in semiconductors. *Reviews of Modern Physics*, 50:4, 1978.

[75] W. Kohn and J. M. Luttinger. Theory of donor states in silicon. *Physical Review*, 98:4, 1955.

[76] A. S. Martins, Timothy B. Boykin, Gerhard Klimeck, and Belita Koiller. Conduction-band tight-binding description for Si applied to P donors. *Phys. Rev. B*, 72:193204, Nov 2005.

[77] A. H. Wilson. *Proc. R. Soc. A*, 134:277, 1932.

[78] R. Williams. Determination of deep centers in conducting gallium arsenide. *Journal of Applied Physics*, 37(9):3411–3416, 1966.

[79] C. T. Sah, L. Forbes, L. I. Rosier, Jr. A. F. Tasch, and A. B. Tole. Thermal emission rates of carriers at gold centers in silicon. *Applied Physics Letters*, 15(5):145–148, 1969.

[80] C. T. Sah, W. W. Chan, H. S. Fu, and J. W. Walker. Thermally stimulated capacitance (TSCAP) in p-n junctions. *Applied Physics Letters*, 20(5):193–195, 1972.

[81] C. T. Sah. Bulk and interface imperfections in semiconductors. *Solid-State Electronics*, 19(12):975 – 990, 1976.

[82] J. W. Davisson B. W. Henvis E. Burstein, J. J. Oberly. The optical properties of donor and acceptor impurities in silicon. *Phys. Rev.*, 82:764–764, 1951.

[83] E. Burstein, E. E. Bell, J. W. Davisson, and M. Lax. Optical investigations of impurity levels in silicon. *The Journal of Physical Chemistry*, 57(8):849–852, 1953.

[84] E. Burstein, J. J. Oberly, and J. W. Davisson. Infrared photoconductivity due to neutral impurities in silicon. *Phys. Rev.*, 89:331–332, Jan 1953.

[85] Masaru Shiotani Anders Lund, Shigetaka Shimada, editor. *Principles and Applications of ESR Spectroscopy*. Springer, 2011.

[86] A. Janotti and C. G. Van de Walle. Native point defects in ZnO. *Phys. Rev. B*, 76:165202, Oct 2007.

[87] D.B. Williams and C.B. Carter. *Transmission Electron Microscopy: A Textbook for Materials Science*. Number v. 1 in Cambridge library collection. Springer, 2009.

[88] Sandra Van Aert, Kees J. Batenburg, Marta D. Rossell, Rolf Erni, and Gustaaf Van Tendeloo. Three-dimensional atomic imaging of crystalline nanoparticles. *Nature*, 470(7334):374–377, February 2011.

[89] Jinwoo Hwang, Jack Y. Zhang, Adrian J. D'Alfonso, Leslie J. Allen, and Susanne Stemmer. Three-dimensional imaging of individual dopant atoms in $SrTiO_3$. *Phys. Rev. Lett.*, 111:266101, Dec 2013.

[90] R.F. Egerton. *Electron Energy-Loss Spectroscopy in the Electron Microscope*. Language of science. Plenum Press, 1996.

[91] J. Neugebauer and C. G. Van de Walle. Chemical trends for acceptor impurities in GaN. *Journal of Applied Physics*, 85(5):3003–3005, 1999.

[92] A. F. Kohan, G. Ceder, D. Morgan, and Chris G. Van de Walle. First-principles study of native point defects in ZnO. *Phys. Rev. B*, 61:15019–15027, Jun 2000.

[93] A. Janotti and C. G. Van de Walle. Fundamentals of zinc oxide as a semiconductor. *Reports on Progress in Physics*, 72(12):126501, 2009.

[94] S. H. Wei. Overcoming the doping bottleneck in semiconductors. *Comput. Mater. Sci.*, 33:337–348, 2004.

[95] A. Walsh, Y. Yan, M. M. Al-Jassim, and S-H Wei. Electronic, energetic, and chemical effects of intrinsic defects and Fe-doping of $CoAl_2O_4$: A DFT+U study. *The Journal of Physical Chemistry C*, 112(31):12044–12050, 2008.

[96] S. B. Zhang, S. H. Wei, and A. Zunger. Intrinsic n-type versus p-type doping asymmetry and the defect physics of ZnO. *Phys. Rev. B*, 63:075205, Jan 2001.

[97] R. Saniz, Y. Xu, M. Matsubara, M. N. Amini, H. Dixit, D. Lamoen, and B. Partoens. A simplified approach to the band gap correction of defect formation energies: Al, Ga, and In-doped ZnO. *Journal of Physics and Chemistry of Solids*, 74(1):45 – 50, 2013.

[98] A. Janotti and C. G. Van de Walle. Oxygen vacancies in ZnO. *Applied Physics Letters*, 87(12):122102, 2005.

[99] S. Ismail-Beigi and S. G. Louie. Self-trapped excitons in silicon dioxide: Mechanism and properties. *Phys. Rev. Lett.*, 95:156401, Oct 2005.

[100] J Heyd, GE Scuseria, and M Ernzerhof. Hybrid functionals based on a screened coulomb potential (vol 118, pg 8207, 2003). *Journal of chemical physics*, 124(21):219906, JUN 7 2006.

[101] A. Janotti and C. G. Van de Walle. New insights into the role of native point defects in ZnO. *Journal of Crystal Growth*, 287(1):58 – 65, 2006.

[102] A. Janotti and C. G. Van de Walle. Hydrogen multicentre bonds. *Nat Mater*, 6(1):44–47, January 2007.

[103] A. Janotti and C. G. Van de Walle. LDA+U and hybrid functional calculations for defects in ZnO, SnO_2, and TiO_2. *physica status solidi (b)*, 248(4):799–804, 2011.

[104] K.I. Hagemark. Defect structure of Zn-doped ZnO. *Journal of Solid State Chemistry*, 16(34):293 – 299, 1976.

[105] C. G. Van de Walle. Hydrogen as a cause of doping in zinc oxide. *Phys. Rev. Lett.*, 85:1012–1015, Jul 2000.

[106] A. K. Singh, A. Janotti, M. Scheffler, and C. G. Van de Walle. Sources of electrical conductivity in SnO_2. *Phys. Rev. Lett.*, 101:055502, Jul 2008.

[107] S. Limpijumnong, P. Reunchan, A. Janotti, and C. G. Van de Walle. Hydrogen doping in indium oxide: An *ab initio* study. *Phys. Rev. B*, 80:193202, Nov 2009.

[108] R. M. Nieminen P. Ágoston, K. Albe and M. J. Puska. Intrinsic *n*-type behavior in transparent conducting oxides: A comparative hybrid-functional study of In_2O_3, SnO_2, and ZnO. *Phys. Rev. Lett.*, 103:245501, Dec 2009.

[109] S. Lany and A. Zunger. Many-body GW calculation of the oxygen vacancy in ZnO. *Phys. Rev. B*, 81:113201, Mar 2010.

[110] C. DeHart T. Barnes H. Moutinho Y. Yan D. Young M. Young J. Perkins T. Coutts X. Li, T. Gessert. A comparison of composite transparent conducting oxides based on the binary compounds CdO and SnO_2: Preprint. *NREL Report No. CP-520-31017*, page 4 pp., 2001.

[111] S. Sadofev, S. Blumstengel, J. Cui, J. Puls, S. Rogaschewski, P. Schafer, and F. Henneberger. Visible band-gap ZnCdO heterostructures grown by molecular beam epitaxy. *Applied Physics Letters*, 89(20):201907, 2006.

[112] P. D. C. King, T. D. Veal, P. H. Jefferson, J. Zúñiga Pérez, V. Muñoz Sanjosé, and C. F. McConville. Unification of the electrical behavior of defects, impurities, and surface states in semiconductors: Virtual gap states in CdO. *Phys. Rev. B*, 79:035203, Jan 2009.

[113] D. T. Speaks, M. A. Mayer, K. M. Yu, S. S. Mao, E. E. Haller, and W. Walukiewicz. Fermi level stabilization energy in cadmium oxide. *Journal of Applied Physics*, 107(11):113706, 2010.

[114] W. Walukiewicz. Mechanism of fermi-level stabilization in semiconductors. *Phys. Rev. B*, 37:4760–4763, Mar 1988.

[115] D. O. Scanlon M. Burbano and G. W. Watson. Sources of conductivity and doping limits in CdO from hybrid density functional theory. *Journal of the American Chemical Society*, 133(38):15065–15072, 2011.

[116] G. Kresse and J. Furthmüller. Efficient iterative schemes for *ab initio* total-energy calculations using a plane-wave basis set. *Phys. Rev. B*, 54:11169–11186, Oct 1996.

[117] H. Liu, H. K. Mao, M. Somayazulu, Y. Ding, Y. Meng, and D. Häusermann. B1-to-B2 phase transition of transition-metal monoxide CdO under strong compression. *Phys. Rev. B*, 70:094114, Sep 2004.

[118] F. P. Koffyberg. Thermoreflectance spectra of CdO: Band gaps and band-population effects. *Phys. Rev. B*, 13:4470–4476, May 1976.

[119] C. Kilic and A. Zunger. n-type doping of oxides by hydrogen. *Applied Physics Letters*, 81(1):73–75, 2002.

[120] O. P. E. Blöchl, Jepsen and O. K. Andersen. Improved tetrahedron method for brillouin-zone integrations. *Phys. Rev. B*, 49:16223–16233, Jun 1994.

[121] J. C. Phillips. Ionicity of the chemical bond in crystals. *Rev. Mod. Phys.*, 42:317–356, Jul 1970.

[122] P. D. C. King. *Charge Neutrality Level in Significantly Cation-Anion Mismatched Semiconductors*. PhD thesis, Figure 5.12, University of Warwick, 2009.

[123] P. D. C. King, T. D. Veal, C. F. McConville, F. Fuchs, J. Furthmuller, F. Bechstedt, P. Schley, R. Goldhahn, J. Schormann, D. J. As, K. Lischka, D. Muto, H. Naoi, Y. Nanishi, Hai Lu, and W. J. Schaff. Universality of electron accumulation at wurtzite c- and a-plane and zinc-blende InN surfaces. *Applied Physics Letters*, 91(9):092101, 2007.

[124] C. Stampfl, C. G. Van de Walle, D. Vogel, P. Krüger, and J. Pollmann. Native defects and impurities in InN: First-principles studies using the local-density approximation and self-interaction and relaxation-corrected pseudopotentials. *Phys. Rev. B*, 61:R7846–R7849, Mar 2000.

[125] K. Xiong, J. Robertson, and S. J. Clark. Behavior of hydrogen in wide band gap oxides. *Journal of Applied Physics*, 102(8):083710, 2007.

[126] J. L. Lyons, A. Janotti, and C. G. Van de Walle. Role of Si and Ge as impurities in ZnO. *Phys. Rev. B*, 80:205113, Nov 2009.

[127] J. I. Nomoto, J. I. Oda, T. Miyata, and T. Minami. Effect of inserting a buffer layer on the characteristics of transparent conducting impurity-doped ZnO thin films prepared by dc magnetron sputtering. *Thin Solid Films*, 519(5):1587 – 1593, 2010.

[128] H. Kim, C. M. Gilmore, J. S. Horwitz, A. Pique, H. Murata, G. P. Kushto, R. Schlaf, Z. H. Kafafi, and D. B. Chrisey. Transparent conducting aluminum-doped zinc oxide thin films for organic light-emitting devices. *Applied Physics Letters*, 76(3):259–261, 2000.

[129] X. Yu, J. Ma, F. Ji, Y. Wang, C. Cheng, and H. Ma. Thickness dependence of properties of ZnO:Ga films deposited by rf magnetron sputtering. *Applied Surface Science*, 245(14):310 – 315, 2005.

[130] R. J. Hong, X. Jiang, B. Szyszka, V. Sittinger, and A. Pflug. Studies on ZnO:Al thin films deposited by in-line reactive mid-frequency magnetron sputtering. *Applied Surface Science*, 207(14):341 – 350, 2003.

[131] E. Fortunato, L. Raniero, L. Silva, A. Gonçalves, A. Pimentel, P. Barquinha, H. Águas, L. Pereira, G. Gonçalves, I. Ferreira, E. Elangovan, and R. Martins. Highly stable transparent and conducting gallium-doped zinc oxide thin films for photovoltaic applications. *Solar Energy Materials and Solar Cells*, 92(12):1605 – 1610, 2008.

[132] T. Yamada, A. Miyake, H. Makino, N. Yamamoto, and T. Yamamoto. Effect of thermal annealing on electrical properties of transparent conductive Ga-doped ZnO films prepared by ion-plating using direct-current arc discharge. *Thin Solid Films*, 517(10):3134 – 3137, 2009.

[133] J. Wienke and A.S. Booij. ZnO:In deposition by spray pyrolysis - influence of the growth conditions on the electrical and optical properties. *Thin Solid Films*, 516:4508 – 4512, 2008.

[134] C. H. Patterson. Role of defects in ferromagnetism in Zn_{1-x} Co_xO: A hybrid density-functional study. *Phys. Rev. B*, 74:144432, Oct 2006.

[135] F. Oba, A. Togo, I. Tanaka, J. Paier, and G. Kresse. Defect energetics in ZnO: A hybrid Hartree-Fock density functional study. *Phys. Rev. B*, 77:245202, Jun 2008.

[136] S. J. Clark, J. Robertson, S. Lany, and A. Zunger. Intrinsic defects in ZnO calculated by screened exchange and hybrid density functionals. *Phys. Rev. B*, 81:115311, Mar 2010.

[137] M. Schulz O. Madelung and H. Weiss. Numerical data and functional relationships in science and technology. *Springer-Verlag, Berlin*, 17, 1982.

[138] S. S. Shinde, P. S. Shinde, C. H. Bhosale, and K. Y. Rajpure. Optoelectronic properties of sprayed transparent and conducting indium doped zinc oxide thin films. *Journal of Physics D: Applied Physics*, 41(10):105109, 2008.

[139] J. A. Sans, J. F. Sánchez-Royo, A. Segura, G. Tobias, and E. Canadell. Chemical effects on the optical band-gap of heavily doped ZnO:M_{III} (M=Al, Ga, In): An investigation by means of photoelectron spectroscopy, optical measurements under pressure, and band structure calculations. *Phys. Rev. B*, 79:195105, May 2009.

[140] S. Bloom and I. Ortenbur. Pseudopotential band-structure of ZnO. *Physica status solidi b-basic research*, 58(2):561–566, 1973.

[141] S. C. Jain, J. M. McGregor, and D. J. Roulston. Band-gap narrowing in novel III-V semiconductors. *Journal of applied physics*, 68(7):3747–3749, OCT 1 1990.

[142] M. N. Amini, R. Saniz, D. Lamoen, and B. Partoens. Hydrogen impurities and native defects in CdO. *Journal of applied physics*, 110(6), SEP 15 2011.

[143] C. G. Van de Walle and J. Neugebauer. Universal alignment of hydrogen levels in semiconductors, insulators and solutions. *Nature*, 423(6940):626–628, June 2003.

[144] S. F. J. Cox, E. A. Davis, S. P. Cottrell, P. J. C. King, J. S. Lord, J. M. Gil, H. V. Alberto, R. C. Vilão, J. Piroto Duarte, N. Ayres de Campos, A. Weidinger, R. L. Lichti, and S. J. C. Irvine. Experimental confirmation of the predicted shallow donor hydrogen state in zinc oxide. *Phys. Rev. Lett.*, 86:2601–2604, Mar 2001.

[145] F. Leiter H. Zhou F. Henecker B. K. Meyer S. B. Orlinskii J. Schmidt D. M. Hofmann, A. Hofstaetter and P. G. Baranov. Hydrogen: A relevant shallow donor in zinc oxide. *Phys. Rev. Lett.*, 88:045504, Jan 2002.

[146] Y. Chen, D. M. Bagnall, H. Koh, K. Park, K. Hiraga, Z. Zhu, and T. Yao. Plasma assisted molecular beam epitaxy of ZnO on c-plane sapphire: Growth and characterization. *Journal of Applied Physics*, 84(7):3912–3918, 1998.

[147] A. Nuruddin and J. R. Abelson. Improved transparent conductive oxide/p^+/i junction in amorphous silicon solar cells by tailored hydrogen flux during growth. *Thin Solid Films*, 394(12):48 – 62, 2001.

[148] T. Minami. New n-type transparent conducting oxides. *MRS Bulletin*, 25:38–44, 8 2000.

[149] W. Liu, G. Du, Y. Sun, Y. Xu, T. Yang, X. Wang, Y. Chang, and F. Qiu. Al-doped ZnO thin films deposited by reactive frequency magnetron sputtering: H2-induced property changes. *Thin Solid Films*, 515(5):3057 – 3060, 2007.

[150] S. H. Lee, T. S. Lee, K. S. Lee, B. Cheong, Y. D. Kim, and W. M. Kim. Characteristics of hydrogen Co-doped ZnO: Al thin films. *Journal of Physics D-Applied Physics*, 41(9), MAY 7 2008.

[151] S. H. Lee, T. S. Lee, K. S. Lee, B. Cheong, Y. D. Kim, and W. M. Kim. Effect of heat treatment of sputter deposited ZnO films co-doped with H and Al. *Journal of Electroceramics*, 23(2-4):468–473, 2009.

[152] S. J. Tark, Y. W. Ok, M. G. Kang, H. J. Lim, W. M. Kim, and D. Kim. Effect of a hydrogen ratio in electrical and optical properties of hydrogenated Al-doped ZnO films. *Journal of Electroceramics*, 23(2-4):548–553, 2009.

[153] D. H. Kim, S. H. Lee, G. H. Lee, H. B. Kim, K. H. Kim, Y. G. Lee, and T. H. Yu. Effects of deposition temperature on the effectiveness of hydrogen doping in Ga-doped ZnO thin films. *Journal of Applied Physics*, 108(2):023520, 2010.

[154] X. Li, B. Keyes, S. Asher, S. B. Zhang, S. H. Wei, T. J. Coutts, S. Limpijumnong, and C. G. Van de Walle. Hydrogen passivation effect in nitrogen-doped ZnO thin films. *Applied Physics Letters*, 86(12):122107, 2005.

[155] H. Y. He, J. Hu, and B. C. Pan. Hydrogen in Ag-doped ZnO: Theoretical calculations. *The Journal of Chemical Physics*, 130(20):204516, 2009.

[156] S. Zh. Karazhanov, E. S. Marstein, and A. Holt. Hydrogen complexes in Zn deficient ZnO. *Journal of Applied Physics*, 105(3):033712, 2009.

[157] S. Limpijumnong, S. B. Zhang, S. H. Wei, and C. H. Park. Doping by large-size-mismatched impurities: The microscopic origin of arsenic- or antimony-doped *p*-type zinc oxide. *Phys. Rev. Lett.*, 92:155504, Apr 2004.

[158] Y. S. Kim and C. H. Park. Rich variety of defects in ZnO via an attractive interaction between O vacancies and Zn interstitials: Origin of *n*-type doping. *Phys. Rev. Lett.*, 102:086403, Feb 2009.

[159] S. Aldridge and A. J. Downs. Hydrides of the main-group metals: New variations on an old theme. *Chemical Reviews*, 101(11):3305–3366, 2001. PMID: 11840988.

[160] W. Humphrey, A. Dalke, and K. Schulten. VMD: Visual molecular dynamics. *Journal of Molecular Graphics*, 14(1):33 – 38, 1996.

[161] S. Limpijumnong, J. E. Northrup, and C. G. Van de Walle. Identification of hydrogen configurations in *p*-type GaN through first-principles calculations of vibrational frequencies. *Phys. Rev. B*, 68:075206, Aug 2003.

[162] L. D. Landau and E. M. Lifshitz. *Quantum Mechanics NonRelativistic Theory*. Butterworth-Heinemann, Boston, 1981.

[163] H. Kawazoe, H. Yasukawa, H. Hyodo, M. Kurita, H. Yanagi, and H. Hosono. P-type electrical conduction in transparent thin films of $CuAlO_2$. *Nature*, 389:939–942, 1997.

[164] H. Mizoguchi, M. Hirano, S. Fujitsu, T. Takeuchi, K. Ueda, and H. Hosono. $ZnRh_2O_4$: A p-type semiconducting oxide with a valence band composed of a low spin state of Rh^{3+} in a $4d^6$ configuration. *Appl. Phys. Lett.*, 80:1207–1209, 2002.

[165] H. J. Kim, I. C. Song, J. H. Sim, H. Kim, D. Kim, Y. E. Ihm, and W. K. Choo. Electrical and magnetic properties of spinel-type magnetic semiconductor $ZnCo_2O_4$ grown by reactive magnetron sputtering. *J. Appl. Phys.*, 95:7387–7389, 2004.

[166] M. Dekkers, G. Rijnders, and D. H. A. Blank. $ZnIr_2O_4$, a p-type transparent oxide semiconductor in the class of spinel zinc-d(6)-transition metal oxide. *Appl. Phys. Lett.*, 90:021903, 2007.

[167] N. Mansourian-Hadavi, S. Wansom, N. H. Perry, A. R. Nagaraja, T. O. Mason, L. H. Ye, and A. J. Freeman. Transport and band structure studies of crystalline $ZnRh_2O_4$. *Phys. Rev. B*, 81:075112, Feb 2010.

[168] D. J. Singh, R. C. Rai, J. L. Musfeldt, S. Auluck, Nirpendra Singh, P. Khalifah, S. McClure, and D. G. Mandrus. Optical properties and electronic structure of spinel $ZnRh_2O_4$. *Chem. Mater.*, 18:2696–2700, 2006.

[169] D. O. Scanlon and G. W. Watson. Band gap anomalies of the $ZnM_2^{III}O_4$ (M^{III} = Co, Rh, Ir) spinels. *Phys. Chem. Chem. Phys.*, 13:9667–9675, 2011.

[170] H. Dixit, R. Saniz, S. Cottenier, D. Lamoen, and B. Partoens. Electronic structure of transparent oxides with the tran-blaha modified becke-johnson potential. *J. Phys.: Condens. Matter.*, 24:205503, 2012.

[171] T. R. Paudel, A. Zakutayev, S. Lany, M. d'Avezac, and A. Zunger. Doping rules and doping prototypes in A_2BO_4 spinel oxides. *Adv. Funct. Mater.*, 21:4493–4501, 2011.

[172] T. R. Paudel, S. Lany, M. d'Avezac, A. Zunger, N. H. Perry, A. R. Nagaraja, T. O. Mason, J. S. Bettinger, Y. Shi, and M. F. Toney. Asymmetric cation nonstoichiometry in spinels: Site occupancy in Co_2ZnO_4 and Rh_2ZnO_4. *Phys. Rev. B*, 84:064109, Aug 2011.

[173] J. D. Perkins, T. R. Paudel, A. Zakutayev, P. F. Ndione, P. A. Parilla, D. L. Young, S. Lany, D. S. Ginley, A. Zunger, N. H. Perry, Y. Tang, M. Grayson, T. O. Mason, J. S. Bettinger, Y. Shi, and M. F. Toney. Inverse design approach to hole doping in ternary oxides: Enhancing p-type conductivity in cobalt oxide spinels. *Phys. Rev. B*, 84:205207, Nov 2011.

[174] A. Zakutayev, T. R. Paudel, P. F. Ndione, J. D. Perkins, S. Lany, A. Zunger, and D. S. Ginley. Cation off-stoichiometry leads to high p-type conductivity and enhanced transparency in Co_2ZnO_4 and Co_2NiO_4 thin films. *Phys. Rev. B*, 85:085204, Feb 2012.

[175] A. Schleife, C. Rodl F. Fuchs, J. Furthmüller, and F. Bechstedt. Branch-point energies and band discontinuities of III-nitrides and III-/II-oxides from quasiparticle band-structure calculations. *Appl. Phys. Lett.*, 94:012104, 2009.

[176] D. Emin. Small polarons. *Phys. Today*, 35 [6]:34–40, 1982.

[177] N. F. Mott and M. J. Littleton. Conduction in polar crystals .1. electrolytic conduction in solid salts (reprinted from, vol 34, pg 485, 1938). *J. Chem. Soc., Faraday Trans. 2*, 85:565–579, 1989.

[178] A. M. Stoneham. Small polarons and polaron transitions. *J. Chem. Soc., Faraday Trans. 2*, 85:505–516, 1989.

[179] A. M. Stoneham, J. Gavartin, A. L. Shluger, A. V. Kimmel, D. M. Ramo, H. M. Ronnow, G. Aeppli, and C. Renner. Trapping, self-trapping and the polaron family. *J. Phys. Condens. Matter.*, 19:255208, 2007.

[180] A. R. Nagaraja, N. H. Perry, T. O. Mason, Y. Tang, M. Grayson, T. R. Paudel, S. Lany, and A. Zunger. Band or polaron: The hole conduction mechanism in the p-type spinel Rh_2ZnO_4. *J. Am. Ceram. Soc.*, 95:269–274, 2012.

[181] M. Shishkin and G. Kresse. Implementation and performance of the frequency-dependent GW method within the PAW framework. *Phys. Rev. B*, 74:035101, Jul 2006.

[182] M. Shishkin and G. Kresse. Self-consistent GW calculations for semiconductors and insulators. *Phys. Rev. B*, 75:235102, Jun 2007.

[183] P. Deák, B. Aradi, and T. Frauenheim. Band lineup and charge carrier separation in mixed rutile-anatase systems. *J. Phys. Chem. C*, 115:3443–3446, 2011.

[184] B. Höffling, A. Schleife, F. Fuchs, C. Rödl, and F. Bechstedt. Band lineup between silicon and transparent conducting oxides. *Appl. Phys. Lett.*, 97:032116, 2010.

[185] D. D. Wagman, W. H. Evans, V. B. Parker, R. H. Schumm, I. Halow, S. M. Bailey, K. L. Churney, and R. L. Nuttall. The NBS tables of chemical thermodynamic properties. selected values for inorganic and C1 and C2 organic substances in SI units. *Journal of physical and chemical reference data*, 11:Suppl. 2, 1982.

[186] J. D. Cox, D. D. Wagman, and V. A. Medvedev. CODATA key values for thermodynamics. *CODATA Key Values for Thermodynamics, Hemisphere Pbl. Corp.: New York*, 1989.

[187] M-S Miao and R Seshadri. Rh_2O_3 versus IrO_2: relativistic effects andthe stability of Ir^{4+}. *J. Phys.: Condens. Matter*, 24:215503, 2012.

[188] J. B. Varley, A. Janotti, C. Franchini, and Chris G. Van de Walle. Role of self-trapping in luminescence and p-type conductivity of wide-band-gap oxides. *Phys. Rev. B*, 85:081109, 2012.

[189] H. Zhou and Z. Li. Synthesis of nanowires, nanorods and nanoparticles of ZnO through modulating the ratio of water to methanol by using a mild and simple solution method. *Materials Chemistry and Physics*, 89(23):326 – 331, 2005.

[190] D.W. Zeng, C.S. Xie, M. Dong, R. Jiang, X. Chen, A.H. Wang, J.B. Wang, and J. Shi. Spinel-type $ZnSb_2O_4$ nanowires and nanobelts synthesized by an indirect thermal evaporation. *Applied Physics A*, 79(8):1865–1868, 2004.

[191] H. Zhang, D. Yang, X. Ma, Y. Ji, J. Xu, and D. Que. Synthesis of flower-like ZnO nanostructures by an organic-free hydrothermal process. *Nanotechnology*, 15(5):622, 2004.

[192] F. Liu, P. J. Cao, H. R. Zhang, J. Q. Li, and H. J. Gao. Controlled self-assembled nanoaeroplanes, nanocombs, and tetrapod-like networks of zinc oxide. *Nanotechnology*, 15(8):949, 2004.

[193] L. S. Vlasenko and G. D. Watkins. Optical detection of electron paramagnetic resonance in room-temperature electron-irradiated ZnO. *Phys. Rev. B*, 71:125210, Mar 2005.

[194] X. J. Wang, L. S. Vlasenko, S. J. Pearton, W. M. Chen, and I. A. Buyanova. Oxygen and zinc vacancies in as-grown ZnO single crystals. *Journal of Physics D: Applied Physics*, 42(17):175411, 2009.

[195] J. Li and L. W. Wang. Band-structure-corrected local density approximation study of semiconductor quantum dots and wires. *Phys. Rev. B*, 72:125325, Sep 2005.

[196] J. G. Reynolds, C. L. Reynolds, A. Mohanta, J. F. Muth, J. E. Rowe, H. O. Everitt, and D. E. Aspnes. Shallow acceptor complexes in p-type ZnO. *Applied Physics Letters*, 102(15):–, 2013.

[197] G. Ceder G. M. Rignanese G. Hautier, A. Miglio and X. Gonze. Identification and design principles of low hole effective mass p-type transparent conducting oxides. *Nat Commun*, 4:–, August 2013.

[198] A. P. Wijnheijmer, J. K. Garleff, K. Teichmann, M. Wenderoth, S. Loth, R. G. Ulbrich, P. A. Maksym, M. Roy, and P. M. Koenraad.

Enhanced donor binding energy close to a semiconductor surface. *Phys. Rev. Lett.*, 102:166101, Apr 2009.

Curriculum Vitae

Mozhgan Amini

Curriculum Vitae

Personal Information

Born 19/04/1984, Mashhad, Iran

Education

2009–2013 **PhD of Science in Physics**,
Condensed matter theory group, Department of physics, University of Antwerp, Antwerp, Belgium.
Title of my PhD Thesis:
First-principle Study of Defects in Transparent Conducting Oxide Materials.

2006–2008 **Master of Science in Solid State Physics**,
Department of physics, Ferdowsi University of Mashhad, Mashhad, Iran.
Title of my Master Thesis:
First-principles Study of Mechanical Properties of $PbTiO_3$ Perovskite Crystal.

U 313, Groenenborgerlaan 171 – 2020 Antwerpen
Belgium
+32 (488) 806 913 • ☎ +32 (3) 265 3431
✉ mozhgan.amini@uantwerpen.be

2002–2006 **Bachelor of Science in Physics**,
Department of physics, Ferdowsi University of Mashhad, Mashhad, Iran.

Languages

Persian **native**
English **fluent**
French **basic**

Computer Skills

Operating systems	Windows, Linux	Programming Language	Fortran, Python
Office	Word, Excel, PowerPoint	Mathematical software	Matlab, Maple
DFT packages	VASP, ABINIT	Other Packages	Origin, LATEX, CorelDRAW

Conferences Presentations

Poster Summer School on "Computational Materials Sciences"
28th June – 3th July 2010, San Sebastian, Spain

Poster Belgium Physical Society meeting (BPS)
25 May 2011, University of Namur, Belgium

Poster Quantum Chemistry Meeting in Belgium, Tenth Edition (QCB10)
10 February 2012, VUB, Brussel, Belgium

Oral DPG Spring Meeting of the Condensed Matter Physics
25-30 March 2012, Berlin, Germany

U 313, Groenenborgerlaan 171 – 2020 Antwerpen
Belgium
+32 (488) 806 913 • ☎ +32 (3) 265 3431
mozhgan.amini@uantwerpen.be

Professional Training

Spring School	41st International Spring School, "Electronic Oxides - Correlation Phenomena, Exotic Phases, and Novel Functionalities" 08-19 March 2010, Julich, Germany
Summer School	Summer School on "Computational Materials Sciences" 28th June – 3th July 2010, San Sebastian, Spain
Winter School	School on "Computational Modeling of Materials" 2-3 December 2010, University of Antwerp, Belgium

Teaching Experience

Teacher Assistant	Quantum mechanics : courses in 2007-2008 Department of physics, Ferdowsi University of Mashhad, Mashhad, Iran

List of Publications

- M. N. Amini, R. Saniz, D. Lamoen, and B. Partoens, *Hydrogen impurities and native defects in CdO*, Journal of Applied Physics **110**, 063521 (2011)
- M. N. Amini, M. Matsubara, R. Saniz, D. Lamoen, and B. Partoens, *Attracting shallow donors: Hydrogen passivation in (Al,Ga,In)-doped ZnO*, Physical Review B **86**, 165207 (2012)
- R. Saniz, Y. Xu, M. Matsubara, M. N. Amini, H. Dixit, D. Lamoen, and B. Partoens, *A simplified approach to the band gap correction of defect formation energies: Al, Ga, and In-doped ZnO*, Journal of Physics and Chemistry of Solids **74** 45–50 (2013)
- M. N. Amini, O. Leenaerts, D. Lamoen, and B. Partoens, *Graphane- and Fluorographene-Based Quantum Dots*, Journal of Physical Chemistry C, **117 (31)**, 16242 (2013)

U 313, Groenenborgerlaan 171 – 2020 Antwerpen
Belgium
+32 (488) 806 913 • ☎ +32 (3) 265 3431
mozhgan.amini@uantwerpen.be

- S. Dabaghmanesh, R. Saniz, M. N. Amini, D. Lamoen, and B. Partoens, *Perovskite transparent conducting oxides: an ab initio study*, Journal of Physics: Condensed Matter **25**, 415503 (2013)
- M. N. Amini, H. Dixit, R. Saniz, D. Lamoen, and B. Partoens, *Origin of P-type Conductivity in ZnM_2O_4 (M=Co, Rh, Ir)*, Phys. Chem. Chem. Phys., 2014, DOI: 10.1039/C3CP53926A.

Research Interests

- Electronic and optical properties of materials using ab initio calculations
- Electronic properties of two dimensional systems such as graphene nanostructures

Awards and Honor

- Award of top BS graduate student, Physics department of Ferdowsi University of Mashhad, Mashhad, Iran (2006)
- Award of top MS graduate student, Physics department of Ferdowsi University of Mashhad, Mashhad, Iran (2008)
- Workshop grant awarded by Fonds Wetenschappelijk Onderzoek (FWO) (2011)

U 313, Groenenborgerlaan 171 – 2020 Antwerpen
Belgium
+32 (488) 806 913 • ☎ +32 (3) 265 3431
✉ mozhgan.amini@uantwerpen.be